Faculté des Sciences
Département de Physique
Group for Research and Applications in Statistical Physics

Walking droplets above cavities

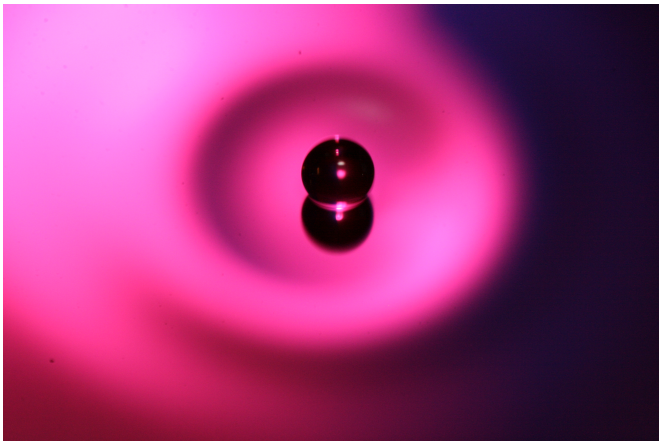

Dissertation présentée par

Boris Filoux

en vue de l'obtention du titre de
Docteur en Sciences
Année académique 2017-2018

Remerciements

Commençons tranquillement la lecture de ce manuscrit, avec la traditionnelle section des remerciements. Si j'attendais avec impatience ce moment marquant la fin de la rédaction de cette thèse, je le redoute à présent. En effet, le challenge va être de n'oublier personne. Si par malheur cela m'arrivait, croyez-moi j'en suis sincèrement navré.

J'ai découvert le laboratoire du GRASP en effectuant un stage de M1. J'y ai rencontré Nicolas Vandewalle, qui m'a fait découvrir la très jolie manipe des gouttes rebondissantes et des marcheurs. Pour la première fois, je me trouvais devant une expérience qui me fascinait et m'émerveillait, comme un gamin peut l'être lorsqu'il déballe ses cadeaux à Noël ! J'ai donc passé deux mois à « jouer » avec des cristaux de gouttes. A l'issue de ce séjour bien trop court à mon goût, je suis retourné en France pour commencer mon M2. Arrivé à la fin de l'année, j'ai repris contact avec Nicolas qui m'a proposé un sujet de thèse... sur les marcheurs. J'ai fait mon balluchon, et suis parti pour la Belgique.

En premier lieu, je souhaite remercier Nicolas Vandewalle qui aura été pour moi un excellent promoteur, avec de nombreuses qualités autant scientifiques qu'humaines. Merci de m'avoir accompagné, conseillé et d'avoir su me remotiver avec votre enthousiasme inébranlable lorsque les manipes se faisaient capricieuses.
J'aimerais aussi remercier l'ensemble des membres de mon jury. Merci à Denis Terwagne et Antonin Eddi, de m'avoir fait l'immense honneur de faire partie de mon jury. Leurs thèses ont été pour moi des modèles à suivre lorsque j'ai découvert le sujet des marcheurs. Thanks to Tomas Bohr who accepted to come from Denmark for this special day and for the interest you have shown in my work. Je remercie Peter Schlagheck, qui résout les équations comme personne, pour les discussions échangées et sa bienveillance. Et enfin, une pensée particulière pour Stéphane Dorblodo... Dordolo... Dorbole... Stéphane Dorbolo ! Stéphane toujours calme, parvient à monter en un temps record une manipe qui foisonne de résultats exceptionnels. Cela m'a toujours impressionné. Un grand merci pour tes conseils d'expérimentateur avisé, cela m'a été précieux. J'ai également apprécié les discussions diverses et variées au -1 (ou ailleurs, hein) sur le cinéma, les gouttes, etc, sans oublier le fantastique taxi-limousine à la Nouvelle-Orléans !

Au cours de ces quatre années passées au GRASP, j'ai vu passer bon nombre de personnes. Mes pensées vont en premier lieu à mes premières rencontres, et collègues de bureau, Maxime et Arianne. Merci pour ces bons moments passés ensemble au sein de ce local ô combien studieux. Arianne, ton aide en Matlab m'a été précieuse quand j'ai débuté, je t'en suis fort reconnaissant. Maxime, le grand geek, tantôt magicien LV 32 puis guerrier Jedi spé glace, merci de m'avoir donné pas mal d'idées de manipes à faire,

pour comparer théorie et expérience. A short word to Maryam: that was a pleasure to meet you and to share our office with you. Il y a aussi eu Sébastien Ze-Same-Please, le joueur de vieux jeux sur PS1. Ça a été un plaisir de partager toutes ces discussions sur les jeux rétros, Zegema Beach et la galaxie. Enfin, je remercie Jean, le fan de sandwhichs, et Sofiene l'expert en impacts et films liquides. Merci à Martin et Laurent, les anciens de Stéphane, qui en plus d'être de super expérimentateurs ont été les rois des barbecues du B5. Merci à Bob, alias Nicolas, pour les conseils qu'il m'a prodigué lorsque j'ai commencé à travailler sur les marcheurs. Merci à Julien, Maître es blagues (pauvre chèvre) et à Martial l'Ardennais, photographe de génie, pour ces grands moments de calme à Lyon. Je remercie Geoffroy, très réactif au tintement de verres, et Hervé, pour leur bonne humeur et leurs conseils pour améliorer une manipe. Un petit mot aussi pour Salvatore le petit nouveau, Eric le festivalier fou et Alexis MT180 pour leur gentillesse, les discussions partagées et ... ne pas m'avoir grondé quand je rentrais à l'improviste dans leur bureau pour utiliser leur perco. Last but not least, je remercie infiniment mon GRAS (Groupement des Relecteurs Attitrés Sympathiques, eh oui, « what did you expect? » comme le disait Uma Thurman dans une pub pour une boisson gazeuse), qui m'a permis de corriger un nombre incroyable de fautes dans mon manuscrit. Merci à Charlotte, nouvelle secrétaire du GRASP, pour sa maîtrise de l'anglais. Et merci à Galien, Floriane dite FloFlo, et Martin le scout ninja, de l'autre côté du couloir. Sans vous, ma thèse n'aurait pas comporté autant de fous rires, merci de m'avoir transmis votre bonne humeur. Martin, merci pour tous tes récits à propos de tes soirées plus incroyables les unes que les autres. Floflo, merci pour tes conseils de mise en page, suggestions de couleurs pour des graphes etc, et tes délicieux brookies pour la dernière ligne droite. Galien, merci pour toutes ces discussions de musique et de matos autour d'un café. Je tiens aussi à remercier la personne qui a inventé la commande ctrl+f, sans qui mes corrections auraient été nettement plus laborieuses. Une petite pensée à Pauline qui, bien qu'au 1er étage fait aussi partie du 3^{e}.
Enfin, je remercie les techniciens et autres personnes de l'atelier, sans lesquels il serait bien plus difficile de faire fonctionner toutes nos expériences. Merci à Chouaib, Méd, Sam, Sébastien et Michaël. Merci aux secrétaires du 1er pour leur gentillesse et leur aide, merci à Christophe pour les bons moments, et merci à Corbi l'expert en montage vidéos. Merci également à tous les postdocs passés par ici, qui avec leur recul, avaient toujours quelque chose à apporter et savaient toujours me remettre d'aplomb dans les moments de doute. Merci à Guillaume (ta fameuse fonction exportfig m'a accompagné tout au long de ma thèse), Antonella, Baptiste, Pierre-Brice, et Alexis, qui a gentiment répondu à toutes mes questions sur le ressaut !

Durant ces années passées en Belgique, j'ai pu faire la connaissance de nouvelles personnes. Je vais commencer par Oli qui était sans doute un des premiers autochtones que j'ai rencontré, merci de m'avoir fait découvrir le Dino et l'univers décadent du Chapi. Un immense merci à Veston qui m'a fait découvrir, comme il se doit, la ville de Liège, ses recoins et plus généralement: le patrimoine houblonné de son pays. Merci

aux frères Willburn et Julburn pour leur bonne humeur permanente. Will, ta photo avec le chanteur de Possessed à Méan me vendra du rêve toute ma vie. Un grand merci aussi à Stef, Chris, Gaétan, Julie et Julie, Laurent et TH pour toutes ces soirées, festivals et concerts. Je remercie John et Lucie, Jul et Sarah, et Charles-Henry, pour ce récent séjour en République Tchèque dans l'imprenable forteresse de Jaromer, qui m'a vraiment permis de souffler sur la fin de ma rédaction. Merci de m'avoir fait découvrir votre *pizzeri* et d'avoir fait des arrêts à chaque stand de *pivo*. Merci à Chris et Marc pour les superbes concerts qu'ils organisent, et à Flo, Fred et Seymon pour les jams et répètes. Merci à Loïc à la barbe soyeuse, pour toutes les discussions ciné et musique partagées. Un grand merci à Zékia pour tous tes bons plans sur Liège et pour m'avoir régalé à chaque fois que je venais manger à la maison. Un immense aussi à Fred, pour les bons moments passés aussi bien à Liège, qu'au lycée et en prépa. Mes remerciements vont aussi vers Eric qui est devenu plus un ami qu'un proprio: MacGyver durant son temps libre, éleveur de poules, dresseur de chiens, un gars en or. I don't forget my crazy friend from Flanders: Cas ! It's always a pleasure to discover new bands with you, feel free to enjoy the very coming Absolupulus shows. Enfin, mes pensées se tournent vers Kévin, Quentin et Charlotte: merci pour les différents concerts et les soirées nanars que j'ai passés en votre compagnie (mention spéciale au non-terrifiant Sinister).
La musique étant très importante dans ma vie, je remercie musicalement: Arnaud de Humanitas E.E., princesse Yannick et Oli d'Atroxentis, Julien de Karne, Maxime de Dawohl, Ben de Malevolentia, Boris de l'Hiver e. D., Denis de Einsicht, et Morgan de Je, qui m'a transmis sa passion pour les belles LP et le matos de musique plus généralement. Un grand merci aussi à Antoine l'ancien chimiste virtuose à la gratte, pour ses leçons et autres conseils.
A short word to my international friends I met in Enschede: Marco, Daniel and Remon. I really enjoyed all the discussions and the beers shared at de Vluchte.

Un grand merci aussi à mes amis de longue date, dont certains me supportent depuis la maternelle. Merci à Claire et Mathieu pour tous les concerts et festoches passés en votre compagnie. Merci à Manageuse (bonjoir) toutes ces discussions partagées. Merci à Stéphane avec lequel j'étais en cours du collège au lycée et qui a été mon acolyte de DM de math et qui faisait la majeure partie du travail je dois honteusement l'avouer. Merci à Bastis et Papis qui ont rendu le quotidien de la prépa bien plus vivant et délirant. Merci à Guillaume et Benoit qui m'ont accompagné durant tout le M2 et qui étaient toujours partant pour discuter physique au Brewberry. J'en profite pour saluer mes petits franc-comtois que je vois trop peu à mon goût : Maxime et Fanette, et Amaury, mon double maléfique qui est tout aussi fan que moi de Mr. Pickles, Baborlelefan, South Park, DMC ou le coeur a ses raisons. Un tout grand merci à Alexandre et Kévin (Chheeffffff) pour les jams à la gratte, à Emilien (Maître Gouvernail), à Romain et à Quentin, mes plus vieux amis, je pense, depuis la maternelle. Merci à vous deux pour toutes les aventures vécues ensemble, entre les cours de natation, les compètes, le

chalet, les WOP, les remparts, et les 10 000 heures de jeu totalisées sur Warcraft III et Diablo III (un petit Boucher ?) et bien d'autres choses encore.

Enfin, je remercie du fond du coeur mes grands parents, mes parents, ma soeur et l'ensemble de ma famille qui m'ont toujours soutenu depuis tout petit, m'ont toujours encouragé à aller de l'avant et, sans qui tout cela n'aurait pas été possible. Un immense merci à ma mère pour les innombrables crumbles, galettes et tartes aux pommes qui m'attendaient les week-ends où je rentrais en Alsace et mon père qui m'a donné le goût des sciences physiques.

Enfin mes pensées se tournent vers Rondchon, Coton et surtout ma Elena, qui partagent et égayent mon quotidien depuis quelques années déjà.

Merci pour tout et merci à tous.

Contents

Chapter 1

Introduction

1.1 Droplets in daily life

When hearing of droplets, people usually visualise this small amount of liquid, of millimetric size, with its spherical shape. We are all familiar with this tiny object of everyday life. We observe raindrops that slide on our windows, flatten, spread or splash when impacting a solid surface such as pavement, or merge with liquid, such as a lake surface. In the early morning, we encounter dew droplets in grass, pine needles, or on spider webs with their unduloid shape, as seen in Figure 1.1. Droplets are also present in fog, or sprays that are used by farmers.

The applications of the physics of droplets are broad. Understanding the physics of droplets impacts [1–3] enables us to develop ink jet printing [4], fire suppression by sprinklers [5], spray cooling of hot surfaces [6], painting and coating [7]. The knowledge

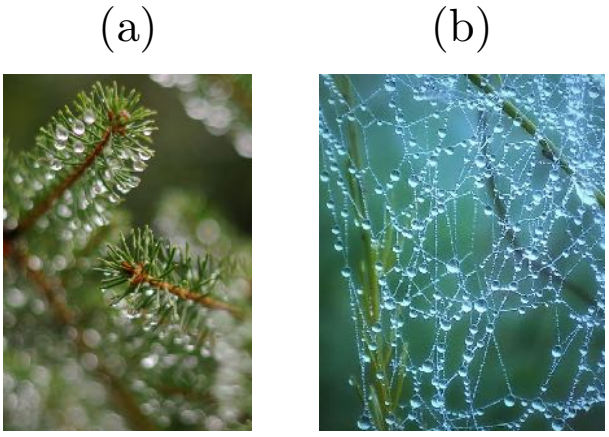

FIGURE 1.1: Photographs of droplets in daily life. (a) Dew droplets on pine needles, (b) dew droplets on a spider web.

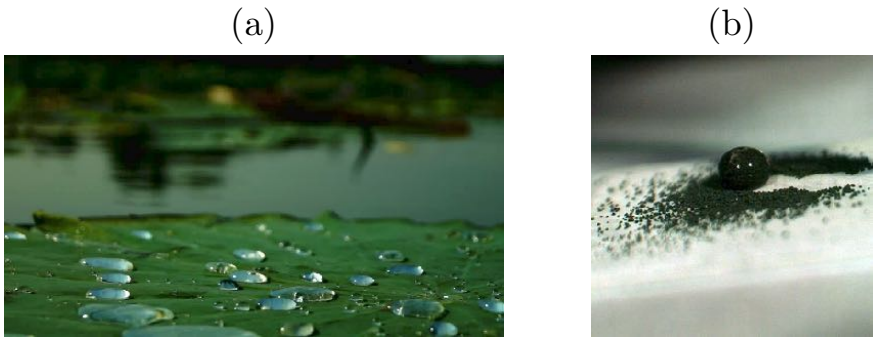

FIGURE 1.2: Photographs of droplets in daily life and an application observed from nature. (a) Droplets lying on a lotus leaf. (b) An example of a self-cleaning surface, a droplet is rolling over a hydrophobic substrate and captures particles (« dust ») in its path, credits to Yao Lu (UCL Chemistry) [12].

of the spreading of a drop, but also the hydrophobic properties of materials, is relevant to the farmer who sprays his plants. Pesticides need to spread but remain on the leaves. Applications inspired from nature observations are also developed [8, 9]. Upon tuning the wettability of a substrate, *e.g.* with a patterned surface [9–11], one can obtain a material with which the droplets have a large contact angle, like lotus leaves in Figure 1.2(a). In addition, such materials benefit from a self-cleaning property [10, 12]: droplets roll over them taking dust away, as one can see in Figure 1.2(b). Handling the wettability of a material is also of interest to model the shape of a drop. This could be performed by electrowetting [13–15]. The applications are numerous: from fog harvesting to the transport of droplets [16, 17], or the development of fluidic lenses [18–20]. With the miniaturisation of fluid processes comes microfluidics [21–23]. This newborn and emergent domain of fluid dynamics tends to handle quantities of fluids of a few μL [24]. It involves various operations on fluids: mixing, splitting, fusion, sorting, trapping, and displacement [16, 17, 23]. Figure 1.3 illustrates those diverse operations performed on droplets.

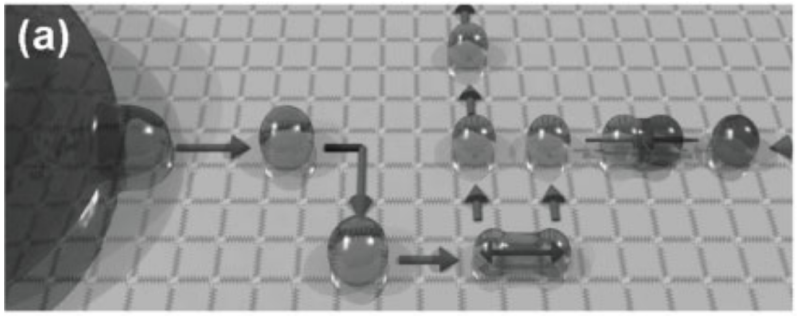

FIGURE 1.3: A system using electrowetting on dielectrics, where four processes are performed on a droplet: dispensing, displacing, splitting and merging (from [17]).

The development of these labs-on-a-chip are convenient tools for biochemical or medicinal applications [23–27], such as drugs preparation [24, 26, 27], combinatorial chemistry [16, 24, 27], cell culture [16, 24, 25], protein analysis [16, 22, 24–26]. Note that, most of the droplet-based microfluidics is founded on the electrowetting on a dielectric substrate.

Dealing with droplets used as microreactors requires a skillful control over the coalescence process. In addition, it can be primordial to keep the samples free of any dust or any other impurity. In particular, it is tricky to manipulate a droplet without altering its physical and chemical properties, when it is in contact with a solid surface. Fortunately, some methods can be used where the droplet is never really in contact with a surface, but levitates. This is the case of the Leidenfrost effect [28]: when a droplet is in contact with a surface hotter than its boiling point, it levitates on its own vapour film. This phenomenon is commonly seen when cooking. Another method consists in using acoustic waves so that the droplet can levitate [29–32]. It is of interest to run fluorescence measurements with a contactless sampling method. This avoids the common issues that scientists encounter when using support material that can alter sample properties. Besides, there is a considerable enthusiasm for an other elegant method, which was recently developed [33, 34]. It consists in a droplet, bouncing on a liquid bath. In particular, a vertical oscillation is provided to the bath. Thanks to it, coalescence is avoided. Moreover, the droplet is never in contact with the bath, and remains free of any contamination. This ability to keep a droplet bouncing permanently constitutes the heart of this thesis.

1.2 Motivations

In this work, we focus on a droplet, that can bounce on a liquid surface. More surprisingly this droplet can even move along a liquid surface. It is propelled by its own waves, generated at each bounce, and evolves at a well defined speed. This curious macroscopic object is called a « walker ». Moreover, it seems to present various analogies with the world of quantum mechanics and it has fascinated the scientists since its discovery in 2005 [34]. Indeed, the droplet is associated with its own waves, such that the droplet behaviour is intimately linked to the waves, which is a striking curiosity.
In this thesis, we investigate further this subject of a droplet between wave-particle physics and fluid mechanics. Various experiments have been performed for a better understanding of walkers. They cover a wide range of 2d systems [35]. Some experiments develop methods to confine or trap droplets, upon using 2d harmonic potential

[36–44]. However, there are only a few studies reported on a 1d system droplet [45]. We wonder then, how to confine a droplet in 1d. Can we find a method to constrain its trajectory along a 1d path? Can experiments of walkers in 1d open new doors through other curiosities related to quantum mechanics? If not, how close to the wave-particle physics can we go? Is the walker entity a real analog to the quantum world, or just a curiosity ? As a starting point, we study the influence of the liquid height on the droplet behaviour. We wonder then how a linear cavity can trap a drop, and how the width of this cavity influences the confinement of a drop. How does droplet confinement affect the interactions between walkers? In this manuscript, we give answers to those different questions, and shed light on other curiosities.

1.3 Strategy

This thesis is organised as follows: in Chapter 2, we develop the state of the art. We explain how a droplet can bounce, and how does it turns into a walker. We also present the different works which have been performed on this subject. Chapter 3 deals with droplet confinement, and introduces our method to manipulate a droplet in one dimension. In Chapter 4, we study the behaviour of a drop placed within an annular cavity. We develop the effects of the memory parameter on the drop, and focus on experiments involving submarine obstacles placed within cavities. Chapter 5 analyses the interaction between several droplets placed within a cavity. The different kinds of interactions between droplets are listed. Finally, we demonstrate that several droplets interacting in an annular cavity share a coherent wave. Chapter 6 concludes and gives some elements of perspective for future works.

Chapter 2

State of the art

2.1 Physics of droplets

2.1.1 Capillary length and surface tension

When looking at a drop, a first naive question that one can ask is: why does the droplet keep a spherical shape? From small to large scales, the physical phenomena that surround us are ruled by different forces. Gravity is the dominant force for objects of considerable size, like oceans, whereas tiny objects are governed by capillary forces, for example, the insect flight or motion on fluid interfaces. A droplet constitutes a fascinating object, since it is just on the edge of the transition between large and small scales. In the 19th century, Laplace and Young evidenced that interfacial tension is responsible for the minimisation of the interfacial area of a drop. The idea is that creating a surface area S between two fluids requires an energetic cost E. Thus, one can define the surface tension, noted σ, which is proportional to this ratio E/S. Common values are $\sigma_{aw} \simeq 72$ mN/m for an air/water interface, $\sigma_{ow} \simeq 20$ mN/m for an oil/water interface. Considering a drop, of radius r_d and mass m, sitting on a solid surface. Its shape deformation results from the competition between gravity and capillary forces. One can build a dimensionless number called Bond number [46, 47], noted

$$\mathrm{Bo} = \frac{mg}{4\pi\sigma r_d} = \frac{\rho g r_d^2}{3\sigma}. \tag{2.1}$$

When this ratio is lower than one, the capillary effects dominate and the droplet remains in its spherical shape, as seen in Figure 2.1(a), while for a Bond number greater than 1, gravity effects dominate and the droplet tends to spread, as seen in Figure 2.1(b). When

both forces are comparable, *i.e.* Bo $\simeq$ 1, one can define a lengthscale corresponding to the capillary length l_c. Thus, equation 2.1 leads to $l_c = \sqrt{\frac{\sigma}{\rho g}}$. For usual liquids, the capillary length is about a few millimetres, and depends on the liquid physical properties. As an example, for water in air at 20°C, the capillary length l_c is equal to 2.7 mm.

2.1.2 Viscosity, inertial and surface tension forces

When studying jet breakup, Lord Rayleigh [51–53] realised that surface tension has to work against inertia in order to bring about jet breakup. Later on, the dimensionless Ohnesorge number was introduced. The latter is noted Oh and compares the viscous forces to inertial and surface tension forces. It characterises the deformations undergone by droplets or bubbles during a breakup process [49, 54]. Two different time scales are

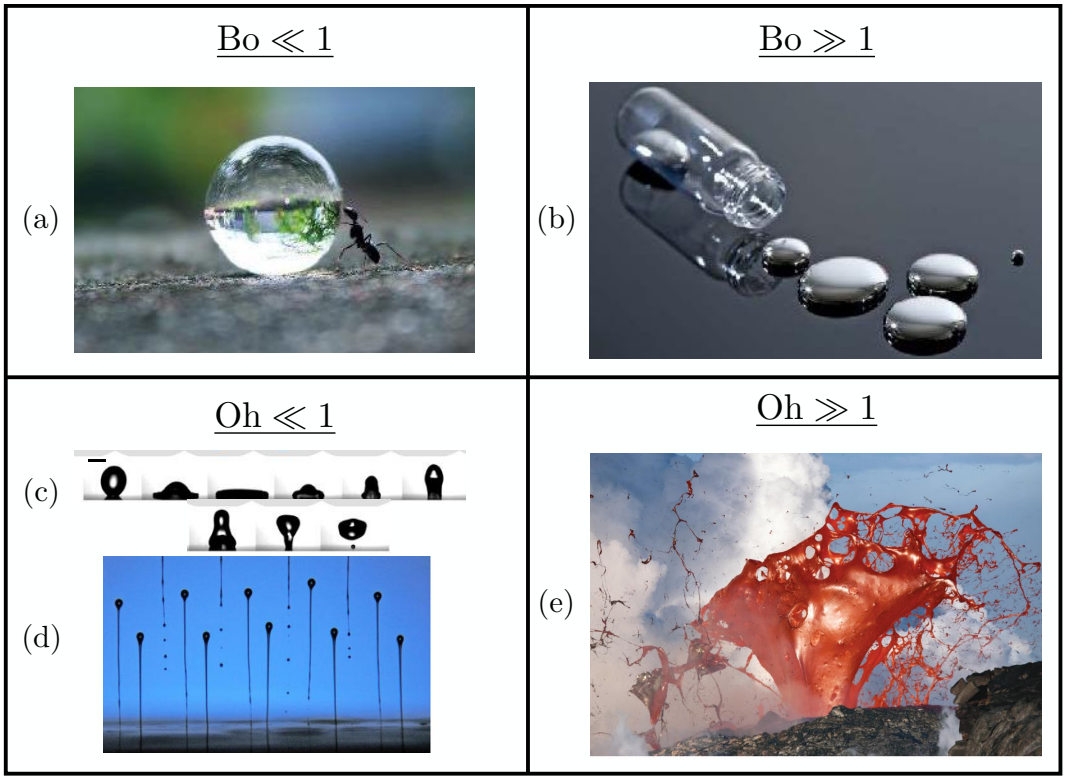

FIGURE 2.1: Illustrations of the influence of the Bond number (a) and (b), and influence of the Ohnesorge number (c) to (e), on droplets and fluids. (a) A droplet keeping its spherical shape at a minuscule Bo number where surface tension effects dominate. (b) Photograph of mercury drops where gravity effects dominate, the droplets spread on the surface. (c) Temporal evolution of a droplet that deforms when impacting and then bouncing on a rigid surface (from [48]). (d) Droplets emerging from a bank of ink-jet nozzles (from [49], credits to Steve Hoath, Cambridge Engineering Department). (e) Fluid-dynamic breakup of basaltic magma which becomes stretched into a sheet that breaks up into filaments (from [50], credits to Bruce Omori).

involved: a viscous time scale t_v and an inertial time scale t_i. They are given by $t_v = \eta r_d/\sigma$ and $t_i = \sqrt{\rho r_d^3/\sigma}$. Ohnesorge number reads

$$\mathrm{Oh} = \frac{t_v}{t_i} = \nu\sqrt{\frac{\rho}{\sigma r_d}}, \tag{2.2}$$

where ν is the kinetic viscosity of the fluid, ρ its density, and r_d the typical length scale, like the droplet radius. A weak Ohnesorge number, $\mathrm{Oh} < 1$, shows that most of the energy inserted is converted into surface tension energy, and the deformation of the droplet is important. In Figure 2.1(c), one can observe the deformation of a drop, bouncing on a flat surface. The physics of jets is also relevant, the smaller the Ohnesorge number, the easiest it is for a jet to break up into tiny droplets. It is particularly of interest in ink jet printing applications, where very small Ohnesorge numbers are used, as illustrated in Figure 2.1(d). However, a large Ohnesorge number, $\mathrm{Oh} > 1$, indicates that viscous dissipation dominates over capillary effects. The droplet becomes therefore hardly deformable. For example, magma breakup is dominated by viscous forces [49, 50, 54]. Instead of observing an atomization of the jet, the breakup results in filaments called Pele's hair [50, 54].

2.2 The inhibition of coalescence

2.2.1 Coalescence

In the coming section, we give a short overview of coalescence. It simply corresponds to the process under which two amounts of fluid can unite to form a larger system. In nature, one can take as an example a raindrop merging with a lake, or several droplets gliding on a spider web that form a larger one, which may detach from the web due to its heavy mass. Considering two coalescing droplets, surface tension drives the motion which joins them into a larger drop. Coalescence was widely studied by Lord Rayleigh in 1899 [52]. Traditional applications of coalescence include sintering: the merging of a powder upon heating, in a homogeneous material, such as glass or ceramics [55]. Other fundamental problems of coalescence consist in the description of two-phase dispersions, such as emulsions [56]. Understanding this issue will enable improved processing of these products. In Figure 2.2, one can observe two photographs of coalescence processes. In Figure 2.2(a), two identical droplets of distilled water are brought into contact. One observes the progressive merging of the droplets. In Figure 2.2(b), one can see a droplet impacting a sessile drop. This impact results in the merging of both droplets, to form a single and larger one.

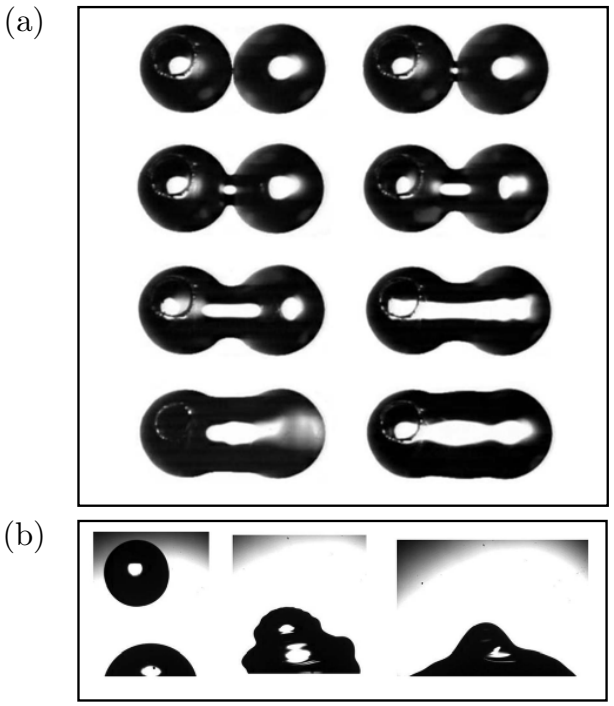

FIGURE 2.2: Photographs of coalescence. (a) Photograph of two droplets of distilled water, viewed from above. They are progressively brought into contact until they merge (from [57]). (b) A falling droplet impacts a sessile droplet laying on a substrate (from [58]).

2.2.2 How to avoid coalescence?

Even though it is of interest to understand coalescence in depth, it can be relevant to know how to prevent it, in order to manipulate droplets. Hereafter, we list some techniques that enable us to do so.

A first method consists in using surfactants. It is well known that a pure water droplet coalesces quasi instantaneously with a pure water surface. However, Amarouchene *et al.* evidenced that the addition of surfactant dramatically changes this behaviour. Indeed, a tiny amount of surfactant added within the liquid increases by two orders of magnitude the lifetime of the droplet on the bath [59]. Another method to delay coalescence was developed by Dell'Aversana *et al.* [60, 61]. In this study, they showed that when a temperature difference is imposed between two droplets, no coalescence occurs when both droplets are brought in contact. Applying a temperature gradient along a surface induces Marangoni convection inside the droplets. Therefore, the air film between both droplets exerts a lubrication force that prevents them from merging, as shown in Figure 2.3. Experiments involving hydraulic jump and droplets were recently performed [62, 63]. When a vertical jet of liquid impinges a horizontal surface, a radially spreading flow is produced, and a circular hydraulic jump is formed. When a droplet

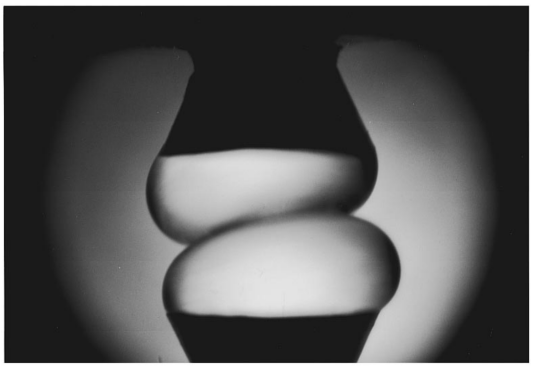

FIGURE 2.3: Photograph of two millimetric droplets. The pendant (sessile) droplet temperature is about 45° C (20° C). When brought in contact no coalescence happens, one can only observe the slipping of both droplets (from [60]).

is placed in this hydraulic jump, it moves along the jump. In particular, the droplet is said to « levitate ». This is due to a thin layer of air just below the drop, which is entrained by the permanent flow of liquid that constitutes the jump. The droplet remains trapped within this hydraulic jump (see Figure 2.4). This situation is similar to the Leidenfrost experiment [28], where the droplet levitates as well on its own vapour film [28, 64–67].

Another subtle and original method to manipulate a droplet was found out in 1978 by Walker [33]. It is probably one of the first work based on bouncing droplets on a liquid surface. Walker showed that coalescence of a droplet with a liquid bath could be avoided thanks to the vibration of a loudspeaker [33]. He related the importance of the air film between the droplet and the bath. Slowing down the drainage of the

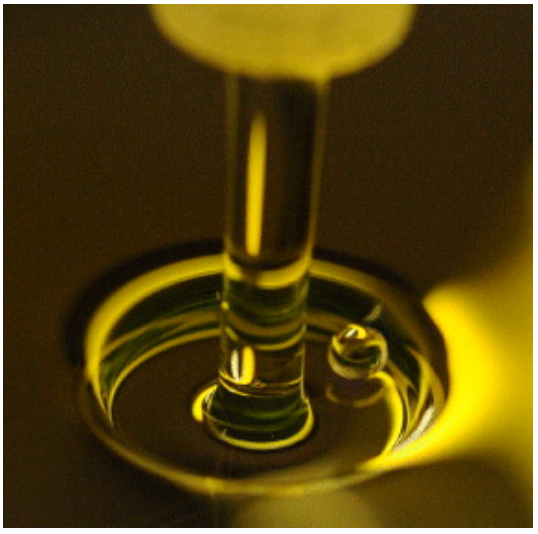

FIGURE 2.4: Photograph of a droplet of 1 mm radius, trapped inside a hydraulic jump (from [63]).

air film between the droplet and the bath delays coalescence. In the experiment of bouncing droplets, Walker went even further by stopping the drainage. Thanks to the vibration applied to the system, while the droplet lifts off the bath, the air film can be permanently regenerated. Thus, the experimenter is released of any time constraint in his manipulation of droplets.

We have discussed here various methods used to avoid coalescence. Hydraulic jump, bouncing droplets, Leidenfrost effects, all of these techniques deal with the control of the air film that separates the droplet from the bath. We discuss the importance of the latter in the next section, related to the experiment with bouncing droplets.

2.3 Bouncing droplets

2.3.1 Importance of the air film

After the work performed by Walker [33], we had to wait until 2005 before it was revisited by the team of Couder [34]. They rationalise the necessary conditions to allow the bouncing of the droplet on the bath. When gently depositing a droplet on a vertically vibrated bath, under certain specific conditions that we will specify hereafter, one can inhibit coalescence. The bath is vibrated at a frequency f and submitted to an acceleration $\gamma = A\omega^2 \cos(\omega t)$. The amplitude of the bath is written A, and $\omega = 2\pi f$. We note $\gamma_m = A\omega^2$ the maximal acceleration. To ensure the bouncing, γ_m has to be larger than a critical value γ_b. Thus, the air film between the droplet and the bath is not broken. The droplet can bounce at the same frequency as the bath is vibrated. This is illustrated in the photographs in Figure 2.5. The forcing bouncing γ_b increases as f^2 [34], but depends as well on the size of the drop. The larger the drop is, the faster γ_b increases, since larger droplets absorb a part of the energy in the deformation.

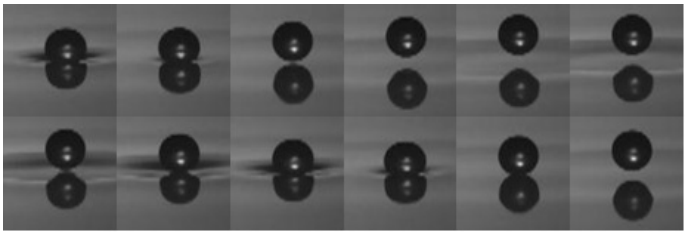

FIGURE 2.5: Photographs of a droplet, of diameter $2r_d = 0.76$ mm, bouncing on a bath vibrated at 60 Hz. Silicone oil of viscosity $\nu = 20$ cSt was used. The time elapsed between two consecutive photographs is $t = 0.002$ s.

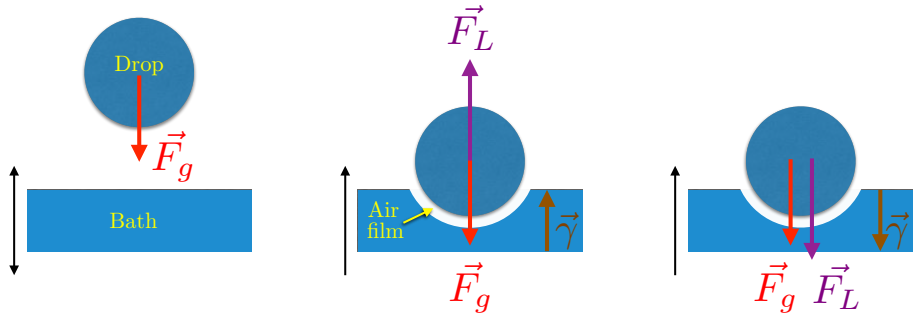

FIGURE 2.6: Schematic of a droplet bouncing on a periodically oscillated bath, that regenerates the air film at each bounce. a) The free fall situation is depicted here, the droplet is only subjected to its weight. b) The landing of the droplet is represented. The bath and the droplet are separated by the air film, the lubrication force prevent the droplet to coalesce. c) At the lift-off the lubrication force points downwards while the air film thickens.

The bouncing mechanism is the following. At first, the droplet when created, is in a free fall situation and only subjected to the gravity force F_g, as it is depicted in Figure 2.6(a). Secondly, the droplet lands on the bath, while the bath is going upwards. During this phase, the droplet is not only subjected to its weight but also to an opposed lubrication force F_L, pointing in the same direction as γ, as indicated in Figure 2.6(b). The air film is squeezed at this moment, and balances the pressure of the drop. During the last phase, see Figure 2.6(c), the droplet lifts off while the bath keeps moving upwards but γ is oriented downwards. Finally, during the droplet flight, the air film can be renewed. Nevertheless, for the lift-off to be allowed, the plate acceleration needs to be larger than the droplet acceleration. This condition is written

$$|\gamma| > \frac{|F_L + F_g|}{m}. \tag{2.3}$$

This mechanism of the bouncing droplet is similar to the case of a solid and inelastic ball bouncing on a vertically vibrated plate [68–70]. In other works [71, 72], focused on the cascade of partial coalescence, it was pointed out that one can build a droplet size filter upon using the bouncing threshold.

2.3.2 Bouncing modes

Protière *et al.* were the first to publish a phase diagram indicating the behaviour of droplets, deposited on an oscillating bath [73]. The latter is vibrated at 50 Hz. The silicone oil used has a viscosity of $\nu = 50$ cSt. Different regions are depicted in Figure 2.7, which depend on the diameter of the droplet $2r_d$, and the non-dimensional

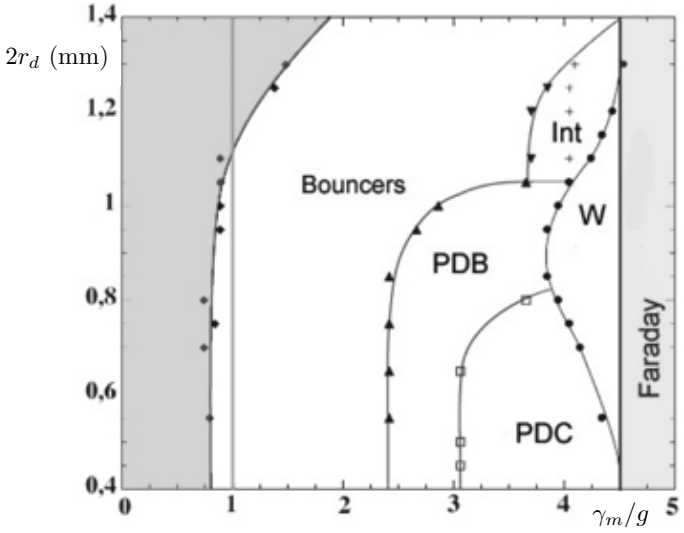

FIGURE 2.7: Phase diagram of the different behaviours of a drop, as a function of its diameter $2r_d$ and the forcing acceleration applied to the bath γ_m/g. Silicone oil was used for the bath and the oil, its viscosity is 50 cSt. The bath is vibrated at $f = 50$ Hz (from [73]).

acceleration applied to the bath γ_m/g, which is commonly noted Γ. One can note two gray regions. The first one, on the left, is the coalescence area, where the droplet is not sustained and quickly coalesces with the bath. The nondimensionalised bouncing threshold is noted $\Gamma_b = \gamma_b/g$. The second area on the right is the Faraday instability region. When γ_m is larger than a threshold γ_F, a pattern of standing waves appears on the surface of the liquid. In this area, the droplets still bounce on the wavy surface. However, their motion is extremely chaotic, their collision with the bath are irregular. It usually ends up with coalescence. More details on this instability are given in section 2.4. The nondimensionalised Faraday threshold is noted $\Gamma_F = \gamma_F/g$. In the region called « Bouncers », the droplets are finally able to bounce on the substrate, at the same forcing frequency applied to the bath. Upon a further increase of the forcing acceleration, one enters a different region depending on the size of the drop. Here, the vertical motion of the droplet is affected. For larger droplets ($2r_d > 1.2$ mm), one encounters an intermittent regime, noted « Int ». The vertical motion of the droplet reveals intermittent disorder. For tinier droplets, the PDB region corresponds to a Period Doubling Bouncing. The droplet passes alternatively from large to small bounces, so that the period doubles. In the PDC region, the process repeats itself in a period doubling cascade, with temporally chaotic motion. Finally, in the W region called Walking region, the period doubling is complete and the droplet bounces on the surface once in two driving periods of the bath. In addition, the droplet even propels itself on the bath, thanks to its own wave, at a constant speed, which depends on the size of the drop, and the forcing acceleration. This is what we call a « walker ».

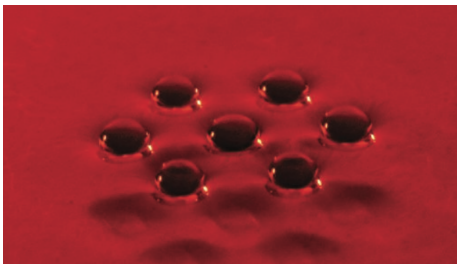

FIGURE 2.8: Hexagonal lattice formed by seven droplets, from [74].

Note that, in the process of bouncing and walking, the deformation of the droplet is relevant. It ensures that the droplet can bounce [75–78]. A bouncing droplet can be seen as an analogous system to a damped driven harmonic oscillator. While viscosity is responsible for damping, it is balanced by surface tension, which can be considered as a restoring force. In particular, the bouncing is an interplay between elastic storage and energy dissipation at each bounce. When it bounces, the droplet loses energy in its internal motion, and in the lubrication film. Eventually, both may be dissipated by viscosity. However, the bath motion balances this loss upon providing some translational energy to the droplet [76]. This energy compensation defines the threshold for bouncing. Otherwise, it was evidenced that deformation of the droplet can be used in order to move it horizontally on the surface of the bath. Thus, one can obtain a rolling droplet [76]. It was shown that spherical harmonics express the resonant effects and the deformations undergone by a droplet [76]. A model was proposed upon using an analogy with bouncing balls on a vibrated plate [68–70]. It consists in a linear mass-spring damper system. The latter was improved by Hubert *et al.* [79, 80], while Moláček and Bush argued in favour of a log spring model [81]. In a recent work, the effects of Bond, Ohnesorge, and Weber numbers on a bouncing droplet, were analysed by Blanchette [82]. The complexity and variety of behaviours of bouncing droplets were reproduced.

2.3.3 Interactions between bouncing droplets and clusters

Interactions between droplets have been studied. It was shown that a second droplet could interact with a first one, in particular, it was proved that the interactions between both wavefields could result in an attraction between the droplets. Adding several droplets results in regular patterns [73, 74]. Seven droplets adopts hexagonal lattice positions, as it is illustrated in Figure 2.8. The crystalline structures adopted by the droplets were therefore widely characterised by Eddi *et al.* [83, 84]. Depending on the forcing conditions, they determined that different patterns could be selected. The stability and destruction of these aggregates were also investigated [84, 85]. In Figure 2.9, one can observe a hexagonal lattice of 19 droplets. The forcing acceleration was

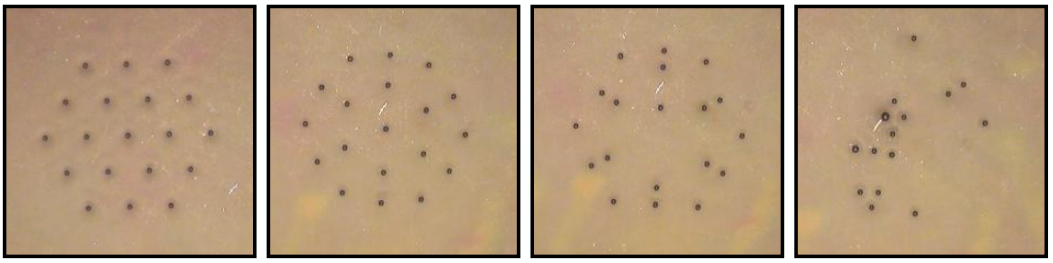

FIGURE 2.9: Different pictures of an aggregate of droplets. The forcing acceleration was gradually increased from left to right. The initial crystal is a hexagon composed of 19 droplets. One can see the deformations undergone while increasing γ. Then 6 pairs of droplets are formed. Finally, the crystal is destroyed. Note that the droplets are all in a bouncing state.

gradually increased, until the merging of the crystal. Few droplets even coalesced at the end. In another contribution from Lieber *et al.* [86], it was shown that varying the driving frequency led to a spinning of the clusters of droplets.

2.4 From bouncing to walking

In the previous section, we discussed the importance of the air film and the wealth of behaviours of bouncing droplets. Hereafter, we present the key object of this thesis: the walker, which is a particular state for bouncing droplets. In the vicinity of the Faraday instability, the droplet generates an extended wavefield on the bath. Hence, thanks to its wave, the droplet starts to walk horizontally across the liquid surface, as seen in Figure 2.10. In the last decade, these « walkers » have exhibited really intriguing and unexpected behaviours. In particular, Couder showed that walking droplets seem to feature quantum-like dynamical behaviours despite their belonging to the macroscopic realm [87–89]. Before focusing on these walking droplets, we first develop the Faraday instability which is a subjacent mechanism in the walking process of the drop.

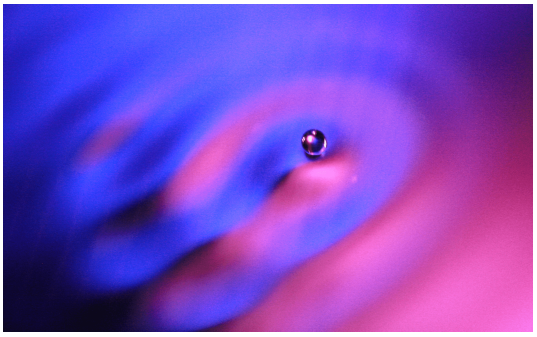

FIGURE 2.10: Photograph of a walker and its waves.

2.4.1 Faraday instability

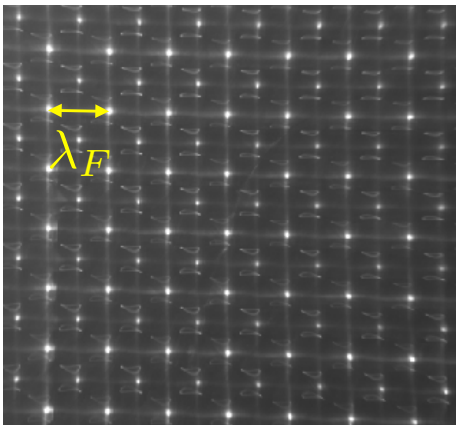

FIGURE 2.11: Photograph of the Faraday instability within a square cavity, in deep water region. The bath is made of silicone oil at $\nu = 20$ cSt, and is vibrated at $f = 70$ Hz, and $\gamma \simeq 4g$. λ_F corresponds to the Faraday wavelength. We measured $\lambda_f = 5.35$ mm.

In 1831, Faraday demonstrated the emergence of a stationary wave pattern along the surface of a vertically vibrated bath [90]. These parametric standing waves oscillate at half of the forcing frequency and are a crossover from capillary and gravitational waves [91–98]. In 1954, Benjamin and Ursell characterised it in the case of an inviscid liquid [99]. Kumar and Tuckerman rationalised the existence of a threshold γ_F beyond which this instability is triggered [100, 101]. In Figure 2.11, one can observe a pattern of Faraday waves within a square cavity of 18×18 cm^2. These patterns depend on the shape of the container [92, 93, 102, 103]. In addition, increasing γ_m above γ_F can lead to more complex lattices and chaotic interfacial dynamics. One can notice the original patterns and cavities on the photographs in Figure 2.12. The Faraday wavelength is derived from the dispersion relation [46, 47, 91, 93]

$$\omega_0^2 = \left(gk + \frac{\sigma}{\rho}k^3\right)\tanh\left(hk\right), \tag{2.4}$$

with g the gravitational acceleration, k the wavenumber, σ the kinematic viscosity, ρ the density of the fuild, h the fluid depth, and finally ω_0 the wave frequency. One can consider the fluid depth infinite in the limit $\tanh\left(hk\right) \simeq 1$. In this deep water regime, considering capillary waves, *i.e.* Bo $<<$ 1, the forcing acceleration threshold is written [104, 105]

$$\gamma_F = 2^{4/3}(\rho/\sigma)^{1/3}\nu\omega_0^{5/3}, \tag{2.5}$$

and the Faraday wavelength is thus given by

$$\lambda_F = (2\pi)^{1/3}(\sigma/\rho)^{1/3}(f_0/2)^{-2/3}. \tag{2.6}$$

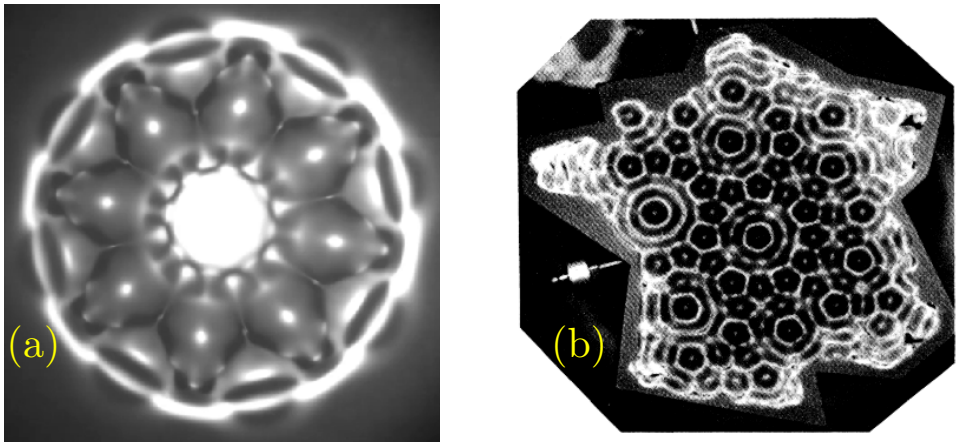

FIGURE 2.12: Faraday instability with exotic patterns. (a) An annular cavity filled with 20 cSt silicone oil was vibrated at 25 Hz. One can observe a « flower ». (b) The instability was triggered within a French-map cavity (from [92]).

When the surface of the vibrated fluid is subjected to a small perturbation, one can note two different cases depending on the forcing acceleration γ_m applied to the bath. For $\gamma_m > \gamma_F$, a perturbation is amplified, whereas when $\gamma_m < \gamma_F$, the waves generated on the bath are damped at a damping rate τ which exponentially rises with γ_m. Just below the Faraday threshold, the damping time τ diverges, there is a supercritical pitchfork bifurcation [106]. Considering now a bouncing droplet, just below γ_F, the droplet bounces at twice the period of the bath, vibrating at a Faraday period T_F. At each impact, circular Faraday waves are generated and slowly damped [107]. Note that those cylindrical waves belong to Bessel-like modes [36, 107, 108]. Consequently, the droplet is bouncing on a surface perturbed by the previously generated waves. These waves decrease in time as γ_m is a little below γ_F. One defines the memory parameter, Me, and the memory time, $\tau = \mathrm{Me}T_F$. Me is a dimensionless parameter that compares the damping time, τ, of the Faraday waves to the time, T_F, between two successive droplet bounces. Me indicates the number of secondary sources contributing to the surface wavefield. It is tuned thanks to the forcing acceleration γ_m applied to the bath, and yields

$$\mathrm{Me} \simeq \frac{\gamma_\mathrm{F}}{\gamma_\mathrm{F} - \gamma_\mathrm{m}}. \tag{2.7}$$

Since the surface of the bath is inclined when the droplet is bouncing, a horizontal momentum is transferred to the drop, which moves at a constant speed V_W which is about $V \simeq 10$ mm/s [36, 107].

2.4.2 Walking droplets

At the end, a walker is the association between a droplet and its wave. It exhibits similarities with quantum-like dynamical behaviour because of its particle-wave components. Actually, the analogy goes even further. One of the first papers on the subject from Couder illustrates that two walkers interact through their waves [109]. Two walkers can repel or attract each other. When colliding, they can orbit around each other [110, 111] similarly to rotating bound states of solitons [112, 113]. Note that, during these « collisions », there is no contact between the droplets, just a deflection of their trajectories. Somehow, walkers behave as billiard balls [114]. They undergo scattering collisions, they can form circular orbits, or even merge to form a bigger walker. Couder demonstrated that the droplet and its wave obey to the diffraction law [87]. Submarine slits were placed in a vertically vibrated cell. The latter limited the extent of the wave. The motion of the walker was investigated when passing a single or two slits. It appeared that diffraction and interference patterns were recovered, upon building the histogram of the deviations of numerous walkers. This is even more striking that these results should only be found in quantum physics [115, 116]. However, this discovery is still debated [117]. When revisiting the diffraction experiment from Couder, Andersen *et al.* obtained striking results [117], different from the analogy described by Couder. Finally another puzzling experiment of the tunnel effect was performed by Eddi *et al.* [118]. They revealed that during a collision with a barrier, the walker can be reflected or can pass through it, depending on how its waves are reflected and transmitted. The probability of passing the barrier was measured depending on the height and the width of the obstacle. It was also pointed out that when getting closer to the Faraday instability, *e.g.* when increasing the memory of the system, this probability increases.
A walker is thus a complex but surprising object. These pioneering studies revealed that a walker may show a dual character.

2.4.3 Motion equation

A first model for the particle wave interaction was proposed by Protière *et al.* [89], in the absence of barrier and external force. The equation for the drop horizontal motion is given by

$$m\frac{d^2x}{dt^2} = F^b \sin\left(2\pi\frac{dx/dt}{V_F^\phi}\right) - f^v dx/dt. \tag{2.8}$$

Equation 2.8 is derived by time-averaging the horizontal force over a single Faraday period T_F. The left hand side corresponds to the inertia of the drop, while the right

hand side corresponds to the forces exerted during the collision with the bath. The first term is the interaction of the droplet with the bath during its bouncing on the tilted surface. One has $F^b \simeq m\gamma_m(A_F/\lambda_F)(\tau/T_F)$. The collision time is written τ. The force F^b is proportional to the amplitude of the forcing acceleration γ_m, and to the slope of the surface waves, given by A_F/λ_F. The sine argument determines the phase shift between the drop, which moves at a velocity $V_W = dx/dt$, and its wave, of velocity V_F^ϕ. Finally, the second term on the left hand side describes the viscous damping resulting from the shearing of the thin air film between the droplet and the bath. In 2013, an improved version of this model was proposed by Oza *et al.* [106]. They developed an integro-differential equation of motion, upon deriving the interface height of the bath in time and space. The same assumptions are made. One denotes $\boldsymbol{x}_p(t)$ the horizontal position of the droplet at an instant t. The motion equation now yields

$$m\ddot{\boldsymbol{x}} = -mg\nabla\zeta(\boldsymbol{x}_p, t) - D\dot{\boldsymbol{x}}. \tag{2.9}$$

The drag force remains identical, but the propulsive wave force is now expressed by $-mg\nabla\zeta(\boldsymbol{x}_p, t)$. The wavefield generated by the walker reads

$$\zeta(\boldsymbol{x}, t) = \frac{A}{T_F}\int_{-\infty}^{t} J_0\left(k_F|\boldsymbol{x} - \boldsymbol{x}_p(s)|\right) \mathrm{e}^{-(t-s)/(T_F \mathrm{Me})}\mathrm{d}s. \tag{2.10}$$

The amplitude of the waves is given by the Bessel profile $J_0\left(k_F|\boldsymbol{x} - \boldsymbol{x}_p(s)|\right)$. In the section hereafter, we sum up the different works which contributed into a deep understanding of walking droplets.

2.4.4 Recent works

Collisions and orbiting walkers were also analysed [89]. It was rationalised that the diameter of the circular orbits described by two identical droplets are quantified. In particular, their diameter d_n^{orb} are related to the Faraday wavelength. One has

$$d_n^{orb} = (n - \epsilon_0)\lambda_F, \tag{2.11}$$

where $n = 1, 2, 3, \ldots$ or $n = 1/2, 3/2, 5/2, \ldots$, whether the droplets are bouncing in phase, or in phase opposition. More recently, by using a droplet launcher developed by Pucci *et al.* [119], Oza *et al.* suggested that a pair of orbiting walkers behaves as a phase-adapting oscillator [39].

In addition, other works contributed to the pioneering analogies made with quantum mechanics, such as tunneling [88, 118] and diffraction [87, 88, 117, 120]. It was found

out that a droplet trapped in a 2d harmonic central potential exhibits some Zeeman-like splitting or Landau level analogues [37, 40–44]. Droplets in cavities, in particular wavelike statistics in cavities have been developed [114, 121–123]. It was shown that the Bohr-Sommerfeld quantisation condition was satisfied, upon investigating long path-memory dynamics for which quantisation behaviours emerged [124]. Spin states have been studied [35]. In the vicinity of the Faraday threshold, the waves generated are decaying slowly in time, thus, the droplet dynamics is affected. Moreover, in these conditions the droplet is strongly influenced by its path stored in its wavefield. It was also proved that Me has an influence on the droplet dynamics when the walker evolves in a confined geometry, *e.g.* a 2d harmonic potential [36–39].

Walkers turn out to be a nice example of a pilot-wave system, developed by de Broglie in his double-solution pilot wave theory [125, 126]. Some variants to this model were later developed by Bohm [116]. Theoretical models of pilot-wave hydrodynamics were reviewed by Bush [35]. Recently, Faria achieved further developments in this model [127]. Important numerical works have been made by Milewski *et al.* [128]. With a model of weakly viscous quasipotential wave generation and evolution, they recovered preliminar features, already observed by Protière *et al.* and Borghesi *et al.*, such as orbits and promenade mode [111, 129].

Despite all these curious similarities between walkers and quantum systems [130, 131], one can find some rebuttal evidence that reveals that the dynamics of a walker is actually far from the quantum world. Several differences were highlighted these recent years. A first notable difference is that the droplet trajectory through slits can be measured without perturbation, which is impossible in quantum mechanics. Secondly, the walker is observed in a macroscopic system. Otherwise, a walker is an open system. The bouncing states are ruled by hydrodynamic equations, which are not conservative. There is also an important dissipation of energy, but it is sustained by an external forcing. This dissipation is compensated by the propulsion mechanism that occurs at each impact. In addition, the de Broglie relation gives $p = \hbar k$, which develops the dependence of the speed with the wavelength, whereas for a walker, its wavelength is imposed by the forcing conditions.

Finally, it is clear that a walker is a topic of discussion and debate. It keeps fascinating the scientific community and several questions are still unsolved. It remains a curiosity to see how it reflects quantum world while it comes out the macroscopic world.

2.5 Problem statement

In the different studies we presented here, all share the same similarity about confinement. The droplets have been confined in 2d, by using a cavity [121, 122], some Coriolis force [41, 42, 132], or even harmonic potential [42, 132]. However, one should note that a little work based on a 1d confinement has been done by Chu *et al.*. They demonstrated that upon confining a droplet in a quasi 1d setup, a droplet exhibited bouncing and glided motion [45]. They showed that, in the vicinity of the nodes of the Faraday wave, a droplet could even slow down or be trapped because of the alternatively changed slope. The Faraday instability evolving in a 1d system has recently been analysed by Nachbin *et al.* [133]. In the world of Physics, it is common to explore and understand a phenomenon in different geometries: from 1d to 3d, and even more. Our aim is to find a way to confine a droplet in 1d, in order to know, in depth, the behaviour of this system in this geometry. Can we shed light on the walker entity? Is there any puzzling analogy we can draw with this unknown 1d system? This is the purpose of the next chapter.

Chapter 3

From 2d to 1d

In this chapter, we present our experimental setup. We give some key ingredients for the experiments involving bouncing and walking droplets. We explain how to generate droplets in a reproducible and constant size. We develop our analysis protocol and explain why we work with a fixed frequency of $f = 70$ Hz. Then, we present our first experiment, which consists in confining a droplet in 1d, thanks to submerged rectangular cavities. We demonstrate that the walker dynamics within the channels shows puzzling analogies with electromagnetic waveguides.

3.1 Experimental setup

3.1.1 Overview

Our device consists in a container filled with silicone oil. In this thesis, we work with silicone oil of viscosity $\nu = 20$ cSt, density $\rho = 949$ kg/m^3 and a surface tension $\sigma = 20.6$ mN/m.Through this manuscript, containers of different geometries have been used. Here, we use a 2d square cell of section 180×180 mm^2, and other cells with channels of 120 mm length but of different widths carved into it. The widths are proportional to the Faraday wavelength λ_F. The tank is vibrated sinusoidally and vertically, using an electromagnetic shaker with a tunable amplitude A and a fixed forcing frequency $f = 70\,\text{Hz}$. The choice of this frequency is explained in subsection 3.1.4. To measure the acceleration applied to the bath, an accelerometer is fixed on the axis of the vibrating plate. It delivers a tension proportional to the acceleration in order to determine the dimensionless forcing acceleration, defined by $\Gamma = \gamma_m/g$. The acceleration Γ defines the memory time [107] $\tau_M = \tau_F\Gamma_F/(\Gamma_F - \Gamma)$ which measures

the time of persistence of the waves emitted by the walkers. To ensure purely vertical oscillations of the container and to avoid parasite effects on the walking dynamics of droplets, we use air cushions carriage that surround the vibrating axis, and guide its vertical motion similarly to Harris *et al.* [134]. A schematic of our system is given in Figure 3.1. Note that, to reduce air currents, walls are placed all around the experiment.

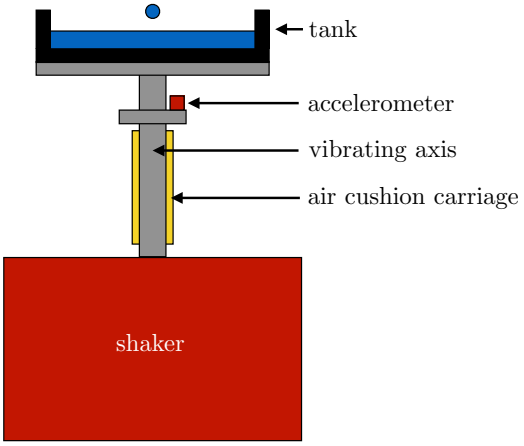

FIGURE 3.1: Sketch of the walking and bouncing droplets experiment. A tank is filled with silicone oil. A droplet, composed of the same fluid, is deposited onto the bath. The tank is vibrated thanks to a shaker. Air cushion carriage are placed around the vibrating axis to ensure a purely vertical oscillation of the device. An accelerometer glued on the axis measure the forcing acceleration applied.

3.1.2 Droplet generation

All the droplets are generated on-demand with a droplet dispenser, which was developed by Denis Terwagne during his PhD thesis [77, 104]. The dispenser is constituted of a small container filled with silicone oil. At the bottom there is a hole to expel a drop, at the top there is a piezoelectric chip. When injecting an electric impulse, a shock wave is created in the container and a droplet is evicted from the chamber. Depending on the size of the hole, the intensity of the impulse, the hydrostatic pressure, one can generate droplets of different sizes. Note that these parameters have been further analysed in this reference [135]. This method is highly reproducible. The size of the droplet is given with a precision of 1%. In this chapter, we work with droplets of diameter $2r_d = 0.8$ mm. The way to measure the size of the droplet is given in Appendix A. A schematic of the droplet dispenser is given in Figure 3.2.

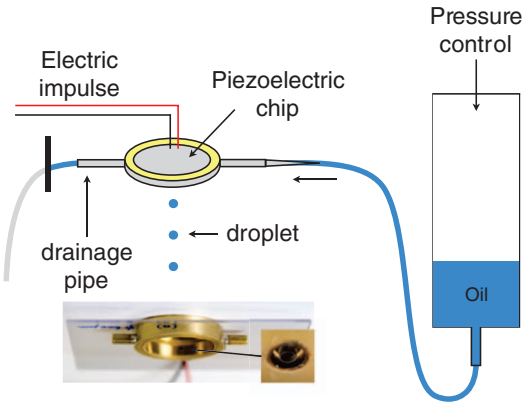

FIGURE 3.2: On the top: schematic of the droplet dispenser, on the bottom: an underneath view of the dispenser. A zoom-in focuses on the nozzle through which the droplets are expelled (from [77]).

3.1.3 Lightning, tracking and analysis

Depending on the component of the walker we want to focus on, *i.e.* the wave or the particle, different lightning types are adapted. In Figure 3.3(a), one can observe our lightning setup to enhance the visualisation of the wavefield of the droplets and more generally the waves resulting from Faraday instability. The bath is illuminated from above. Between the bath and the light, we place a 50% beam splitter. The beams from the bath and the droplets are reflected to a Pixelink camera. In addition, a diffuser with a black and white gradient printed on it is placed between the beam sampler and the light. This technique, which was used by Perrard in his thesis [136], provides a better contrast. When focusing on the particle, one uses the lightning technique illustrated in Figure 3.3(b). Here, the droplet is shot from above, and enlightened by a light inclined at roughly 45°. Upon using this setup, one can easily analyse the motion of the droplet thanks to a Python and OpenCV tracking code.

3.1.4 Choosing a forcing frequency

In literature, the experiments dealing with bouncing and walking droplets are usually performed at $f = 50$ Hz, or $f = 80$ Hz. We ran a short study to select an adequate forcing frequency. The idea was to determine a frequency for which the gap between the walking threshold Γ_W and the Faraday threshold Γ_F was maximal. Thus, in these conditions, it is experimentally easier to tune the memory parameter, because we can work with a larger range of forcing accelerations. Γ_F and Γ_W have been measured for four different frequencies from 50 to 80 Hz as function of the liquid height h, which is another primordial parameter to consider. In Chapter 2, we developed the relation

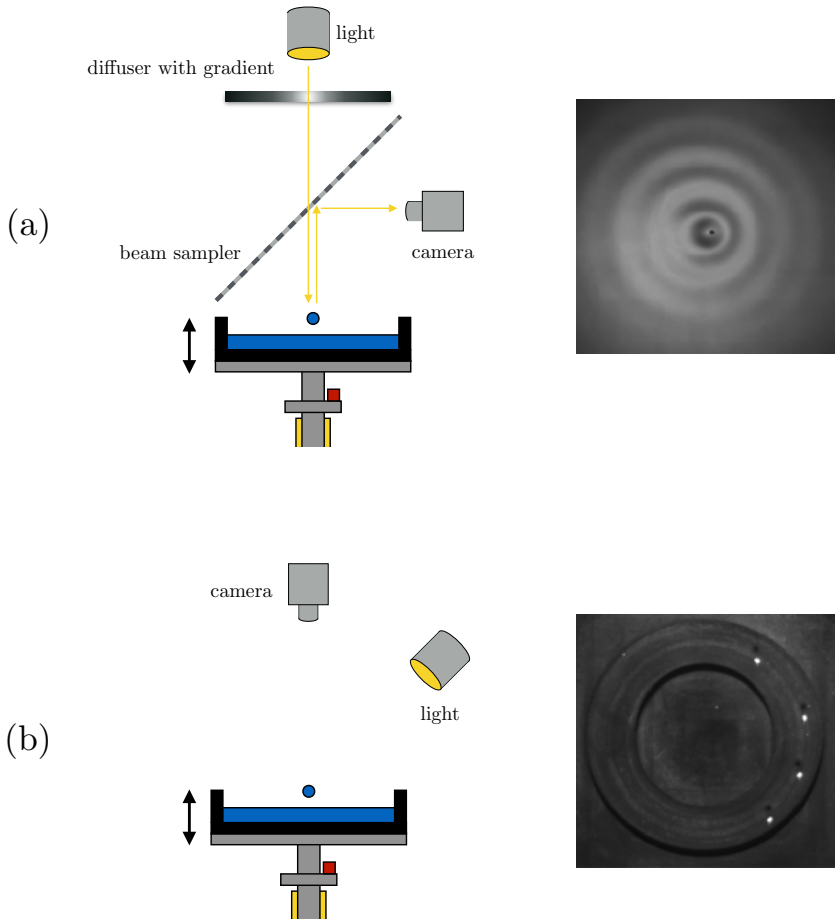

FIGURE 3.3: (a) Experimental set-up used for a visualisation of the waves, the photograph corresponds to a simple walker. (b) Set-up used to track the droplet position, the photograph illustrates an experiment involving four droplets within an annulus cavity.

dispersion, see equation 2.4. We showed that being in a deep or shallow water regime dramatically changes the dynamics of the droplet.

In this manuscript, the adimensionalised forcing accelerations are given with a precision of roughly ± 0.05, and h is given with a precision of ± 0.03 mm. In Figure 3.4, the profiles of Γ_F and Γ_W are plotted as a function of h, for different frequencies. A colour gradient illustrates the range where we can tune the memory to work with walkers, which corresponds to the interval $[\Gamma_W, \Gamma_F]$ where walkers are only observed. Those plots are drastically modified when changing the forcing frequency f. Note that, we can consider to work in deep water region when $h > 3$ mm, since the variables Γ_W and Γ_F become independent from h. When working at $f = 50$ Hz, the range over which we can observe walkers is very limited. In particular and curiously, in the deep water region, no more walker is observed. We suspect that, when working at $f = 50$ Hz, a droplet of diameter $2r_d = 0.8$ mm is too heavy to lift, and Faraday instability occurs

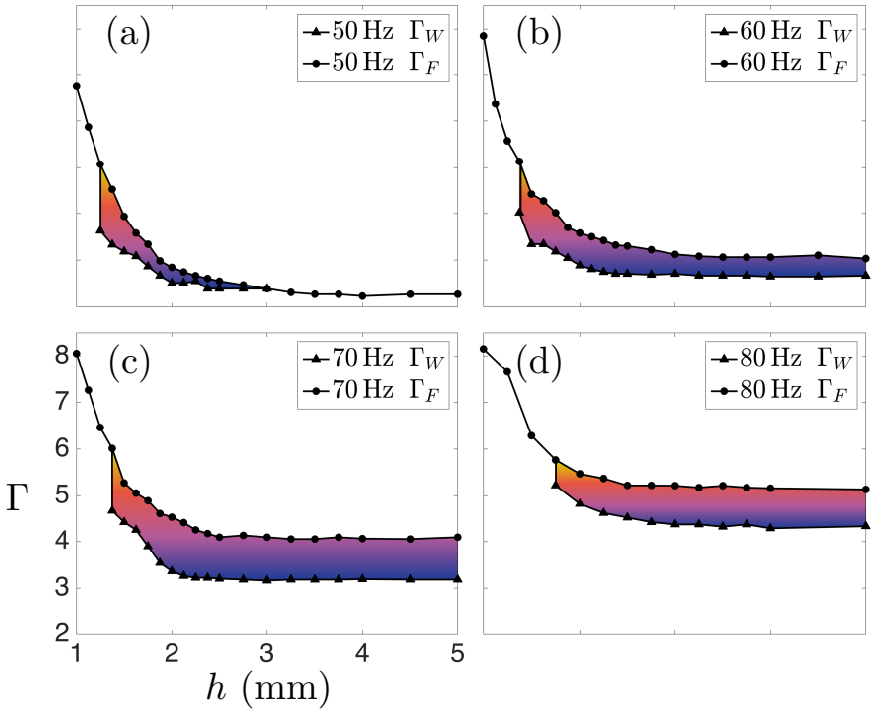

FIGURE 3.4: Evolution of the thresholds Γ_W and Γ_F as a function of the liquid height h, at $f = 50$ Hz (a), $f = 60$ Hz (b), $f = 70$ Hz (c), $f = 80$ Hz (d).

even earlier. Upon using the nondimensionalised form of equation 2.5 and dividing it by the forcing acceleration gives

$$\Gamma_F/f_0^{5/3} = \frac{1}{g}2^{4/3}(\rho/\sigma)^{1/3}\nu(2\pi)^{5/3}. \tag{3.1}$$

One should expect to obtain a constant value in deep water regime for each frequency. This is verified in Figure 3.5. One can see that all plots are reasonably gathered in the deep water regime as one can expect. Experimentally, one has $\Gamma_F/f_0^{5/3} \simeq 0.0035$. When deriving equation 3.1, one obtains $\Gamma_F/f_0^{5/3} \simeq 0.004$, which is of the same order of magnitude. However, since equation 3.1 was derived in the assumption of deep water regime, it is hardly surprising to notice the splitting of the four curves when entering the shallow water region. The gap between the Faraday and walking threshold is then quantified in Figure 3.6. The blue curve, corresponding to $f = 50$ Hz, quickly decreases with h. Above $h > 3$ mm, no walkers were observed. It seems pointless to work with $f = 50$ Hz. The purple curve, for $f = 60$ Hz, also knows a fast decay with the liquid height. However the pink (resp. yellow) curve, corresponding to $f = 70$ Hz (resp. $f = 80$ Hz) gives a more interesting result to tune with accuracy the memory parameter. One can see that $f = 70$ Hz definitely gives the largest possible interval $\Gamma_W - \Gamma_F$ in the deep water regime, which is relevant for an accurate tuning of the

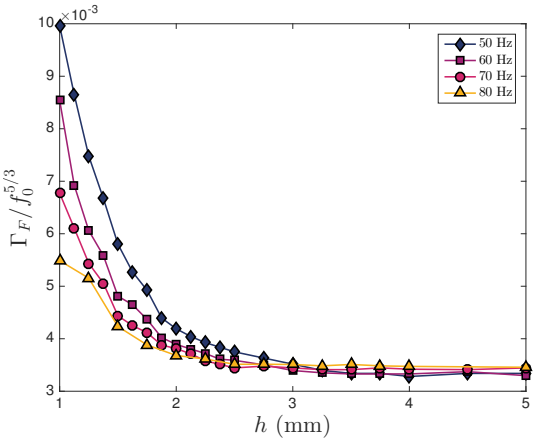

FIGURE 3.5: Evolution of $\Gamma_F/f_0^{5/3}$ as a function of the liquid height h. The four curves dramatically diminish with h, and are gathered in the deep water regime, at around $\Gamma_F/f_0^{5/3} \simeq 3.5 \times 10^{-3}$.

memory of a walker. Hereafter, we choose to work with a frequency of $f = 70$ Hz. It is of interest when performing experiments with walkers, to work in a deep water regime, so that the system becomes independent from h.

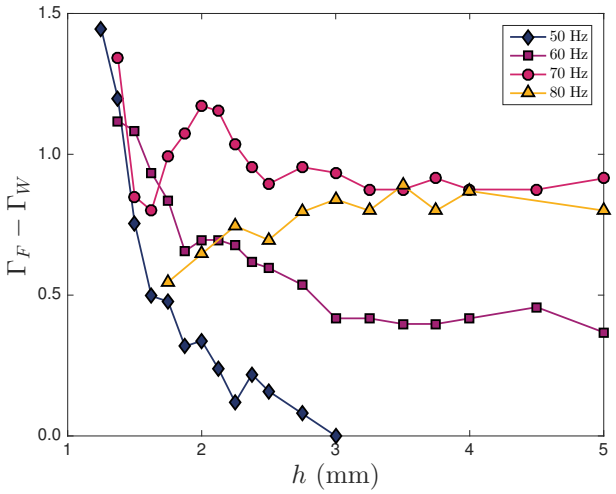

FIGURE 3.6: Difference between $\Gamma_F - \Gamma_W$ as a function of the liquid height h, at four different frequencies.

3.1.5 Evolution and measurement of the Faraday wavelength

In this paragraph, we study briefly the Faraday instability within a 2d cell. Our primal goal is to determine experimentally the evolution of the Faraday wavelength as a function of the liquid height, when working at a fixed forcing frequency of $f = 70$ Hz. This is illustrated in Figure 3.7(a). One observes that λ_F slowly increases with

h. Note that above $h > 3$ mm, λ_F remains constant, as expected within a deep water regime. Experimentally, we measured $\lambda_F = 5.3 \pm 0.1$ mm in a deep water area,

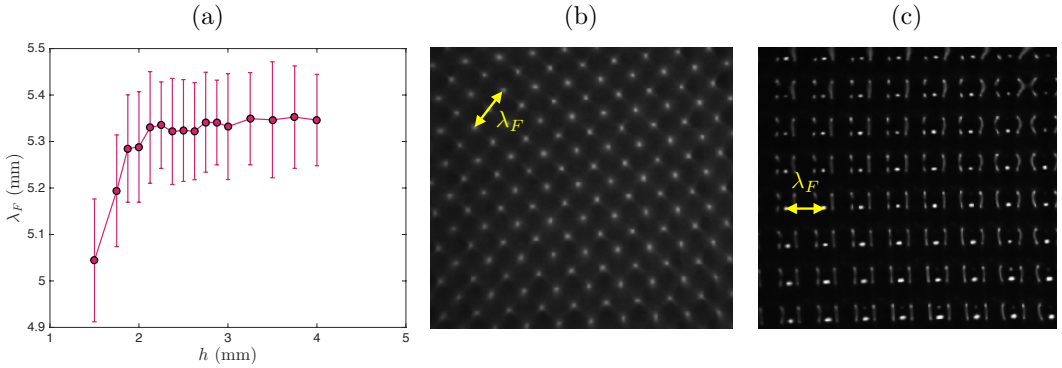

FIGURE 3.7: Faraday wavelength and Faraday instability. Evolution of the faraday wavelength λ_F as a function of the liquid height h in a 2d square cell (a). Photographs of the faraday instability at $h = 3$ mm and $\lambda_F = 5.13$ mm (b) and (c). In (b) one can visualise both nodes and anti-nodes when the FPS rate of the camera is a submultiple of the forcing frequency. When shifting a little the FPS enables us to observe nodes and antinodes separately (c).

which is in reasonable agreement with the numerical value obtained when solving the equation 2.6 that yields to $\lambda_F = 4.8$ mm. However, equation 2.6 only considers capillary waves. Taking into account gravitational waves gives an excellent agreement with our experimental value. Indeed, considering equation 2.4, in the assumption of deep water regime, gives a cubic equation in λ_F. Determining its roots provides $\lambda_F = 5.3$ mm, here the agreement is excellent. In Figures 3.7(b) and 3.7(c) are illustrated the square patterns of the Faraday instability within a 2d cell. A yellow double arrow line evidences the Faraday wavelength. Depending on the camera settings, one can observe the nodes and the antinodes separately.

3.2 Confining a droplet

3.2.1 Trapping droplets within cavities

In this paragraph, we give the ingredients and explain our method to confine a droplet in 1d, when using submerged cavities, as it is illustrated in Figure 3.8. After setting the forcing frequency at $f = 70$ Hz, one has to find a way to influence the droplet bouncing mode. A very simple method consists in working with a cell with 2 different regions where, in the first one, the droplet would behave as a walker, while in the other region, the droplet would remain in its bouncing state. One can do this very easily by tuning the liquid height h in the cell. Indeed, Carmigniani *et al.* [137] demonstrated that

modifying the depth of the fluid in the walking droplet experiment could change the value of the Faraday instability threshold Γ_F and the walking threshold Γ_W for a given frequency. In Figure 3.9 the phase diagram of the drop at $f = 70$ Hz is reported as a function of the liquid height h. Three regimes are delimited: Bouncing, Walking, and Faraday. This plot is instructive because below a critical value noted $h_c \simeq 1.5$ mm, no walker is observed. However, one notices the apparition of the Faraday instability even for a small liquid depth but for large values of Γ. Finally, in the deep liquid region: Γ_F and Γ_W are nearly independent of h. In Figure 3.9, one notes two red dots: when

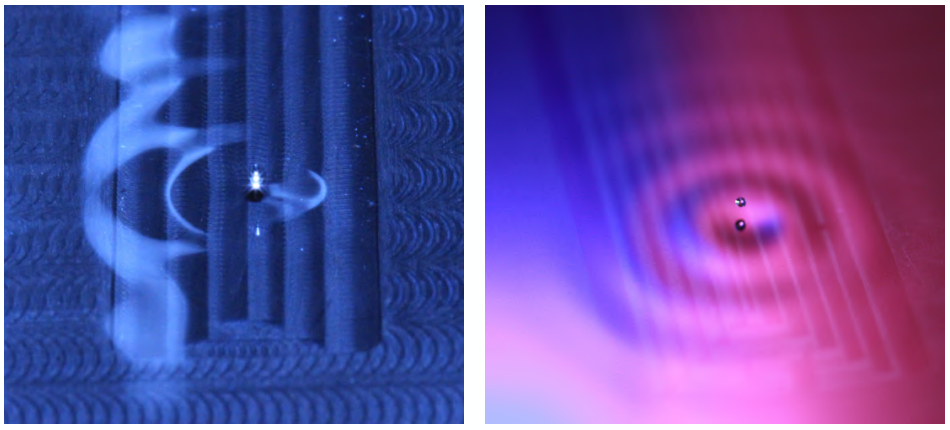

FIGURE 3.8: Photographs of droplets walking in linear cavities of different widths, $D = 2\lambda_F$ (left photograph) and $D = 4\lambda_F$ (right photograph).

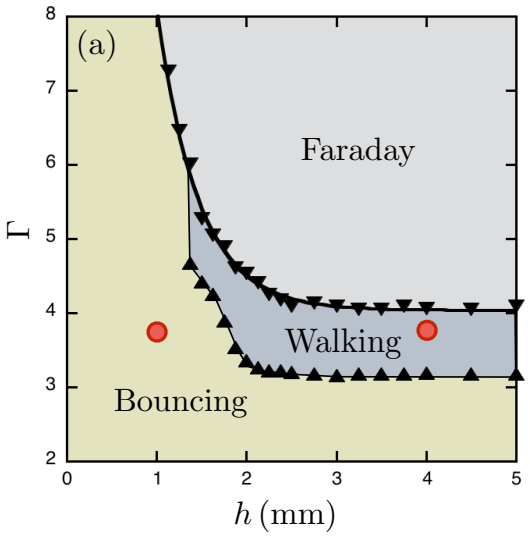

FIGURE 3.9: For $f = 70$ Hz, thresholds of the Faraday instability Γ_F (triangle down) and the walking regime Γ_W (triangle up) as a function of the liquid height h. Three regimes are distinguished: Bouncing, Walking and Faraday. Both red circles correspond to the experimental conditions: Me = 20 and the two depths used in this work. By fixing Me = 20 in a deep water regime, we ensure that the droplet remains a walker in a shallow water region.

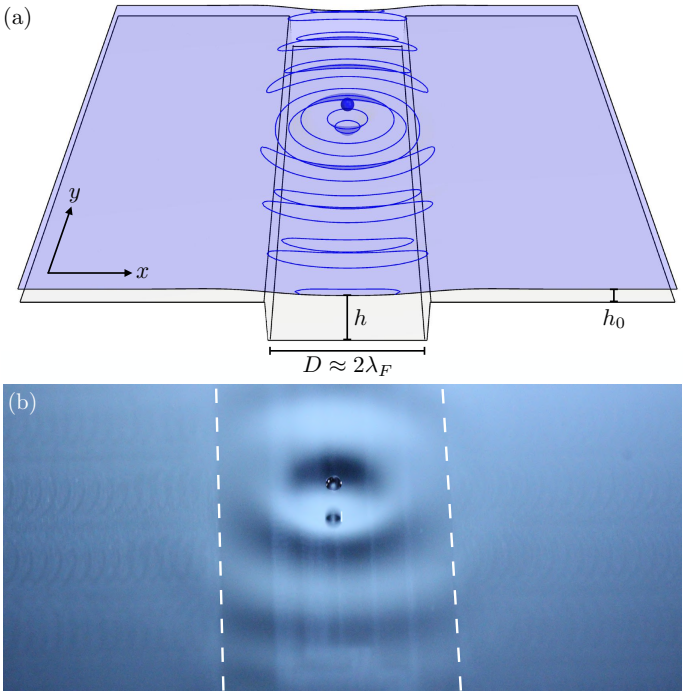

FIGURE 3.10: (a) Sketch of a rectangular cavity of width $D = 2\lambda_F$. The liquid depth is adjusted in order to have $h = 4$ mm in the channel and $h_0 = 1$ mm elsewhere. The droplet can only walk in the channel as explained in the main text. (b) Picture of a walker above a channel of width $D = 2\lambda_F$. Dashed lines indicate the channel boundaries. Faraday waves excited by the droplets are seen to be strongly damped outside the cavity.

fixing the forcing acceleration at $\Gamma \simeq 3.8$, a droplet is in its bouncing state at $h = 1$ mm, but turns to a walker for $h = 4$ mm. From the above results, we had the idea to design cavities ensuring that the droplet would remain inside. We define the faraday wavelength in a deep water region, previously measured in paragraph 3.1.5, as a control parameter for the width of the channel. The channels are finally built as follows: it consists in a rectangular cavity, carved in a square cell. The width D of the channel is proportional to the Faraday wavelength that was previously measured. The length of the channels is arbitrary fixed at $L = 120$ mm. The 180×180 mm^2 cell is filled with silicone oil, so that we obtain, within the channel a deep water region with a liquid height $h = 4$ mm. Thus, the channel is surrounded by a shallow water area, where the liquid height is noted $h_0 = 1$ mm. These two depths correspond to the two red dots in Figure 3.9. The forcing acceleration used $\Gamma \simeq 3.8$ corresponds to a memory parameter of $\mathrm{Me} = 20$. In Figure 3.10(a), a sketch of the channel is provided. Finally, we ensure that the droplet can walk in the channel but stays as a bouncing droplet outside the cavity, because of the height difference, accordingly to our results in Figure 3.9. In Figure 3.10(b), one can see a photograph illustrating that the droplet is walking and remaining within a channel. One can observe the wavefield, which can propagate within

the cavity, while it is quickly damped outside. Finally, different channels have been created with different widths D, from $D/\lambda_F = 1/2$ up to 6. In all cases, the droplet is confined in the cavity. In Figure 3.11, the dependence of both thresholds is plotted as a function of the nondimensionalised channel width D/λ_F. We note that, for large channels $D/\lambda_F > 3$, Γ_F and Γ_W do not vary with the channel width and their values correspond to those obtained for a square cavity in the deep water region, as shown in Figure 3.9. Nevertheless, in smaller cavities such as $D/\lambda_F < 3$, one can observe that the thresholds Γ_W and Γ_F depend on the width of the channel. Consequently, it is necessary to re-adjust the forcing acceleration according to the evolution of both thresholds in each respective channel, to ensure a fixed memory parameter. In our experimental protocol, Γ is tuned so that $\mathrm{Me} = 20$ is kept constant in the experiments that we present in the following section.

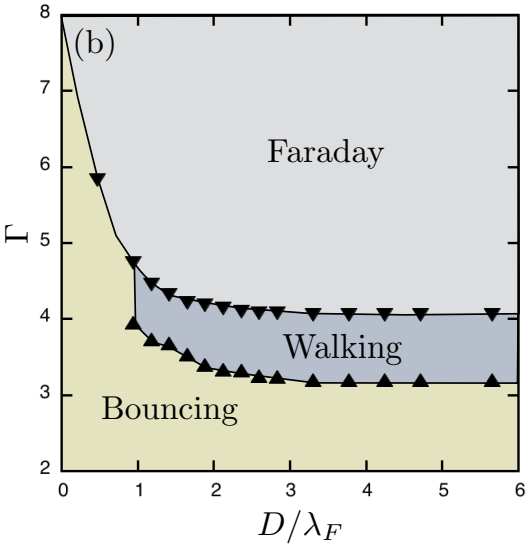

FIGURE 3.11: Thresholds of the Faraday instability (triangle down) and the walking regime (triangle up) as a function of the nondimensionalised channel width D/λ_F. The three regimes are depicted: Bouncing, Walking and Faraday. Herein, the liquid height is fixed at $h = 4$ mm.

3.2.2 Walkers trajectories and Faraday instability

In this subsection, we focus on the trajectories of walkers in the different linear cavities. At first, we observed that for $D/\lambda_F < 1$, the channel is able to pin the droplet which remains immobile, and only bounces on the surface. Walking droplets are only found for $D/\lambda_F \geq 1$. Typical trajectories are drawn in Figure 3.12 for $D/\lambda_F \simeq \{1.5, 2, 4, 5.5\}$. In narrow channels, the walker follows a rectilinear back-and-forth motion at a constant speed. When the droplet reaches an extremity, it is reflected. For wider channels, the

situation is completely different since the droplet jiggles, as it is evidenced in Figure 3.13. Tortuous trajectories with several reflections on the sides of the cavity are seen. By increasing the width, the x component of the droplet velocity becomes more and more important. It should be equivalent to the y component for an isotropic and large system. We note that for narrow channels the droplet is never perfectly centred. In the experiments involving droplets, experimentalists are worried about the presence of air currents that may affect dramatically the dynamics of the droplet [136]. This is why we placed walls all around the entire experimental setup. The experiment was then driven upon rotating the cavity by $\pi/2$ and similar results were obtained. Therefore, we assume that air currents are not the major cause for the wobbling motion and the displacement of the droplet from the center of the channel in the narrow ones.

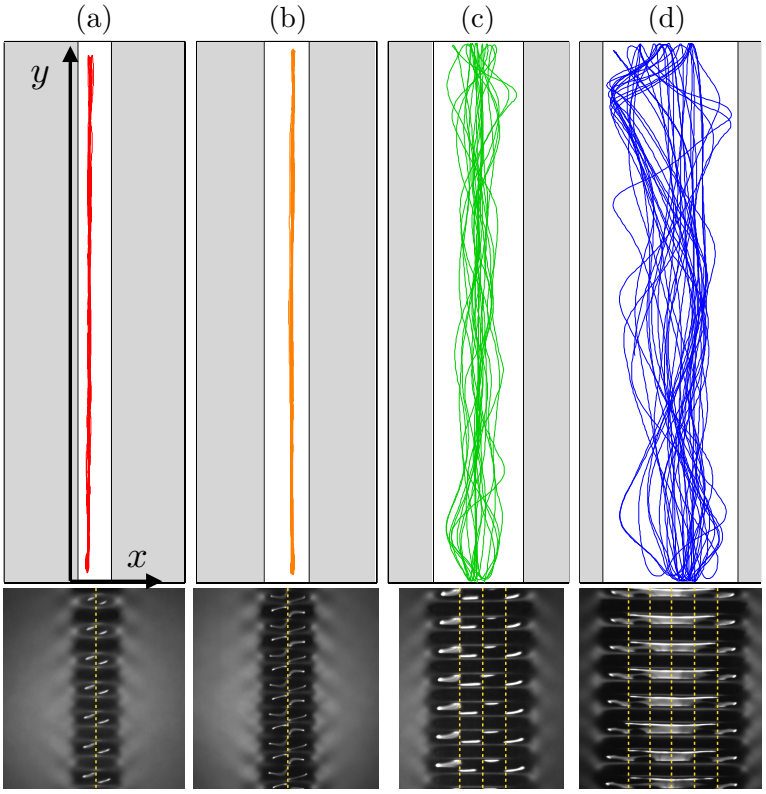

FIGURE 3.12: (Top row) Typical trajectories of a walker in four channels: $D/\lambda_F \simeq 1.5$ (a), $D/\lambda_F \simeq 2$ (b), $D/\lambda_F \simeq 4$ (c), $D/\lambda_F \simeq 5.5$ (d). In the first two narrow cavities (a) and (b), the walker follows a linear path. The droplet has a back and forth motion with a constant speed along the y-axis. In the wider cases (c) and (d), the walker is wobbling and oscillations are seen in the transverse direction, *i.e.* in the x direction. (Bottom row) Pictures of the Faraday pattern obtained in the corresponding upper cavities when the acceleration Γ reaches Γ_F. One can observe evanescent waves outside the channels. The Faraday periodic pattern is only observed along the y axis. The pattern corresponds to a bump along the x axis, where the Faraday wavelength λ_x slightly differs from λ_y. A secondary light source placed close to the liquid bath evidences a periodic substructure along the x axis, emphasised by yellow dashed vertical lines.

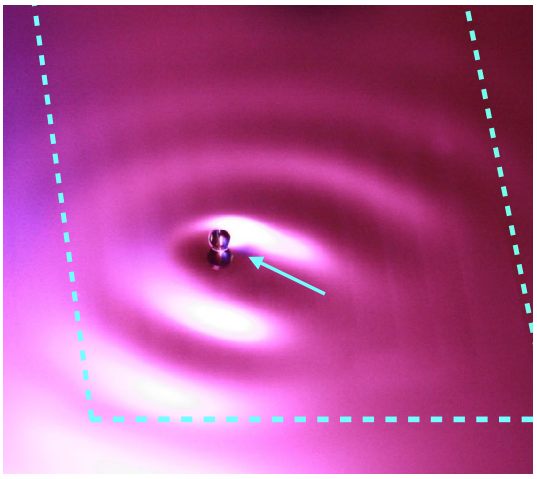

FIGURE 3.13: Photograph of a walker jiggling within a linear channel of width $D = 4\lambda_F$. The borders of the cavity are evidenced thanks to the dashed blue line. The arrow blue line reveals that the walker is not following a straight path.

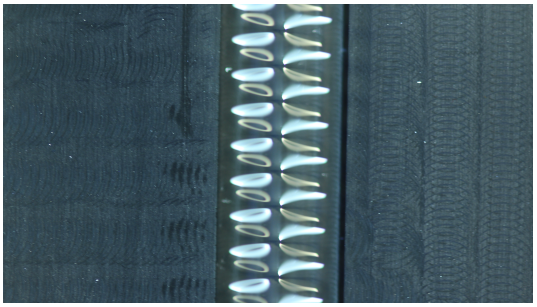

FIGURE 3.14: Faraday instability within a 1.5 λ_F channel. One can guess the nodal line at the middle of the channel that splits an antinode of large amplitude from another antinode of lower amplitude.

Since the successive impacts of the bouncing droplet on the surface are exciting Faraday waves, we explored the Faraday pattern into the different rectangular cavities. The forcing acceleration was cranked up until the emergence of Faraday waves. Pictures at the onset of the Faraday regime are shown in Figures 3.12 and 3.14. Instead of the square patterns found in large tanks, we observed line patterns oriented along the transverse direction of the narrow cavities. The line spacing along the longitudinal direction corresponds roughly to λ_F. Those patterns look similar to those obtained by Pucci and coworkers in the case of worm-like floating droplets [138, 139]. We conclude at this point that a single mode of wave propagation could exist in narrow channels since only transversal structures are observed for Γ close to Γ_F. Outside the channel, in the transverse direction, one can notice evanescent Faraday waves, which are strongly damped, according to our results of Figure 3.9. Strictly considering line wave patterns, it is hard to understand why a droplet starts to wobble for wide channels. A secondary

light source has been placed close to the experiment in order to visualise the substructure of nodal lines which are evidenced with yellow dashed lines in Figure 3.12. One can notice that the second light has to be tilted enough to obtain a proper visualization of the nodal lines inside the channels. They are undulated with a wavelength close to λ_F along the transverse direction. Note that λ_x differs from λ_y. This is illustrated in Figure 3.15. We note that the ratio λ_x/λ_y evolutes around 2. This puzzling result reveals the auto-adaptative character of the Faraday instability within the channels. We also note a remarkable feature: the number n_l of nodal lines is found to be odd in those channels. This implies that an integer (and not half-integer) number of spatial wave oscillation periods is always realised in our experiments. This peculiar property is exploited and discussed in more detail in section 3.3. The number of nodal lines will affect the transverse speed as shown below.

3.2.3 Droplet speed and energy ratio

In the following, we study the transverse and longitudinal speed of a walker in the channels. In Figures 3.16(a) and 3.16(b), one can observe the temporal evolution of the walker speeds in a $D/\lambda_F \simeq 3$ channel. The trajectory of this walker is reported in Figure 3.16(c). One can observe that the droplet wobbles a little in the channel. The longitudinal speed v_y evolves between $\langle v_y \rangle = \pm 10.16$ mm/s with fluctuations. We can consider the droplet speed to be constant since it shifts from $+\langle v_y \rangle$ to $-\langle v_y \rangle$ quasi instantaneously. In the following, when the average speeds $\langle |v_y| \rangle$ and $\langle |v_x| \rangle$ are calculated, the data corresponding to the backwards motion of the droplet are removed

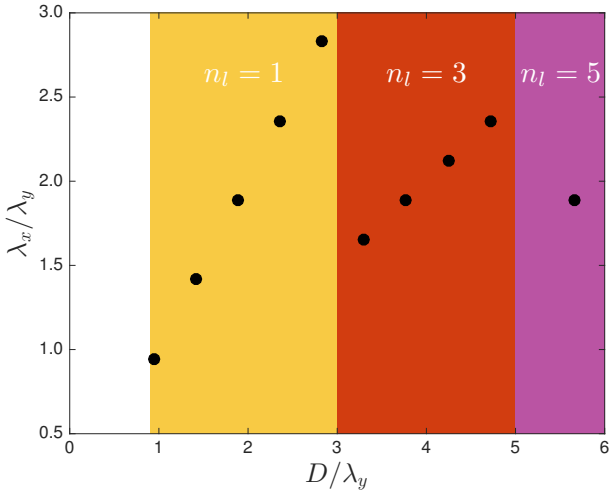

FIGURE 3.15: Evolution of the ratio λ_x/λ_y as a function of D/λ_y. Three regions of different colours denote the number of nodal lines n_l which is found to be odd in the linear channels.

to limit the large fluctuations and to properly estimate the average speeds. In Figure 3.16(a), one can notice that at $t = 50$ s, the speed does not reach $+\langle v_y \rangle$ immediately. This is simply due to an interaction of the walker with the lower left border of the channel, see Figure 3.16(c).

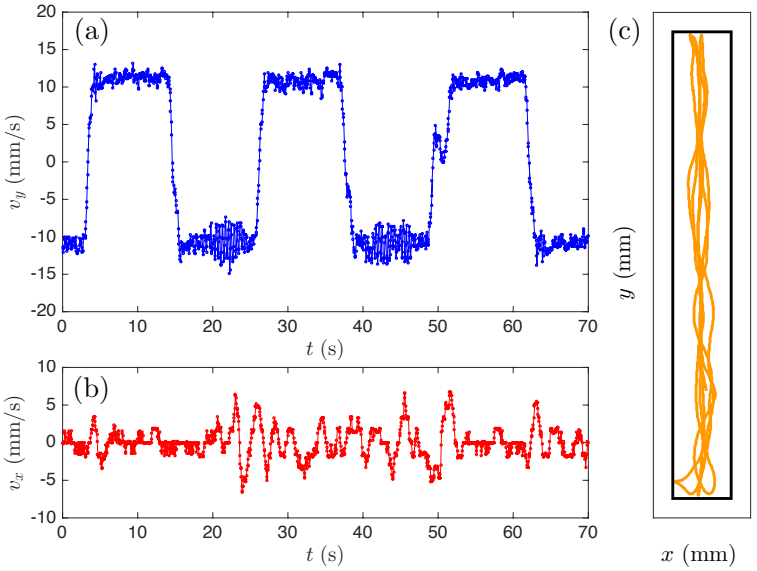

FIGURE 3.16: (a) Evolution of the longitudinal speed v_y and (b) transversal speed v_x of a walker as a function of time, in a channel of $D/\lambda_F \simeq 3$, and (c) its associated trajectory. Colours correspond to those of the trajectories shown in Figure 3.12. The average speeds are: $\langle |v_y| \rangle = 10.16$mm/s, and $\langle |v_x| \rangle = 1.49$ (mm/s).

In order to quantify the walker dynamics in channels, we consider the average speed along the longitudinal and transversal directions: $\langle |v_y| \rangle$ and $\langle |v_x| \rangle$, as a function of the channel dimensionless width D/λ_F. The results are shown in Figure 3.17(a) and 3.17(b). One observes that, along the y-direction, the velocity is equal to zero for channels with $D/\lambda_F \leq 1$. As the width increases, the velocity suddenly grows to reach, for $D/\lambda \gtrsim 3$, a constant value, namely the velocity of a walker in a 2d cell without boundary effects. The behaviour is different along the x direction. $\langle |v_x| \rangle$ has an almost constant value for $1 < D/\lambda_F < 2$ while it steadily increases with D for $D/\lambda_F > 2$. One expects to obtain $\langle |v_y| \rangle = \langle |v_x| \rangle$ for infinitely large channels since one recovers, in this case, the 2D walker dynamics. The evolution of $\langle |v_y| \rangle$ with D is described later in this chapter thanks to an electromagnetic wave-guide analogy. The evolution of $\langle |v_x| \rangle$ seems to be linked to the Faraday instability as discussed before. Indeed, when only one nodal line is observed (*i.e.* $n_l = 1$, which corresponds to one wavelength in the transversal direction), $\langle |v_x| \rangle$ is constant and only changes when two new nodal lines appear (*i.e.* $n_l = 3$, which corresponds to the emergence of a second wavelength along the transversal direction) for $D/\lambda_F = 3$. Note that the subsequent growth of $\langle |v_x| \rangle$

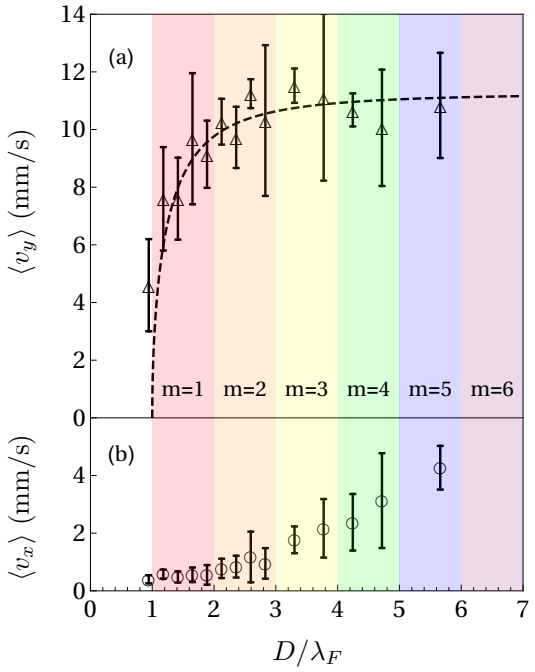

FIGURE 3.17: (a) Evolution of the average longitudinal speed $\langle |v_y| \rangle$ and (b) average transversal speed $\langle |v_x| \rangle$ of a walker as a function of the dimensionless parameter D/λ_F. The black dashed curve is a fit using equation 3.6. Different colours denote different propagation modes noted m, defined in section 3.3. Colours correspond to those of the trajectories shown in Figure 3.12.

is slightly less pronounced for $2 < D/\lambda_F < 3$ than for $D/\lambda_F > 3$. We attribute this to the fact that in this particular interval of channel widths a single nodal line along the center of the channel is still most often encountered, while the theoretical model developed in the next section would in principle allow also for the excitation of the subsequent mode exhibiting three nodal lines. This type of restriction is expected to become less effective for wider channels with $D/\lambda_F > 3$. Since the main application of narrow cavities is the path control of walkers, the relevant question concerns the choice of the optimal width D for limiting the speed fluctuations along the transverse axis. Figure 3.18 presents in a semi-log plot the ratio of the average kinetic energies measured along the x and y directions, *i.e.* the ratio $\langle v_y^2 \rangle / \langle v_x^2 \rangle$, as a function of D/λ_F. As expected, a peak is observed around $1.5 \leq D/\lambda_F \leq 2.25$. It should be noticed that the ratio reaches values above 100. One can consider this range as optimal widths to perform 1d experiments with walkers, in our conditions.

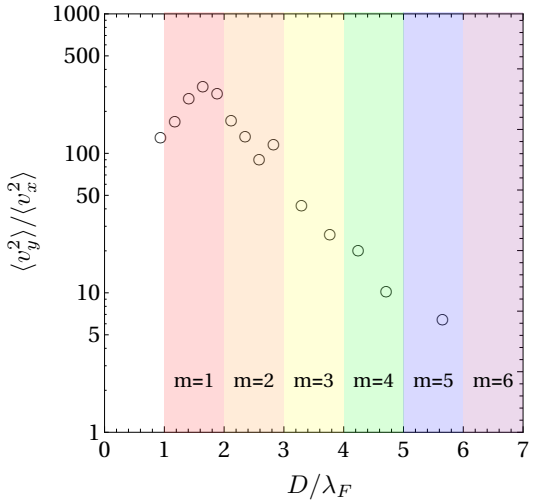

FIGURE 3.18: Ratio of the kinetic energies in a semi log-scale as a function of the dimensionless width D/λ_F. The ratio reaches a maximum at approximately $1.5 < D/\lambda_F < 2.5$. For very large D/λ_F values, we expect that the ratio tends to 1 due to the equiprobability of the droplet motion in both directions.

3.3 Discussion

The above observations can be qualitatively captured by means of a simplified theoretical description of the Faraday waves that are emitted by the bouncing droplets [120]. In a confinement-free configuration, a single bounce of a droplet at the position $\mathbf{r}_0 = (x_0, y_0)$ gives rise to a periodically oscillating surface wave profile of the form [44, 81]

$$\zeta(\mathbf{r}, t) = \mathcal{A} J_0(k_F|\mathbf{r} - \mathbf{r}_0|)\cos(\omega t/2)e^{-t/\tau_M}, \tag{3.2}$$

which decays with a rate $1/\tau_M$ that is inversely proportional to Me. We neglect here the occurrence of a spatial attenuation $\propto e^{-|\mathbf{r}-\mathbf{r}_0|/\delta}$ of the surface waves, which is encountered in droplet experiments [44]. The Bessel function of the first kind J_0 arising in equation (3.2) can be understood as representing the imaginary part of the retarded Green function $G(\mathbf{r}, \mathbf{r}_0, k_F)$ that is associated with the two-dimensional Helmholtz operator [120], that satisfies the equation

$$\left(\frac{\partial^2}{\partial x^2} + \frac{\partial^2}{\partial y^2} + k_F^2 + i0\right) G(\mathbf{r}, \mathbf{r}_0, k_F) = \delta(\mathbf{r} - \mathbf{r}_0)\,. \tag{3.3}$$

We then have

$$\begin{aligned} J_0(k_F|\mathbf{r} - \mathbf{r}_0|) &= -4\mathrm{Im}[G(\mathbf{r}, \mathbf{r}_0, k_F)] \\ &= \frac{1}{\pi}\int d^2k\,\delta(k^2 - k_F^2)e^{i\mathbf{k}\cdot(\mathbf{r}-\mathbf{r}_0)}, \end{aligned} \tag{3.4}$$

which, when inserted into equation (3.2), indicates that only those waves $\propto e^{i\mathbf{k}\cdot(\mathbf{r}-\mathbf{r}_0)}$ persist whose wave vectors $\mathbf{k}$ satisfy the Faraday wave condition $|\mathbf{k}| = k_F = 2\pi/\lambda_F$.

The Faraday wave profile expressed in equation 3.2 will be modified in the presence of sub-surface channels. This modification implies the hypothesis that Faraday waves are still characterised by the same wavenumber k_f in the presence of the boundary conditions. Under these assumptions, the Green function has to satisfy the Helmholtz equation, see equation 3.3. Inspecting the experimentally obtained surface wave profiles that are depicted in the lower panels of Figure 3.12, we infer that the Faraday waves emitted by a droplet in a channel approximately satisfy the Dirichlet boundary conditions at the lateral borders of the channel, yielding the condition $G(\mathbf{r}, \mathbf{r}_0, k_F) = 0$ at $\mathbf{r} = (x, y)$ with $x = 0$ and $x = D$ for the Green function of the Helmholtz equation. We define the horizontal coordinate system such that the channel lies within $0 < x < D$. They furthermore appear to exhibit a nodal line at the channel's centre at $x = D/2$ as can be seen again in Figure 3.12, which is presumably required to allow for a stable droplet motion within the channel. We can then expand the Green function within the lateral channel eigenmodes

$$\chi_m(x) = \sqrt{\frac{2}{D}} \sin\left(\frac{2m\pi x}{D}\right), \tag{3.5}$$

satisfying the Dirichlet boundary conditions and $(-\partial^2/\partial x^2)\chi_m(x) = k_m^2 \chi_m(x)$ with $k_m = 2m\pi/D$, and exhibiting a node at $x = D/2$. This then yields a superposition of longitudinal waves of the form $\chi_m(x)\exp(ik_y^{(m)}|y - y_0|)$ with $k_y^{(m)} = \sqrt{k_F^2 - k_m^2}$ for $0 < m < D/\lambda_F$, complemented by another superposition of evanescent waves of the form $\chi_m(x)\exp(-\kappa_y^{(m)}|y - y_0|)$ with $\kappa_y^{(m)} = \sqrt{k_m^2 - k_F^2}$ for $m > D/\lambda_F$ the influence of which can be safely neglected. As a consequence, surface waves cannot be sustainably excited within too narrow channels whose widths $D < \lambda_F$ are below the Faraday wavelength. This in turn inhibits the walking of droplets within such narrow channels, which is in excellent agreement with our experimental findings. It is now straightforwards to infer that the walking speed v_y of the droplet within the channel is proportional to the effective wave number that characterises the longitudinal Faraday wave pattern along the channel, as this particular wave number determines the slope of the surface wave profile through which the droplet is horizontally accelerated upon impact. We should note that the speed of the droplet is governed not only by the wave number but also by the amplitude of the emitted surface waves. However, the quantitative evolution of the latter is rather involved as it requires a new profound understanding of the decay process of surface waves outside the channel, which is beyond the scope of this chapter. In the particular case of channels whose widths satisfy

$\lambda_F < D < 2\lambda_F$, this effective wave number is evidently given by $k_y^{(1)} = \sqrt{k_F^2 - k_1^2}$ as only the lowest channel mode χ_1 can be excited in that case. This yields the longitudinal walking speed

$$v_y = \pm v_y^{(0)} \sqrt{1 - \left(\frac{\lambda_F}{D}\right)^2}, \tag{3.6}$$

where $v_y^{(0)}$ is a characteristic speed scale of the droplet without constraints, *i.e.* the speed of a droplet in 2d.

Equation 3.6 is fitted on the data of Figure 3.17(a), yielding as sole free parameter $v_y^{(0)} = 11.9$ mm/s, which roughly corresponds to the speed for droplets in 2d which equals $v^{2d} = 12.4$ mm/s. The fit is in good agreement with our experiments, even for $D > 2\lambda_F$. This is attributed to the fact that the longitudinal speed of the droplet is predominantly governed by the largest variation of the Faraday wave along the channel, and the latter would be provided by the lowest transverse mode χ_1. The transverse speed v_x, on the other hand, should be determined by the highest transverse mode that enters into the superposition of modes constituting the Faraday wave profile, since this particular mode provides the largest wave profile variations across the channel. We should generally expect $|v_x| \propto m$ where $m = m_{max}$ is the largest integer that satisfies $m < D/\lambda_F$. This expectation is roughly satisfied as we can see in Figure 3.17(b). There are, however, significant deviations due to the fact that in practice this highest transverse mode $\chi_{m_{max}}$ hardly ever participates in the experimentally observed Faraday wave profile, as we saw in Figure 3.12. A more elaborate theoretical framework, taking into account the decay of Faraday waves outside the channel in a more quantitative manner, is certainly needed in order refine the model under consideration and thereby obtain a more detailed understanding of the behaviour of walking droplets in channels.

The functional form of equation 3.6 is similar to the behaviour of the electrons in quantum wire systems. The particles are confined along a direction while they are free to move in the other one. In the case of carbon nanotubes, the confinement affects the speed of an electron which increases with the diameter [140, 141]. One can also establish an analogy with bosonic matter waves systems. In particular, ultra cold atoms in optical matter-wave guides constitute another example [142, 143]. The properties of the walkers dynamics is, furthermore, reminiscent of the propagation of light in rectangular electromagnetic wave-guides. In particular, one may notice the "Ray-Optics approach" used to understand the wave propagation in a guide, where the rays of light bounces on each wall. Let us compare both systems: wave-guides are usually made of two materials with refraction index n_1 and n_2. The light propagates in the medium of index $n_1 < n_2$. Afterwards, the light is focused on the guide thanks to total reflection.

In the walking droplet experiments, the two "materials" are the regions of different fluid depths which alter the propagation of the Faraday waves, as seen in Figure 3.12. The walker is constrained within the channel thanks to the differences between the Faraday thresholds. Considering two regions as medium of different refractive index is an idea that has been used by the group of Bacot *et al.* in order to study the time reversal of Faraday waves [144]. More interestingly, our analogy can be pushed further by comparing the velocity of the walker to the group velocity of the light propagating within an electromagnetic guide. Indeed for TE1 wave guides, the light group velocity is given by equation 3.6. Nevertheless, some differences occur. Indeed, the Faraday instability auto-adapts to the channel width where, in the electromagnetic case, the wavelength is an experimental fixed parameter. The comparison breaks down for large channels which should be compared to TE_n wave guides. Furthermore, this waveguide analogy does not give any explanation for the evolution of $\langle |v_x| \rangle$ with the width of the channel. Finally, the waves emitted by the droplet are standing waves while electromagnetic wave-guides consider only propagating waves. Analogies should thus be taken with caution.

3.4 Driving droplets within cavities

Thanks to this work based on droplets confinement, we have now found the key ingredients to drive a droplet along a 1d path. One can use this method to conduct a droplet within some more exotic cavity, for example a spiral, as it it is described by the picture in Figure 3.19. The spiral was built similarly to the linear channels: a deep water region with a liquid height of $h = 4$ mm, and a shallow water region of $h_0 = 1$ mm. The deep water region width was chosen so that the drop would remain confined, as demonstrated in Figure 3.18, and was fixed at $D = 7.5$ mm which roughly corresponds to $D/\lambda_F = 1.5$. The shallow water region width was arbitrary fixed at 4 mm. A photograph showing the dimensions of the spiral is shown in Figure 3.19(a). In Figure 3.19(b) one can observe the trajectory of a droplet within the spiral cavity, shown with a colour gradient. As expected, the droplet remains within the spiral. Some measurements on the Faraday instability within this cavity were performed, as it is illustrated in Figure 3.20. Contrary to the linear cavities, where the instability appears and propagates in the whole cavity at almost the same forcing acceleration, the instability within the spiral first appears at the end (*i.e.* the outside) of the spiral, at $\Gamma = 3.58$, as shown in Figure 3.20(a). This threshold is written Γ_F^{out}. Therefore, one has to consequently increase the forcing acceleration, see Figures 3.20(b) to (f), until reaching $\Gamma = 4.10 = \Gamma_F^{\mathrm{in}}$ where the instability is finally settled within the whole cavity.

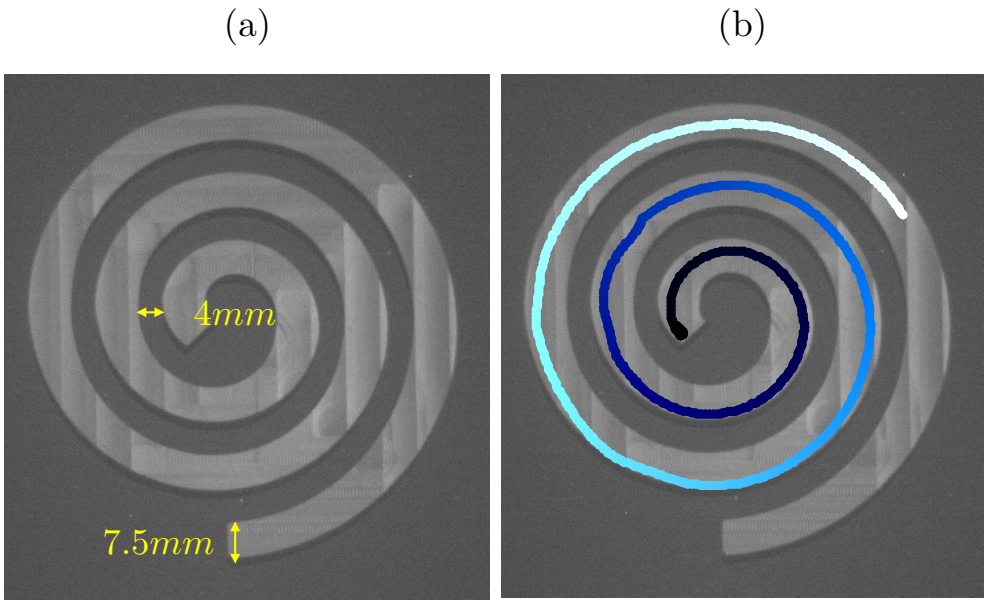

FIGURE 3.19: Two photographs of a spiral cavity. The width of the deep water region was fixed at 7.5 mm, and the shallow water region fixed at 4 mm (a). The trajectory of the droplet is described with a colour gradient (b). The white colour corresponds to the initial time of its path, and the dark blue colour corresponds to the final time of its path.

Note that, when increasing even more the forcing acceleration, the Faraday instability becomes chaotic. One can observe that the wavelengths within the spiral cavity are perpendicular to the edges of the cavity in Figure 3.20, contrary to Figure 3.21, where at some places a wavelength may appear or disappear. In the chaotic regime, the number of wavelengths is not fixed.

Working with such a cavity is not that convenient, because the gap between both thresholds Γ_F^{out} and Γ_F^{in} is considerable. Therefore, it becomes tricky to run some experiments with a walker. Below Γ_F^{out}, a droplet can walk but can hardly explore the whole spiral cavity. Besides, it is easily trapped to the edges of the channel, or it is often reflected before it goes backwards. Cranking up the memory parameter would be an alternative so that a walker may propagate within the whole cavity. However, as it is illustrated in Figure 3.20, the Faraday instability first appears at the outer border of the channel, which influences the dynamics of the walker but also disturbs its path. Consequently, a walker may go backwards in the neighbourhood of the instability, or undergo a chaotic trajectory within the instable region, where in addition, the tracking of the drop can not be successful anymore. Note that, in Figure 3.19(b), the walker could only explore a part of the cavity.

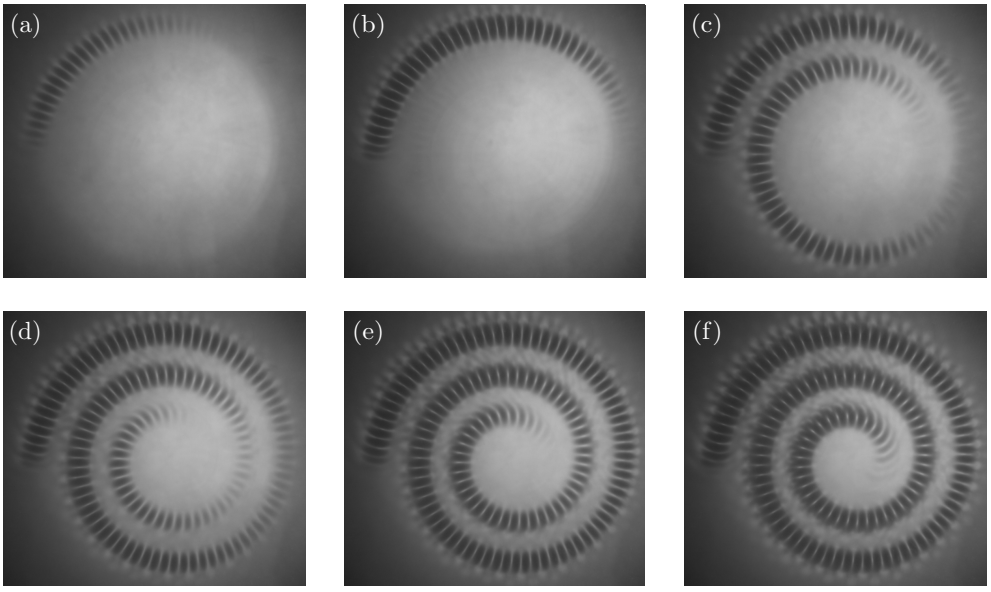

FIGURE 3.20: Photographs of the Faraday instability within a spiral cavity. One notes that the instability initially appears at the outer edge of the spiral. The forcing acceleration at this moment is written Γ_F^{out}. It progressively reaches the inner edge, when increasing the forcing acceleration until reaching $\Gamma = \Gamma_F^{\text{in}}$. On the different photographs, one has $\Gamma = 3.58$ (a) also noted Γ_F^{out}, $\Gamma = 3.68$ (b), $\Gamma = 3.78$ (c), $\Gamma = 3.82$ (d), $\Gamma = 3.92$ (e), $\Gamma = 4.10$ (f) also written Γ_F^{in}.

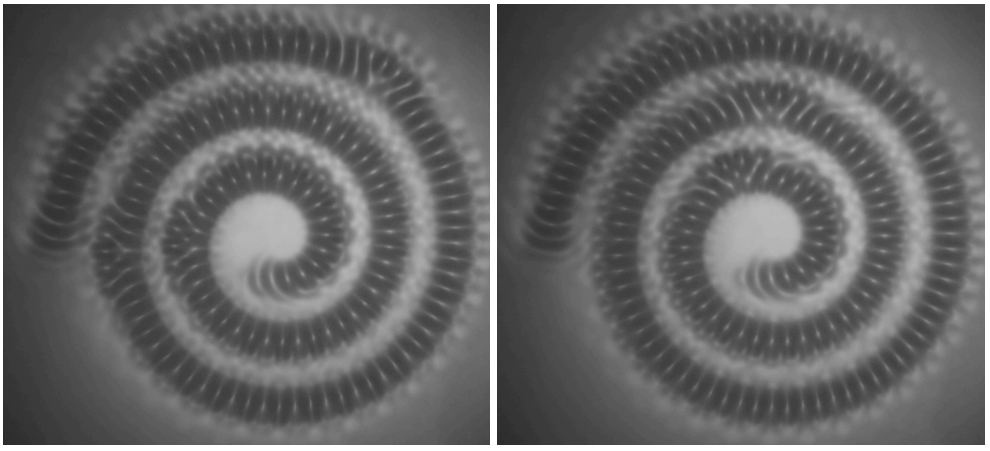

FIGURE 3.21: Two photographs of the Faraday instability within a spiral cavity. The forcing acceleration is fixed at $\Gamma = 4.52 = 1.10\ \Gamma_F^{\text{in}}$. Note that the Faraday pattern presents some irregularities, and is not stationary. At some places, additional wavelengths successfully appear or disappear, which results in a variation of the number of wavelengths within the cavity.

3.5 Conclusion

In this chapter, we evidenced that it is possible to confine and transport walking droplets along 1d channels. While the longitudinal motion is dominated by a single mode, a fine structure composed of m modes is observed in the transverse direction. We discussed the similarities and differences with waveguide systems. We have shown, thanks to an energetic study, that the optimal width maximising the longitudinal speed is around $2\lambda_F$ such that applications can be designed. One can for example drive a droplet within an original cavity, such like a spiral one. In addition, upon shedding light on the following question: how straight the walker's motion can be in a 1d channel, we have performed a study that complements the works based on walkers in confined geometries. Among them, one can refer to the numerical work of Gilet [121] and the experimental work of Harris *et al.* [122] where the authors focused on the statistics of walkers in a corral cavity and cavity modes. However, exploring the spiral cavity has demonstrated that it is also important to conduct experiments using cavities where the Faraday instability appears within the whole cavity at almost the same threshold, if one wants to work with a walker that explores the whole cavity. In the next chapter, to avoid the difficulties mentioned in the case of the spiral cavity, we come back to a more classical shape: a circular cavity. In particular, we will apply our results found with the linear channels in order to confine a droplet in an annulus. We will explore as well the effects of the memory parameter on the droplets dynamics.

Chapter 4

Annular cavities

In this chapter, we present experiments involving a single droplet placed in a circular cavity. Thanks to our study of the confinement of a droplet within a 1d cavity, we ensure that we can build circular cavities where the droplet remains and follows a circular trajectory, reducing drastically any wobbling motion. First, we analyse the dynamics of the droplet within such cavity. Secondly, we study the effect of the memory parameter. We evidence different behaviours, depending on the size of the droplet, whether it is confined or not. Finally, we characterise the influence of submarine obstacles placed in a ring.

4.1 Experimental setup

4.1.1 Overview

The experimental parameters are similar to those previously described in Chapter 3. The bath is vibrated at a frequency $f = 70$ Hz. The droplets have a diameter of 800 μm. Both bath and droplets are still composed of silicone oil with a fixed viscosity $\nu = 20$ cSt. The memory parameter is fixed at Me $= 20$. The sketch of an annular cavity is given in Figure 4.1(a), with a picture of the experiment taken from above (Figure 4.1(b)), and an angle of incidence of roughly 45 degrees (Figure 4.1(c)). The cavity consists in two regions: a deep water area of liquid height $h = 4$ mm, and a shallow water area of liquid height $h_0 = 1$ mm. The width of the annular channel is $D = 7.5$ mm, similarly to Chapter 3. We suppose that the optimal width to enable confinement is similar to linear cavities. A picture of the Faraday instability in the cavity is shown in Figure 4.1(d) from above, and with an angle of incidence of around

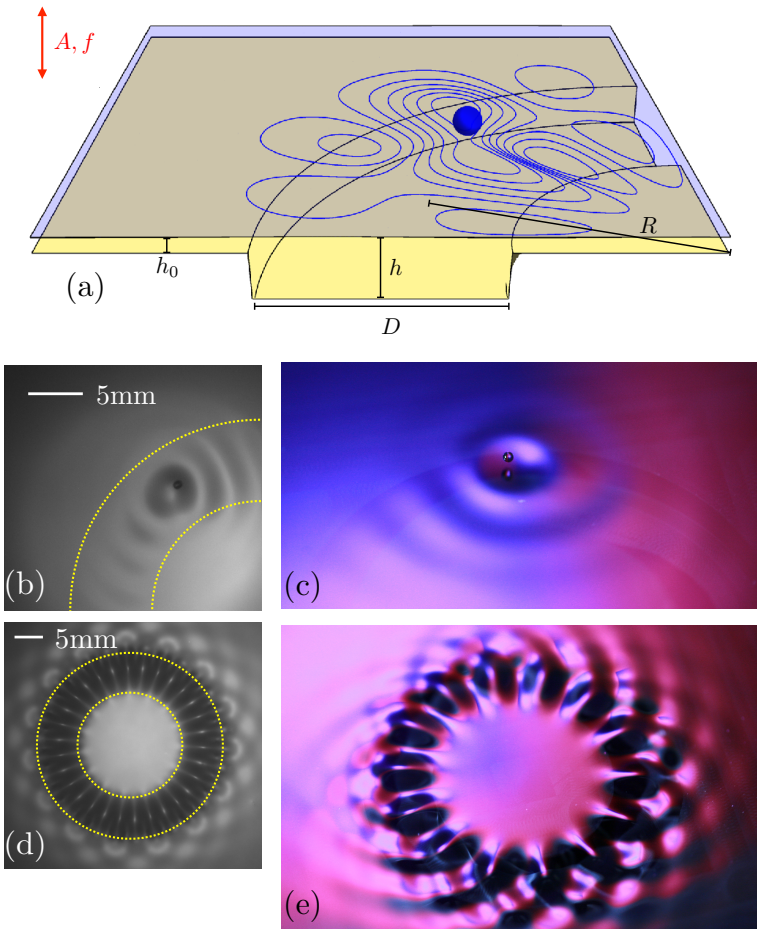

FIGURE 4.1: (a) Sketch of a quarter of the annular cavity of width D and radius R. The oil level is adjusted to obtain a depth h in the cavity and a thin layer h_0 elsewhere. A walking droplet tends to remain in the cavity. Contours of the liquid surface $\zeta(\vec{r}, t)$ are shown to illustrate that the propagation of waves mostly takes place in the cavity while evanescent waves are observed outside the cavity. (b) Photograph of the experiment from above, yellow dashed lines accounts for the channel borders. One observes the waves emitted by the walker at each impact propagating mainly along the channel for a memory $\mathrm{Me} = 20$. (c) Photograph of the experiment at an angle of incidence of about 45 degrees to better evidence wave crests. One can notice that the waves generated at each impact are quickly damped outside the annular cavity. (d) Faraday instability inside the channel above Γ_F. Evanescent waves can be observed outside the channel. (e) Photograph of the Faraday instability, at an angle of incidence of almost 45 degrees.

45 degrees to better evidence wave crests, see Figure 4.1(e). One observes the limited wave propagation outside the cavity, as well as the dependence of Γ_F regarding the fluid depth since Faraday instability takes place mainly on the cavity. Three rings of different radii have been considered with $R_{\mathrm{small}} = 13.75$ mm, $R_{\mathrm{medium}} = 41.25$ mm and $R_{\mathrm{large}} = 68.75$ mm.

4.1.2 Confining a droplet within an annulus

As shown in Figure 4.2, observations show that typical droplet trajectories in the xy-plane of single walkers are mostly circles, regardless of the size of the annular cavity, forcing parameters or memory. Please note that there is no central force behind this circular trajectory. The droplet follows the ring because the Faraday waves adopt the symmetry of the cavity (see Figures 4.1(d) and 4.1(e)). Along the ring, *i.e.* in the azimuthal direction, waves can be approximated to sinusoidal standing waves, as expected for a 1d system as illustrated in Figures 4.1(b) and 4.1(c). In the transverse direction, *i.e.* in the radial direction, the Faraday waves present antinodes in the center of the cavity and evanescent waves are strongly damped outside the ring. The droplet remains in the central part of the cavity. Moreover, the speed v of a walker is fixed by the forcing parameters of the experiment and the geometry of the cavity. We checked that the speed $v \approx 10\,\mathrm{mm/s}$ of the walker (at memory $\mathrm{Me} = 20$) is independent of the ring radius R. This may be the signature of the absence of any central force. Nevertheless, the walker speed strongly depends on the presence of boundaries, especially the fluid depth h, the channel width D, and the droplet's diameter $2r_d$. It is worth noticing that these experiments are dramatically sensitive to the horizontality of the setup. An *a priori* negligible tilting of the bath can lead to an important variation of the speed of the droplet depending on the region where it is walking. More importantly, it can even hinder the dynamics of the droplet, which may be trapped close to an edge of

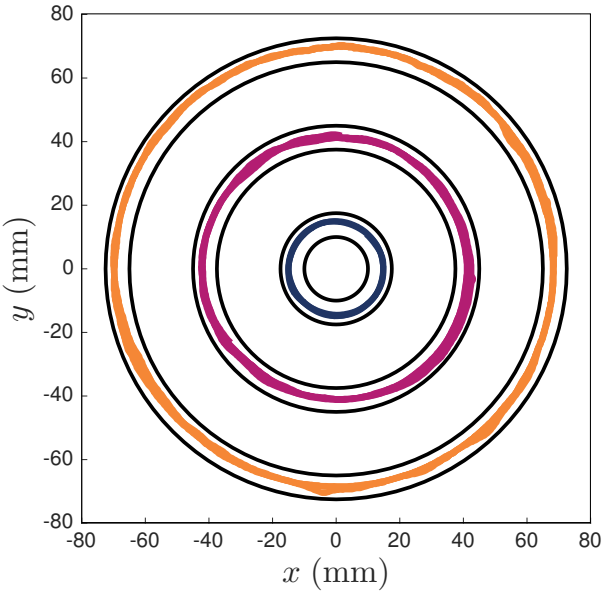

FIGURE 4.2: Trajectories of a walking droplet at $\mathrm{Me} = 20$, in three cavities of radii $R_{\mathrm{small}} = 13.75$ mm, $R_{\mathrm{medium}} = 41.25$ mm and $R_{\mathrm{large}} = 68.75$ mm. The trajectories illustrated here were recorded during a few minutes. As one could expect, the droplet is properly confined within an annular cavity, and the wobbling motion remains weak.

the cavity. We were sometimes confronted to this problem, in particular in the largest annular cavity, where the process of equilibrating the setup to ensure its horizontality could be tricky. Consequently, to avoid such troubles, it is far more convenient to work within a cavity of a reduced surface.

4.2 Effect of the memory parameter

4.2.1 Preamble

Hereafter, we present the experiments involving the influence of the memory parameter on the dynamics of the walker. In Chapter 2, we explained that the speed v of a walker undergoes a supercritical pitchfork bifurcation [106]. Thus, one expects a growth of v with an increase of Me. However, depending on the walkers' size and the geometry of the cavity, we will reveal that this expectation can be faulted.

In the coming section, we work with droplets of two different sizes. We generate large droplets of diameter $2r_d \simeq 0.9$ mm and tiny droplets of diameter $2r_d \simeq 0.7$ mm. To determine the evolution of the speed of a walker as a function the memory parameter, we consider statistics. A droplet of fixed size is created. Its velocity is successively measured at different fixed memories. The experiment is then repeated numerous times with a new droplet of the same size. This protocol was even repeated for several days to collect a large amount of numerical data points for better statistics. It is important to note that, the speed of a walker is dramatically influenced by the external factors which are sources of measurement errors, such as temperature variations, airflows, etc. Indeed, from one day to another, temperature is never fixed, and a little variation of it modifies the speed of a walker of approximately 10 %, but also the silicone oil viscosity and consequently, the Faraday threshold. In order to properly minimise these sources of error and to average our walker speed, we proceed as follows. For each day, one has to adimensionalise the speed curves obtained by a specific value v_0^∞. This speed v_0^∞ corresponds to the daily mean speed of a drop, within a specific cavity, at the largest memory parameter that we reached that respective day. Afterwards, one can gather every collected data to average the adimensionalised speed v/v_0^∞. One finally obtains the evolution of v/v_0^∞ as a function of the memory parameter Me, for large and small drops in the different cavities. For all the cavities we used, the liquid height within the deep water region is fixed, as usual, at $h = 4$ mm, and $h_0 = 1$ mm in the shallow water area.

4.2.2 Experimental results

In this section, we discuss our results involving the effect of Me on walkers trapped within 6 different cavities. At first, we use a 2d square cavity with size 100×100 mm^2, that roughly equals to $20 \times 20\,\lambda_F^2$. Secondly, we confine the droplet within an annular cavity of $1.5\,\lambda_F$ width, which corresponds to a 1d channel. The radius of the cavity is R_{small}. We increased the width of the annular cavity to $2.5\,\lambda_F$ and $4\,\lambda_F$. Finally we perform experiments in two 1d cavities: a linear channel of $1.5\ \lambda_F$ and an annular cavity of the same width, but of radius $2R_{\text{small}}$.

4.2.2.1 Square cavity

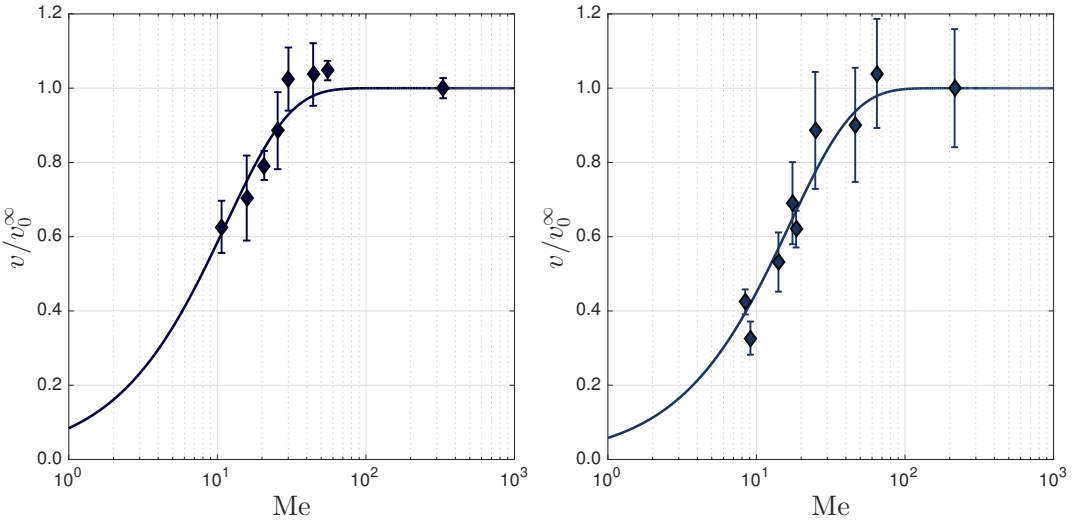

FIGURE 4.3: A semilogarithmic plot showing the evolution of v/v_0^∞ with the memory parameter Me, within a square cavity of 10×10 cm^2. The droplets diameter is $2r_d = 0.7$ mm (left) and $2r_d = 0.9$ mm (right). The curves are fitted using empirical equation 4.1.

In this first cavity, we measured the evolution of the ratio v/v_0^∞ with Me. The results are provided in Figure 4.3. One can observe that both tiny droplets (on the left) and huge droplets (on the right) follow the same trend, *i.e.* a rise of the speed with Me. This could be expected, as it is known from reference [106] that the walker's speed undergoes a supercritical pitchfork bifurcation. Both curves are fits, using the following empirical law:

$$v/v_0^\infty = 1 - \exp(-\text{Me}/\text{Me}^*), \tag{4.1}$$

where Me* is a fitting parameter. It corresponds to a typical memory for which the ratio v/v_0 saturates and becomes stationary. The speeds v_0^∞ used to adimensionalise the curves are given in table 4.1, and the fitting parameters Me* are written in table

4.2. One has respectively $v_0^\infty = 11.6$ mm/s for small droplets, and $v_0^\infty = 14.4$ mm/s for large droplets. In the following, one will see the effect of confinement on the evolution of the speed of the walker.

4.2.2.2 Annular cavity

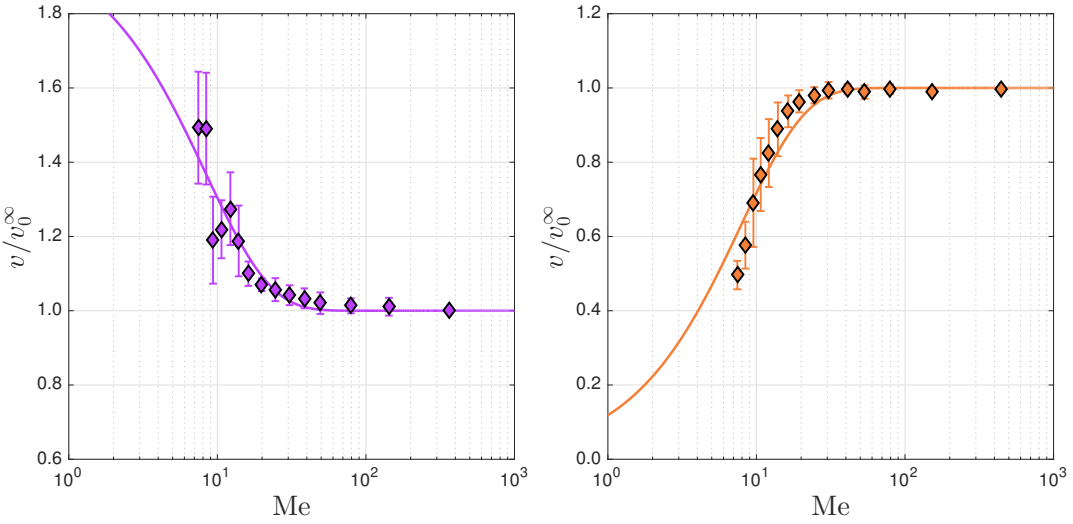

FIGURE 4.4: A semilogarithmic plot showing the evolution of v/v_0^∞ with the memory parameter Me, within a ring of width $D/\lambda_F = 3/2$ and of radius $R_{\text{small}} = 13.75$ mm. This width corresponds to a 1d guide for the drop, as it was demonstrated in Chapter 3. The droplets diameter is $2r_d = 0.7$ mm (left) and $2r_d = 0.9$ mm (right). Contrary to large walkers, the speed of tiny walkers confined in 1d, surprisingly decreases with Me. The curve on the left figure is a fit using equation 4.2, whereas the curve on the right figure is a fit using equation 4.1.

In this paragraph, we work with the annular cavity, described in section 4.1, of diameter R_{small}. The evolution of the ratio v/v_0^∞ when confining the droplets is illustrated in Figure 4.4. One has $v_0^\infty = 6.6$ mm/s for small droplets, and $v_0^\infty = 14.3$ mm/s for large droplets. For large droplets, one obtains the expected behaviour, one uses here the empirical law 4.1. However, for small droplets, one has the opposite: a decrease of the speed with the memory parameter, which may seem counterintuitive. Indeed, since Me is increased, the number of previous impacts contributing to the wavefield of the walker should be more significant and the speed of the droplet should know a corresponding growth. One first answer would be that the confinement may be responsible for the diminishment of the speed of the small walkers. The empirical fit used for the decreasing evolution of the speed of small droplets is

$$v/v_0^\infty = 1 + \exp(-\text{Me}/\text{Me}^*). \tag{4.2}$$

Only a sign differs. The value of the parameters Me^* is given in table 4.2. In the next section, we work with an intermediate ring between 1d and 2d, accordingly to Chapter 3, and with a 2d annular cavity.

4.2.2.3 Width of annular cavities

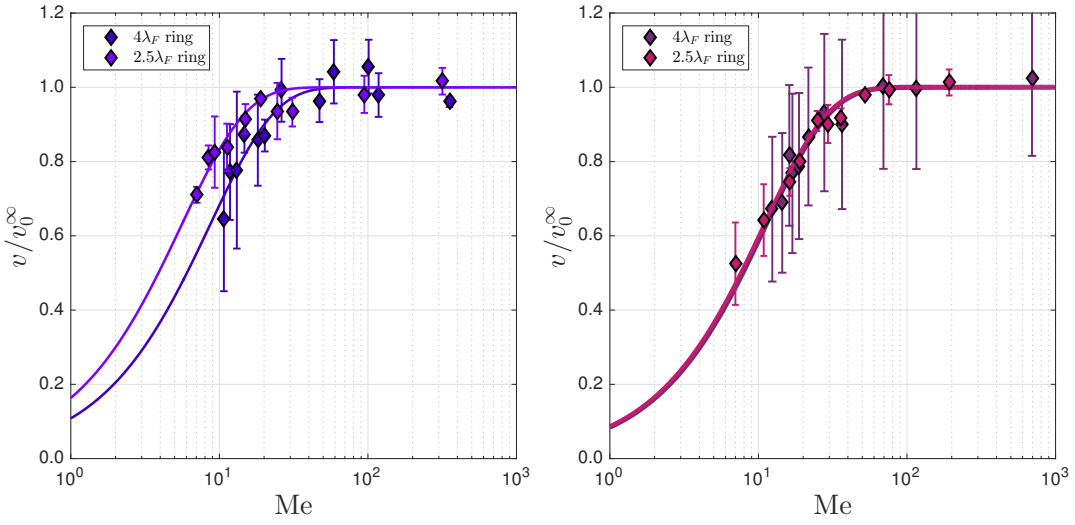

FIGURE 4.5: A semilogarithmic plot showing the evolution of v/v_0^∞ with the memory parameter Me, within a ring of width $D/\lambda_F = 5/2$ and a ring of width $D/\lambda_F = 4$. The droplets diameter is $2r_d = 0.7$ mm (left) and $2r_d = 0.9$ mm (right). The curves are fits using equation 4.1. The annular cavity of width $D/\lambda_F = 4$ corresponds to a channel where the droplet follows a 2d path, as seen in Chapter 3, while the other cavity is an intermediate between a 1d and a 2d confinement. Each plot follows the same trend.

In this section, we present experiments involving two new rings: a ring of intermediate width $D = 2.5\lambda_F$, and a 2d ring of width $D = 4\lambda_F$. In each situation, one notices the growth of the speed. For small walkers (resp. large) one has $v_0^\infty = 9.89$ mm/s (resp. $v_0^\infty = 13.9$ mm/s) for the intermediate ring, and $v_0^\infty = 11.8$ mm/s (resp. $v_0^\infty = 11.6$ mm/s) for the bigger ring. The fitting parameters Me^* are given in table 4.2. Thanks to these graphs, one can suspect that this lowering in the speed of a walker of diameter $2r_d = 0.7$ mm may come from the confinement of the droplet. However, it is still not clear why we observed this behaviour for the smallest walkers only.

4.2.2.4 Towards others 1d cavities

The results obtained within a 1d linear channel of $D = 1.5\lambda_F$ are illustrated in 4.6. In this experiment, we only work with tiny droplets since we assume the large ones will know a rise of v_0^∞ as expected. The speed of the walker in this linear channel, in the high

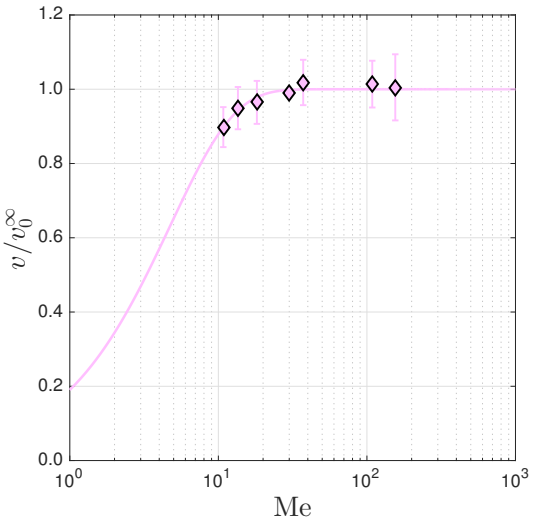

FIGURE 4.6: A semilogarithmic plot showing the evolution of v/v_0^∞ with the memory parameter Me, within a 1d linear channel of width $D/\lambda_F = 3/2$. The droplets diameter is $2r_d = 0.7$ mm. The curve is a fit using using equation 4.1, where the fitting parameter is $\mathrm{Me}^* = 4.7$.

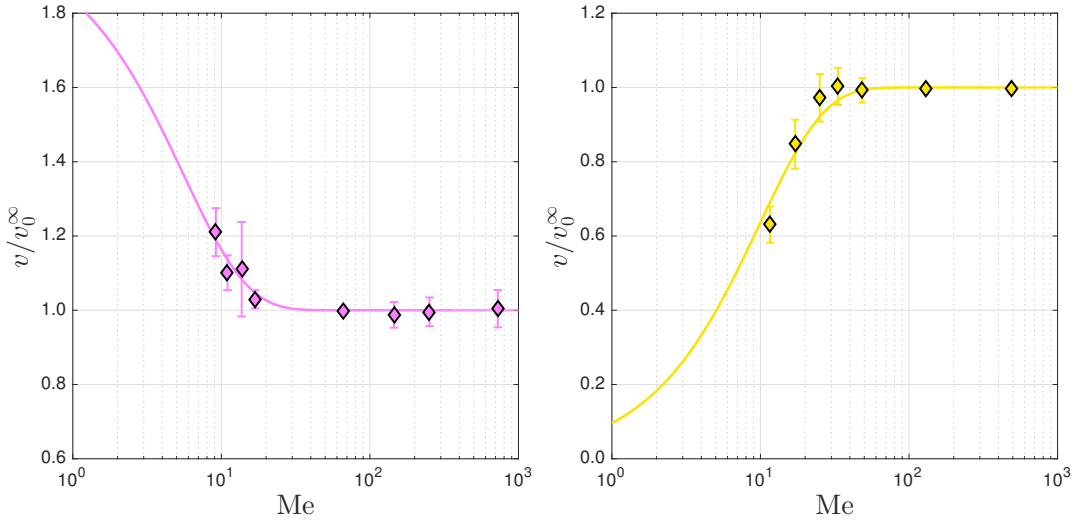

FIGURE 4.7: A semilogarithmic plot showing the evolution of v/v_0^∞ with the memory parameter Me, within a ring of width $D/\lambda_F = 3/2$ and of radius $2R_{\mathrm{small}} = 27.5$ mm. This width corresponds to a 1d guide for the drop, as it was demonstrated in Chapter 3. The droplets diameter is $2r_d = 0.7$ mm (left) and $2r_d = 0.9$ mm (right). The curve on the left figure is a fit using equation 4.2, while the fit used on the right figure follows equation 4.1 One surprisingly observes the decrease in the speed of tiny walkers with Me.

memory regime is $v_0^\infty = 5.4$ mm/s. The behaviour displayed by a tiny droplet within a 1d channel finally follows the assumptions one can have, accordingly to literature about walking droplets, and faults our expectations about confinement. How can we explain the lowering of v_0^∞ in Figure 4.4 ? We expected another decrease in the walker speed

within a linear 1d channel but it yielded to the opposite. Is this striking behaviour due to the confinement and also to the geometry of the circular cavity, where a wavefield could self interfere at high memory? We finally use another cavity: it is still a 1d ring, but of radius $2R_{\text{small}}$. The results are presented in Figure 4.7. For large drops, one has $v_0^\infty = 11.0$ mm/s, and $v_0^\infty = 6.0$ mm/s for the smallest ones. The biggest walkers still follow the same trend and obey the empirical law defined by equation 4.1, while the tiniest droplets know a diminution of the speed with Me, and follow the empirical equation 4.2. The parameters Me* are listed in table 4.2. In the coming section, we discuss and sum up all the results obtained.

4.2.2.5 Discussion

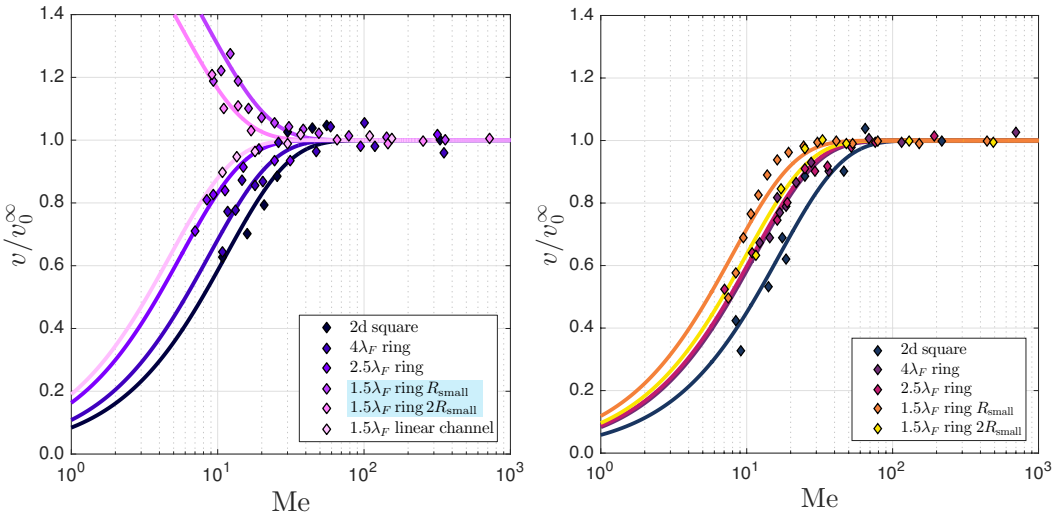

FIGURE 4.8: A summary of every experiments presented above related to the effects of the memory parameters, in the different cavities. The droplets diameter is $2r_d = 0.7$ mm (left) and $2r_d = 0.9$ mm (right). The curves are fits using empirical laws. The error bars of the data plots have been removed for a better understanding and readability.

Cavity	Tiny droplets: v_0^∞ (mm/s)	Large droplets: v_0^∞ (mm/s)
2d cavity	11.6 ± 0.2	14.4 ± 2.3
$4\lambda_F$ ring	11.8 ± 1.0	11.6 ± 0.7
$2.5\lambda_F$ ring	9.89 ± 0.03	13.9 ± 0.7
$1.5\lambda_F$ ring $1R_{\text{small}}$	6.6 ± 0.9	14.3 ± 1.0
$1.5\lambda_F$ ring $2R_{\text{small}}$	6.0 ± 0.5	11.0 ± 0.4
$1.5\lambda_F$ linear channel	5.4 ± 0.6	

TABLE 4.1: Averaged speed v_0^∞, expressed in mm/s, of walkers at the largest memory parameter Me obtained within the different cavities, for small (resp. large) walkers of diameter $2r_d = 0.7$ mm (resp. $2r_d = 0.9$ mm). The cyan coloured cells evidence both sets of data points that follow equation 4.2.

Cavity	Tiny droplets: Me*	Large droplets: Me*
2d cavity	11.4	16.7
$4\lambda_F$ ring	8.7	11.3
$2.5\lambda_F$ ring	5.6	11.0
$1.5\lambda_F$ ring $1R_{\text{small}}$	8.4	7.9
$1.5\lambda_F$ ring $2R_{\text{small}}$	5.5	9.9
$1.5\lambda_F$ linear channel	4.7	

TABLE 4.2: Fitting parameters used in our empirical laws within the different cavities, for small (resp. large) walkers of diameter $2r_d = 0.7$ mm (resp. $2r_d = 0.9$ mm). The cyan coloured cells evidence both sets of data points that follow equation 4.2.

In Figure 4.8, all the results are gathered in order to show the effects of the memory parameter in the different cavities we used. For the sake of clarity and ease of comprehension, the error bars have been removed from this figure. The figure on the left (resp. right) corresponds to the experiments involving small (resp. large) walkers. The v_0^∞ corresponding to each plots are written in table 4.1, and the fitting parameters Me* are given in table 4.2. About the large walkers, one can see that they all face a strong increase of speed with Me. This is the typical behaviour expected [44, 89, 106]. However, concerning the tiny walkers, in every 2d situations the speed grows with the memory as expected. A 1d linear channel leads as well to the same behaviour. Each curve is fitted thanks to the empirical law defined by equation 4.1. However, when working with a 1d annular cavity, one observes the decrease of v/v_0^∞ and the curves are fitted, thanks to equation 4.2. So far, this awkward trend remains unexplained. The only difference with the linear channel is that, within an annular cavity, when the memory is large enough, the present wavefield may interact with its own past, without reflection. One could suspect destructive interferences between the present and the past wavefield. But why does this only occurs for tiny drops ? So far, there is one point we did not mention: the bouncing mode of the droplet. The phase diagram in Figure 4.9 depicts the different kinds of bouncing modes for a fixed frequency of $f = 80$ Hz, as we have seen in Chapter 2. Although we are running our experiments at $f = 70$ Hz, one can make the following assumption. Large walkers speed grows with the memory parameter as one can expect. However, when observing the W region in Figure 4.9, one notes that it is surrounded by two chaotic regions. For small walkers, one may suspect that the droplet size we worked with is just at the boundary between both « Chaos-W » regions. It may explain why we measured a decrease of the speed. However, another element needs to be specified: the Faraday thresholds of the different 1d cavities. In the annular cavity of radius R_{small}, the Faraday threshold is $\Gamma_F = 3.88$, and the forcing acceleration is varied over a range $\Gamma \in [3.38, 3.88]$. One should expect a difference between the thresholds of the annular cavity of radius $2R_{\text{small}}$ and the linear channel

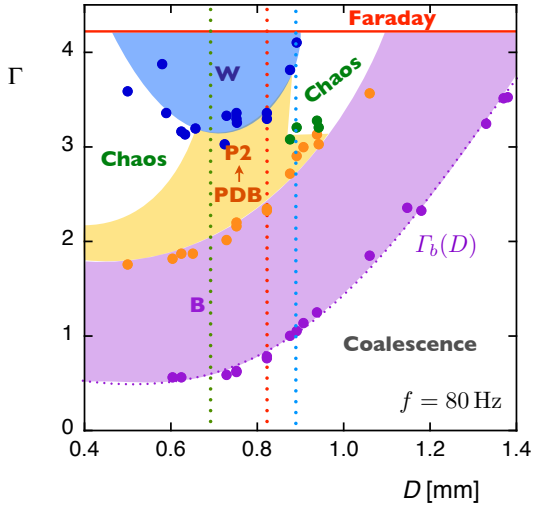

FIGURE 4.9: Phase diagram (Γ, D) of a droplet of 20 cSt silicone oil. The forcing frequency is fixed at $f = 80$ Hz (from [104]).

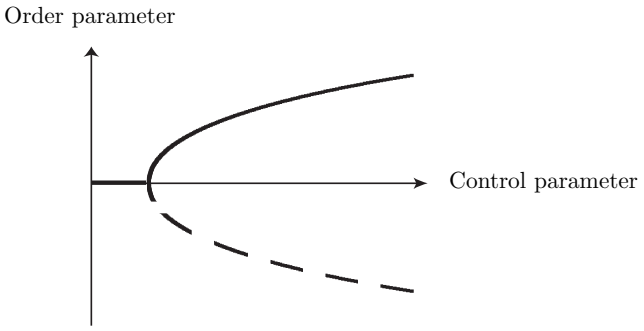

FIGURE 4.10: Schematic of a supercritical pitchfork bifurcation. While the order parameter remains the same below a certain threshold, it suddenly arises after the latter. No hysteresis is observed.

of the same width, since in the first case v/v_0^∞ arises with the memory parameter, contrary to the linear channel. Nevertheless, both Faraday thresholds were the same: $\Gamma_F = 3.63$, and the walkers were evolving in the domain $\Gamma \in [3.38, 3.63]$. For the three 1d cavities, the same range of Γ were finally explored. Another path certainly needs to be explored: it is the bifurcation branch. In Figure 4.10, a supercritical pitchfork bifurcation is illustrated. Maybe in the case of tiny walkers in circular 1d cavities, the lower branch of the bifurcation diagram is the solution of the system, for a reason that remains obscure. This is maybe why the walkers, in these conditions, know a decrease in their speed.

We have finally pointed out a striking phenomenon. In specific conditions, the speed of a walker can decrease with the memory parameter. We only have assumptions to

attempt to explain this trend. Even though this diminishing remains unsolved, we have opened a door for a new problem and we are still seeking a solution.

4.3 Submarine barriers

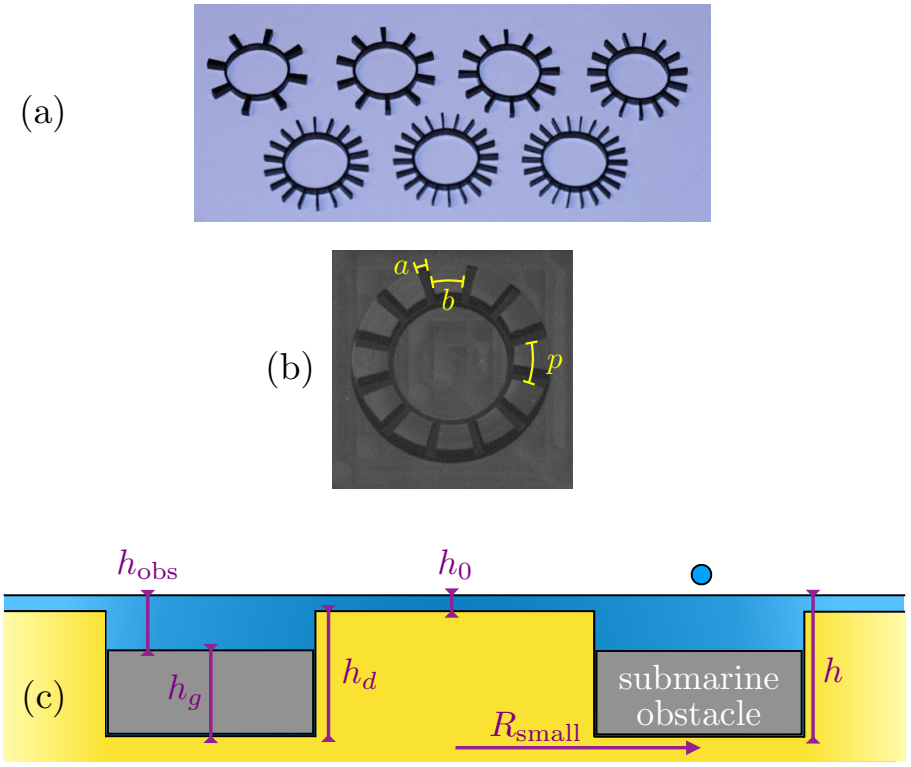

FIGURE 4.11: (a) Photograph of a part of the different gears used in our experiments, with a number of teeth N_t ranging from 8 to 22. (b) Photograph of a gear with $N_t = 12$ that fits in a ring. The thickness of a tooth is noted a, and the gap between two consecutive teeth is b. The pitch of this network is given by $p = a + b$. It seems that a and b vary on the photograph. This impression is actually only due to the shadows of some tooth, because of a little tilting of the camera, and the light above the bath, whose beams are not perfectly perpendicular to the experimental setup. (c) A schematic cross-section of the annular cavity of different depths, to host our different gears. The depth h_d is fixed to 4.5 mm. The submarine obstacle is sketched within the 1d cavity, of radius R_{small}. The thin layer of silicone oil, in the surrounding shallow water area is noted h_0, and h corresponds to the deep water area. The height of the gear is given by $h_g = 3$ mm, and the layer of oil above is noted h_{obs}. A tiny walker of diameter $2r_d = 0.7$ mm is represented near the bath.

In this section, we emphasise the effects of periodic submarine barriers submerged in a circular 1d cavity, on the dynamics of walkers. The droplets have a diameter of $2r_d = 0.700$ mm, the memory parameter is fixed at $\text{Me} = 20$ and we work with an annular cavity of radius R_{small} but with a different channel depth $h_d = h - h_0$, which was fixed at $h_d = 3$ mm in the previously presented results. This study is an extended work to the tunneling effect, which was already investigated and characterised [118, 137].

Our idea is to go further: instead of a step of a certain thickness and height, and a droplet evolving in a 2d area, we use a submarine lattice, placed within our 1d ring. For this effect, we have built several gear-like pieces, see Figure 4.11(a). We used gears with a number of teeth of $N_t = [8, 10, 12, 15, 18, 20, 22, 26, 28, 30, 32]$. The thickness of a tooth is noted a, and the gap between two consecutive teeth written b. They vary with N_t, as one can observe in Figures 4.11(a) and 4.11(b). The pitch of this submarine network is given by $p = a + b$. Note that, for every gear, the surface S_{obs} corresponds to the obstacles. In other words it corresponds to the shallow water region explored by the walkers, and it remains roughly the same from one gear to another. It is calculated by $aN_t l_t = S_{\text{obs}}$, where $l_t = 6.2$ mm is the length of a tooth. The height of the gears is $h_g = 3$ mm. The parameters a, b and p are given in table 4.3. In the following, we will work with the adimensionalised quantity p/λ_F, also given in table 4.3, with a precision of 3%. The Faraday wavelength is given by $\lambda_F = 6.1$ mm, its determination is explained in Chapter 5. In order to receive these gears, the annular channel was dug until reaching $h_d = 4.5$ mm, see Figure 4.11(c). One fixes the parameters h and h_0 so that the walker feels the depth variation. The liquid height above an obstacle, *i.e.* above a tooth, noted h_{obs} must correspond to a shallow water region that a walker may cross.

N_t	a (mm)	b (mm)	p (mm)	p/λ_F
8	2.05	8.35	10.4	1.71
10	1.6	6.75	8.35	1.37
12	1.3	5.5	6.8	1.11
15	1.05	4.45	5.5	0.90
18	0.9	4.0	4.9	0.80
20	0.8	3.3	4.1	0.67
22	0.6	3.2	3.8	0.62
26	0.74	2.75	3.49	0.57
28	0.64	2.53	3.17	0.52
30	0.62	2.36	2.93	0.48
32	0.55	2.27	2.82	0.46

TABLE 4.3: The various parameters of the gears we used in our experiments: number of teeth N_t, width of a tooth a, gap between two successive teeth b, pitch of the network p.

In solid state physics, for physical systems below a certain size, as a wavelength for example, surprising phenomena different from the large scales may occur. Immediate examples deal with light diffraction, X-ray crystallography. In the present experiment, we focus on the mean speed of the walker as a function of p/λ_F. Our setup can be seen as a Kronig-Penney experiment [145–148] but adapted for walkers that cross a periodic potential well. Indeed, Kronig-Penney model is represented by a 1d periodic potentiel,

as it is the case for our 1d annular cavity. The periodicity of the potential well is a relevant property that yields electronic band structure. Solving the Schrödinger equation provides the allowed and forbidden energies. We wonder if, with this experiment, we can similarly obtain band gaps.

A first attempt was made, by fixing $h_0 = 1$ mm and $h_{\text{obs}} = 2.5$ mm. However, the mean speed of a walker remained constant for the different gears and its speed was identical as a walker in a bare ring. This could be expected because the Faraday threshold was not modified in the presence of gears. In addition, when referring to Figure 3.9, one can observes that below $h \simeq 2$ mm, the bouncing mode of a walker remains unaffected. Besides, the thickness of the teeth is too thin for the walker to feel their influence. Consequently, one ensures that h_{obs} in our setup, is calibrated so that it is below 2 mm. In the following, we carefully fixed the liquid heights to: $h = 4.9$ mm and $h_0 = 0.4$ mm. It yields to $h_{\text{obs}} = 1.9$ mm. The speed v_0 of a walker in the bare ring is $v_0 = 7.5$ mm/s. In Figure 4.12(a), the adimensionalised mean speed of a walker v/v_0 is plotted as a function of p/λ_F. Each ratio v/v_0 is lower than 1, accordingly to our expectations. The walker in these experimental conditions, feels the presence of the submarine obstacles. The mean speed of a walker decreases slowly until reaching $p/\lambda_F \simeq 1/2$, where it dramatically collapses near zero. Then, one notes a quick boost in the ratio v/v_0 which roughly reaches $v/v_0 \simeq 0.8$. Different regions are depicted on this figure: two green ones and a blue ones. In the blue region, the walker encounters a change, or several, of its direction of rotation, whereas in the green region, the walker is not subject to any change. Note that the green area on the left is presented with a colour gradient, revealing the absence of data points for $p/\lambda_F < 0.5$. In the Kronig-Penney model, one determines several energy bands. One may suspect to obtain several other blue bands, where the mean speed collapses again as a result of regular changes of direction. In Figure 4.12(b), the angular positions of a walker are illustrated, in both different regions. Figure 4.12(b) on the left depicts a trajectory of a walker with numerous changes of its direction of rotation, which significantly lower its mean speed, whereas, as it is illustrated on the figure 4.12(b) on the right, the walker constantly orbits clockwise. In Figure 4.12(c), one focuses on the evolution of the adimensionalised Faraday threshold Γ_0/Γ_F^0 as a function of p/λ_F, where Γ_F^0 is the Faraday threshold of the bare cavity. When looking at the ratios, it appears that the presence of gears has a very little influence over the Faraday threshold of the bare ring. However, the gap between Γ_F/Γ_F^0 is sufficient enough for the walker to feel the influence of the gears. Note that in the blue region, Γ_F increases significantly before it collapses and starts soaring again.

This original experiment finally reveals that the presence of a periodic submarine lattice modifies the dynamics of a walker. The green regions depicted in Figures 4.12(a) and 4.12(c) can be seen as « allowed » regions for the walker, which only faces a variation of its speed, depending on the adimensionalised pitch of the lattice. However, when a walker explores a blue region, it is subjected to numerous changes in its direction of rotation, which leads to a dramatic decrease of its mean speed, which is close to zero. One can consider this region as a forbidden band, for a walker, similarly as the Kronig-Penney model that evidences forbidden bands for the electrons. One suspects that when reaching $p/\lambda_F = 1/2$, the Faraday wavelength is locked on the pitch of the lattice, which implies a collapse of the velocity of the walker. One finally wonders if there are there others blue regions when decreasing p/λ_F. It would clearly be of interest to explore this unknown area, as well as studying the effects of the memory parameter, the droplet size and the liquid height above the obstacle h_{obs}. This study opens therefore new types of original investigations.

4.4 Conclusion

In this chapter, we introduced our first experiments involving an annular cavity. Its width was chosen so that a walker remained confined within, and we demonstrated that the walker was properly trapped in the ring. Whatever the radius of the ring is, the droplet follows a regular circular path. The patterns of the Faraday instability has been characterised and we evidenced that the evanescent waves are quickly damped outside the ring, similarly to our previous linear channels.

Secondly, we focused on the effects of the memory parameter on the droplet speed. We demonstrated that depending on the size of the droplet and the geometry of the cavity, unexpected behaviours occurred but only for the tiny walkers. In particular, we observed that, in annular cavities, a walker of diameter $2r_d = 0.7$ mm was subject to a lowering of its velocity with Me, contrary to our expectations from literature, which announces the opposite, because of the subcritical bifurcation that a walker undergoes. This striking result is maybe related to the bouncing mode of the tiny walker, which could be in between a chaotic and a walking regime. This is a pure assumption. Another explanation is that, it could be the manifestation of a walker verifying the lower branch of the supercritical bifurcation.

Finally, we extended our investigations to an annular cavity with submarine obstacles. This is a sort of extension to prior works on tunnelling effects. We propose to design some periodic obstacles that the walker has to cross. This experiment is a sort of

adaptation for walkers of the Kronig-Penney model. The study of the mean speed of walkers v/v_0 as a function of p/λ_F provides the existence of a forbidden band, where a walker can hardly explore the whole annular cavity, due to multiple changes of its direction of rotation that result in a speed close to zero. It would be worth exploring the region below $p/\lambda_F < 0.5$ to possibly discover new forbidden bands for walkers. Since we observed a dramatic decrease in the speed of a walker at $p/\lambda_F = 1/2$, one may suspect a similar behaviour for $p/\lambda_F = 1$. Additional data points should be taken close to this ratio and it would be worthy building with an intermediate number of teeth $N_t = 13$ to 14. It would be of interest to work with larger teeth widths, and to study the effects of h_{obs} or Me. Another interesting key parameter to study would be the Faraday threshold depending on the lattice used. Designing a gear accordingly to a dramatic enhancement of the Faraday threshold, but for which a walker can cross the various obstacles, would probably lead to some other surprising and interesting discoveries.

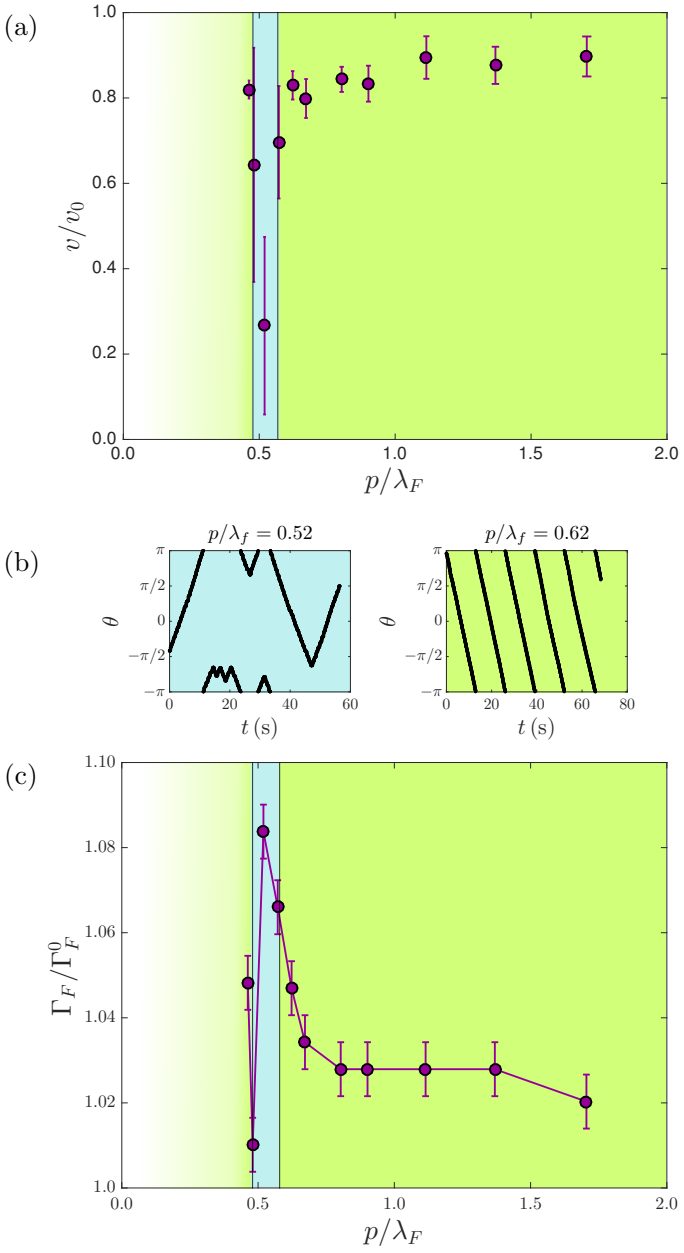

FIGURE 4.12: (a) Evolution of the adimensionalised mean speed of a walker v/v_0 in a cavity with periodic submarine obstacles, as function of the adimensionalised pitch of the network p/λ_F. The ratio v/v_0 is always lower than 1. Regions of different colours are depicted. The green area on the right corresponds to a walker which permanently orbits in the same direction. In the blue area, the walkers frequently undergo modifications of their direction of rotation. The green area on the left, however, represents the start of a new region without modification of the direction or rotation. Nevertheless, we prefer to apply a white to green colour gradient, since we have no data point below $p/\lambda_F < 0.5$. (b) Angular position of a walker evolving in a cavity with a periodic submerged potentiel. On the left, we present a walker whose direction of rotation is regularly modified. On the right, a trajectory of a walker that moves clockwise without any change of direction is illustrated. (c) Adimensionalised Faraday thresholds Γ_F/Γ_F^0 for the different gears used, where Γ_F^0 is the threshold of the bare ring. One has $\Gamma_F^0 = 3.92$. The regions depicting the possible variations of the direction of rotation are represented.

Chapter 5

Interactions between droplets

In this chapter, we focus on the interactions between droplets. First, we review the interactions between them among 1d linear channels. We depict a variety of events that can occur when a droplet encounters another one. In a second part, we keep our attention on the interactions between droplets placed in a ring. Surprising results are obtained. In particular, when every walker in a cavity moves clockwise or counter clockwise, we show that the droplets finally share a coherent wave. It results that they are even propelled at a velocity faster than a single walker.

5.1 Interactions within linear channels

5.1.1 Methods

In the following experiments, we work with linear channels and keep the same experimental conditions as in Chapter 3. The results we present are illustrated via spatio-temporal diagrams, see Figures 5.1 to 5.4. The drops are enlightened so that we only visualise them without their wavefields, as it was described in Figure 3.3(a). For each experiment, we shoot the trajectory of the droplets. Afterwards, a Matlab code is run over each frame of the movie. It determines the mean value of the intensity of the pixels over each horizontal line, which provides a resulting frame of width one pixel. Thus, one easily gets the vertical position of the droplets within the channel. Finally, every resulting frames are combined to build a spatio-temporal diagram. On each diagram, the upwards and downwards borders of the cavities are illustrated thanks to yellow dashed lines. The frames of the examined movie corresponding to the initial and final times, noted t_0 and t_f, are placed on both sides of the resulting diagram. The position

of the walkers is indicated with yellow circles. Just below an axis corresponding to the elapsed time is placed. When needed, the instants we want to focus on are indicated with their corresponding frame or a coloured square. In the coming section, we emphasise the variety of behaviours between interacting droplets.

5.1.2 Towards repulsion, merging, orbits and vanishing

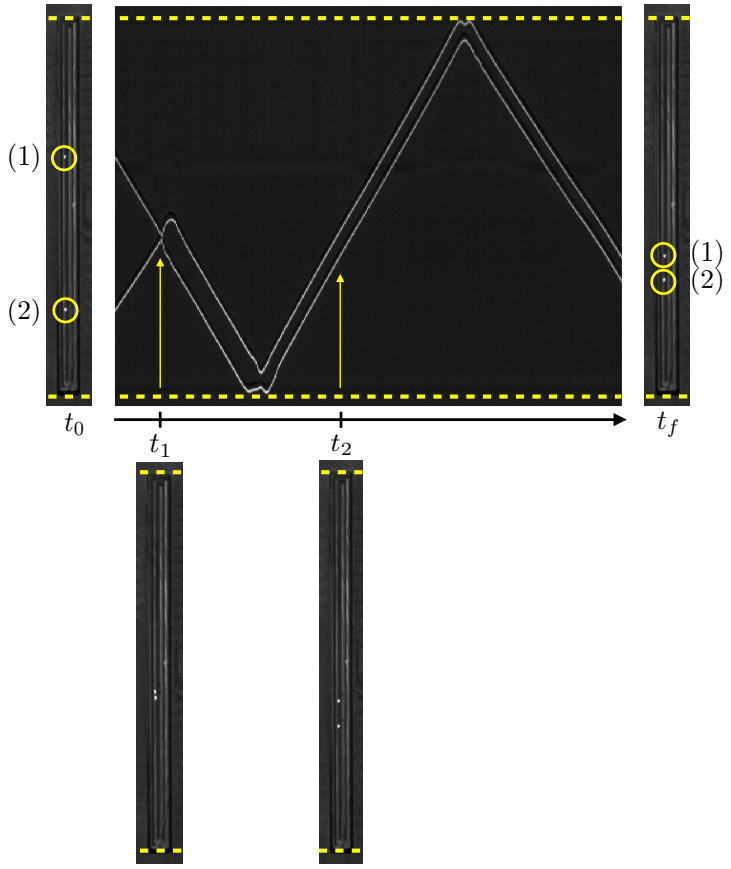

FIGURE 5.1: Spatio-temporal diagram of two droplets placed within a linear channel of width $1.5\,\lambda_F$. The yellow dot lines delimit the borders of the rectangular channel. A black arrow line shows the elapsed time. The spatio-temporal diagram is surrounded by two photographs, at the initial and final times t_0 and t_f. Two yellow circles show the positions of both droplets. Two yellow arrow lines illustrate two phenomena at the times t_1 and t_2, which are depicted with two photographs below the spatio-temporal diagram. The time t_1 reveals a collision between both droplets, which do not merge here, but currently move at the same fixed distance before they collide with the downwards border. At the time t_2, one can observe the droplets moving with another fixed distance.

When several droplets are placed within a cavity, they interact with each other. A variety of different events can happen. In Figure 5.1, is illustrated a collision between two walkers, which are currently repelled. They were both created within a linear channel of width $1.5\,\lambda_F$, the memory parameter is fixed at $\mathrm{Me} = 20$. At the initial state,

one can observe that the droplets are getting closer. Then, a collision between them occurs at the instant t_1 and is illustrated by a photograph underneath. Afterwards, walker 1 goes backwards for a few seconds before it turns back, once more, to follow the other drop at a fixed distance. Then, droplet 2 interacts with the lower border of the channel. At the instant t_2, the pair of walkers goes backwards at the same speed but with a different fixed distance. Finally, droplet 1 interacts with the upwards extremity of the channel and the pair of walkers go backwards again, and so on. Note that, in this figure, when walker 2 interacts with the edge of the cavity, it remains there for a few seconds before it is repelled and moves along with walker 1. In Figure 5.2,

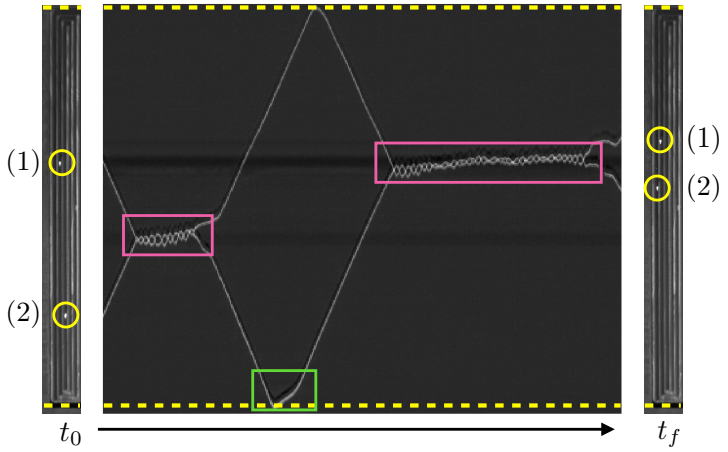

FIGURE 5.2: Spatio-temporal diagram of two droplets placed within a linear channel of width $2\,\lambda_F$. The yellow dot lines delimit the borders of the channel. A black arrow line shows the elapsed time. The spatio-temporal diagram is surrounded by two photographs, at the initial and final times t_0 and t_f. Two yellow circles show the positions of both droplets. This diagram shows that when both droplets orbit each other for a dozen of seconds or so, after they repel and move in opposite directions, as it is illustrated with both pink rectangles. In both cases, the droplets finally repel. The green square shows an interaction with droplet 2, which remains close to the downwards border for a few seconds, before it goes backward.

both pink squares depict a phenomenon that does not frequently happen between two walkers within a channel. Both droplets orbit and follow a twin star type of motion which is not stationary. It usually ends in the repellence of the walkers in opposite directions, after one tenth of a second. This orbiting phenomenon is even more striking and shows some limit of our quasi 1d channels. A single droplet follows a 1d path in such channel. However, two walkers when they might orbit, describe a 2d motion. In particular, the distance between both « twin stars » droplets is always below half of the Faraday wavelength, in our observations. Thus, there is always enough room in our 1d channels, so that both droplets can orbit. Another limitation to our 1d channel is that, when two walkers are orbiting, they might escape from the cavity. This rare event is only possible because the wavefield resulting from the interaction between

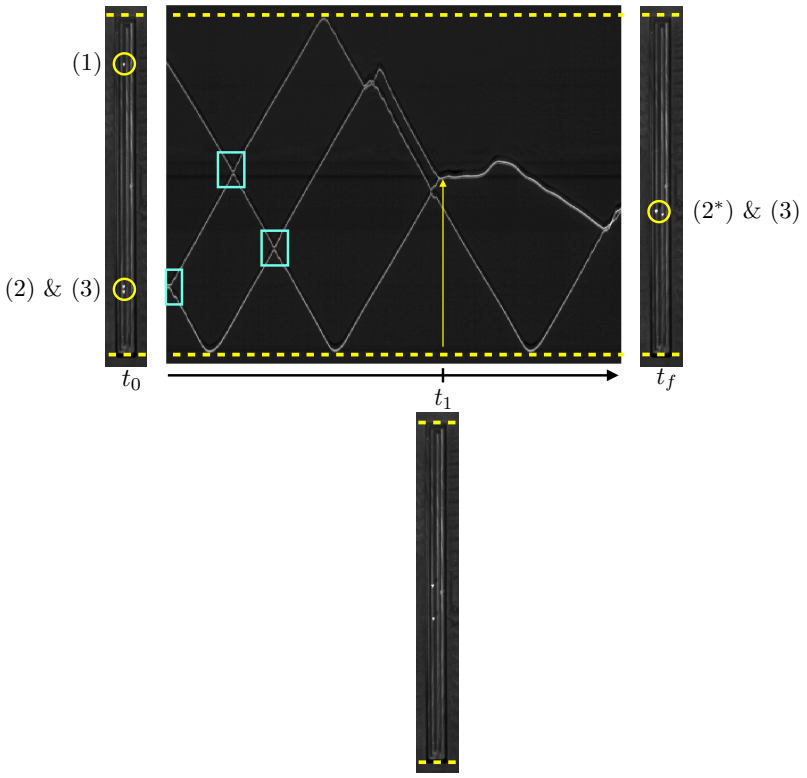

FIGURE 5.3: Spatio-temporal diagram of three droplets placed within a linear channel of width $1.5\,\lambda_F$. The yellow dot lines delimit the borders of the channel. A black arrow line shows the elapsed time. The spatio-temporal diagram is surrounded by two photographs, at the initial and final times t_0 and t_f. Yellow circles show the positions of the droplets. Blue squares reveal the collisions undergone by two droplets, which quasi-instantly repel and move in opposite directions. At the instant t_1, a particular phenomenon is observed. The drops numbered 1 and 2 finally merge and form a larger droplet numbered 2^*. Note that, droplet 3 is not responsible for this merging. Two droplets can easily gather in a larger one as soon as they are moving toward each other.

two walkers is no longer damped enough in the shallow water area. Thus, one of the orbiting droplet can visit a small part of the shallow water area, before it is attracted again into the channel thanks to its neighbour droplet. In an even more rare case both droplets might escape from the channel. They end up deriving and remaining bouncing droplets in the shallow water region. Another event in the green square is illustrated. One can see a small wobbling motion, nearby the extremity of the linear channel. The spatio-temporal diagram also reveals that when interacting with the edge of the channel, the conservation of momentum is faulted. In Figure 5.3, one can focus on another event: a merging. In this experiment, three walkers were placed within a 1d channel. In the beginning of the figure, three blue squares are showing the collisions between the droplets, which result quasi-immediately in the repellence between the interacting droplets. At a time t_1, the merging of both droplets 1 and 2 occurs, which gives a droplet named 2^*. In the end of the spatio-temporal diagram, one observes

that there are only two gray lines of different widths, illustrating the trajectory of both walkers. The thickest line corresponds to the large droplet 2* and the thinnest to walker 3. Finally, in Figure 5.4 another phenomenon is evidenced: the vanishing of a droplet.

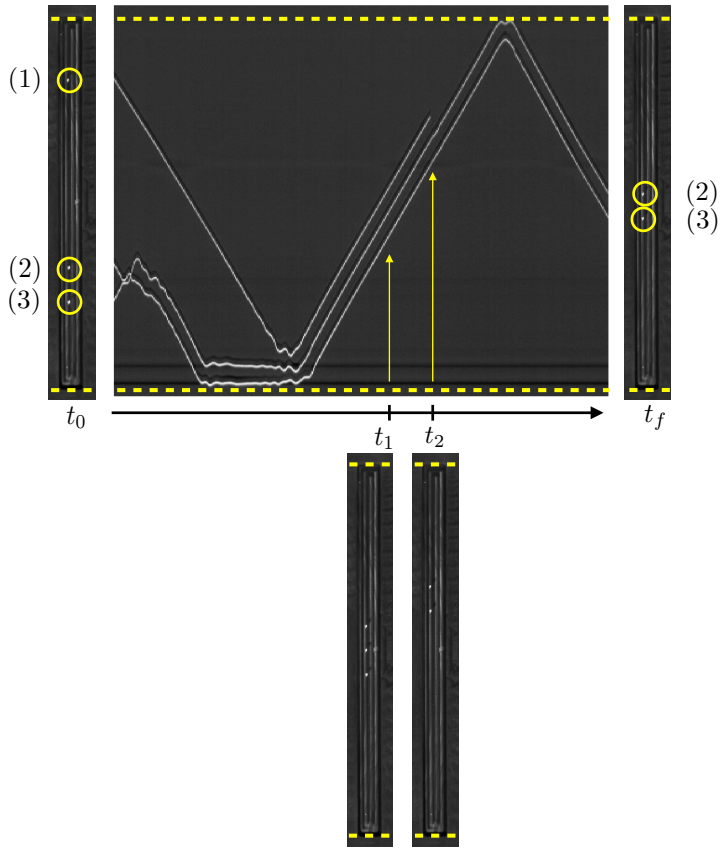

FIGURE 5.4: Spatio-temporal diagram of three droplets placed within a linear channel of width $1.5\,\lambda_F$. The yellow dot lines delimit the borders of the channel. A black arrow line shows the elapsed time. The spatio-temporal diagram is surrounded by two photographs, at the initial and final times t_0 and t_f. Yellow circles show the positions of the droplets. One can observe that droplet 2 and droplet 3 move roughly at a fixed distance, before they interact with the downwards border of the channel and stays there for a few seconds. Afterwards, walker 1 interacts with the pair of walkers and is repelled. Thereafter, it results in a string of three walkers, moving at the same speed with the same fixed distance between each consecutive walker, as it is illustrated at the time t_1. At the time t_2, one can see that the droplet 1 has coalesced. Droplets 2 and 3 eventually continue their trajectory, still at the same speed.

Three walkers were created within a linear cavity of width $1.5\,\lambda_F$. In the first half of the phase diagram, one observes the interaction between the lower walkers with the edge of the cavity. Similarly to Figure 5.1 where a walker seemed to get trapped close to the edge, both walkers are trapped and stay close to the edge for a few seconds, before being finally repelled and moving all together with the third walker. In the second half of the space time diagram, one eventually has a chain of three droplets which are moving at a fixed and identical distance. In particular, this is illustrated at

the instant t_1. Then, at an instant t_2 is depicted the vanishing of a droplet, probably due to some dust particules lying on the bath surface. However, it is interesting to see that the coalescence of a droplet does not disturb the path, or the speed, of its neighbours. Indeed, both surviving droplets keep going at the same speed. This will be further discussed in section 5.2.

5.1.3 Discussion: from channels to rings

We have previously discussed the different phenomena that can arise, when placing several droplets within a linear cavity. One has depicted merging, repulsions, orbits, and the vanishing of droplets, from Figures 5.1-5.4. The orbiting events have pointed out some limit to our 1d channels, since they can undergo a 2d path. It has also been showed that, when several droplets are moving together as a « string », when they interact with an edge of the cavity they may be stuck for a few seconds and the distance between them may vary. Actually, this situation was regularly encountered. It may even result in the splitting of a chain, when considering a chain of more than two walkers which were interacting close to the border of the cavity. For these different reasons, it is finally difficult to characterise the interactions between numerous droplets, even if we easily evidence the different phenomena with several droplets. In addition, the chances for two droplets to merge are not negligible. The experiments we performed usually lasted a few minutes before two walkers, or even more, merged. The main drawback of this experimental setup is currently the extremities of the channel. The latter are responsible for the collisions between droplets, when they have to go backward, which often lead to the merging of both droplets or the splitting of a chain of droplets. A simple way to avoid that is to work with an annular cavity. In particular, in Chapter 3, we studied annular cavity wherein a walker was following a 1d motion along a circular line. This robust method will enable us to study the interaction between numerous droplets and to reveal the coherent nature of the wavefield.

5.2 One ring to rule them all

Walking droplets possess fascinating properties due to their peculiar wave-particle interaction leading to unexpected quantum-like behaviours. We propose an original study consisting in droplets walking along annular cavities. We show that, in this geometry, they spontaneously form a string of synchronised bouncing droplets that share a common coherent wave propelling the group at a speed faster than single walkers. The

formation of this coherent wave and the collective droplet behaviours are captured by a model. Those are at the opposite of the ones found in 2d geometries [129]. Our results shed a new light on walking dynamics.

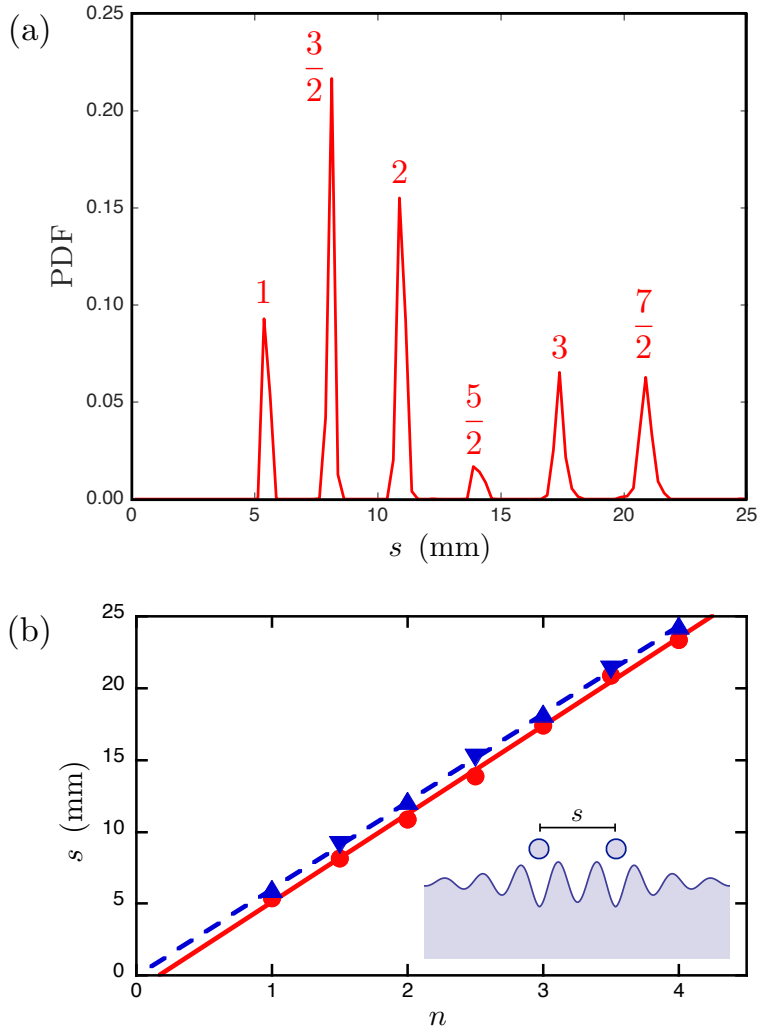

FIGURE 5.5: (a) PDF of the distance between two identical walkers, at a memory Me = 20. Around 15000 events were measured. The values $1, 3/2, 2, 5/2, \ldots$ correspond to the discrete sets of n according to equation 5.1. (b) Red dots represent the droplet interdistances as a function of the label n describing the interaction mode for a memory Me = 20. These data points are provided by the PDF diagram above. The red line is a fit using equation(5.1). Error bars are not indicated since they are smaller than the symbol size. Blue triangles are droplet interdistances given by the model for synchronous (triangle up) or antisynchronous bounces (triangle down). In the synchronous bounces both droplets are successively lifting and landing at the same time. In the antisynchronous case, while a first drop bounces, the second one is in a free flight and vice versa. The dashed blue line is a fit upon simply assuming s as submultiples of the Faraday wavelength: $s \simeq n\lambda_F/2$. Note that the quantification does not depend on the value of the memory Me.

5.2.1 Interaction between two droplets

In this section, we work with the same experimental parameters previously described in Chapter 4. We consider circular rings of radius $R_{\text{small}} = 13.75$ mm, where droplets walk forever without reaching a boundary. The sketch of an annular cavity was given in Figure 4.1(a). All the experiments involve droplets of diameter $2r_d = 0.8$ mm. When two (or more) droplets are placed in the ring, they walk clockwise or counterclockwise depending on their initial conditions. We focus here on the interactions between only two identical droplets, which walk in the same direction. When both droplets walk in the opposition direction, one encounters the same behaviours, depicted in section 5.1. To avoid such thing, we proceed as follows: a first droplet is created above the cavity. Secondly, another walker is created nearby the ring. Therefore, it simply consists in

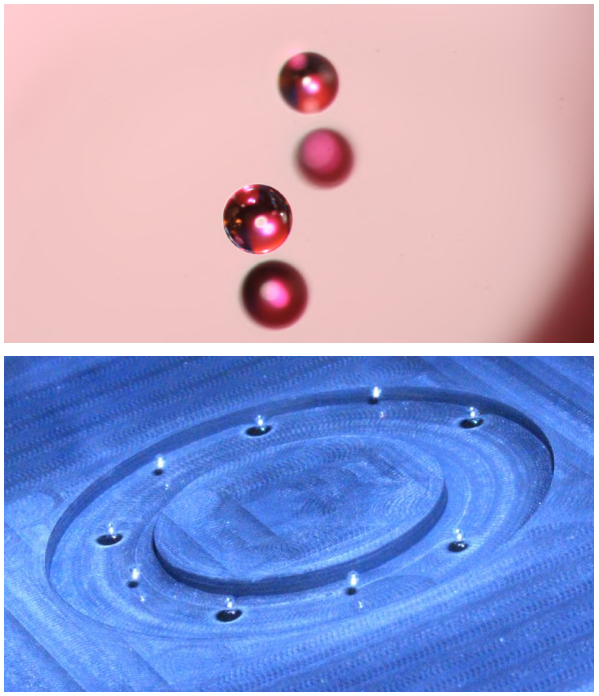

FIGURE 5.6: (a) Photograph of two walkers in a synchronous bounce. (b) Photograph of a group of 9 walkers in an annular cavity. One observes quantified interdistances ($s \simeq 3/2\lambda_F$) and antisynchronous bounces for the successive droplets. Note that the case of a string of N walkers (where $N > 2$) will be examine in subsection 5.2.2.

bending the surface of the liquid with a needle tip in order to propel the second walker in the same direction of the first one. After a while, both walkers interact through their waves and come to bounce at a fixed distance from each other, as it was already demonstrated by the group of Couder [83, 111, 129]. In Figure 5.5(a), a PDF diagram demonstrates that these quantified distances noted s, are stable in time. This figure was obtained upon simply recording the trajectory of a pair of orbiting walkers, in a steady state. The distance s was then calculated. We repeated the experiment

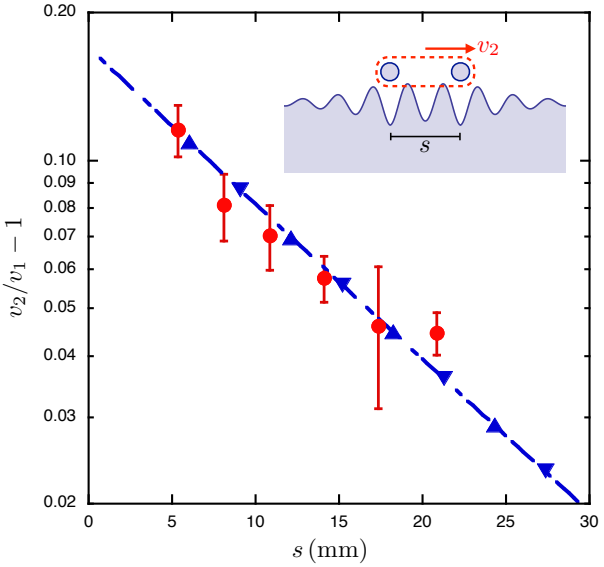

FIGURE 5.7: (Circles) Speed of a droplet pair v_2 (in log. scale) as a function of the distance s between droplets. The speed is normalised by the speed v_1 of a single droplet. Error bars are indicated. (Triangles) The model explained in the main text returns quantified interdistances s between droplets as well as specific speeds v_2 for both synchronous (triangle up) and antisynchronous (triangle down) cases. An excellent agreement is found between the model and the experimental data. The dashed curve is an exponential decay fitting the results from the model.

for numerous pairs, at different fixed distances. We obtained around 15000 events to build this PDF. The obtained peaks clearly reveal the distance quantification. Thanks to this diagram, one can build Figure 5.5(b) to characterise the quantification of the interdistances between successive droplets, in various groups of two droplets that are launched randomly in an annular cavity. The space s is a set of discrete values linked with the Faraday wavelength λ_F, accordingly to the following empirical formula:

$$s = (n - \epsilon_0)\lambda_F, \tag{5.1}$$

where ϵ_0 accounts for the dimensional aspect of the waves and their damping due to viscosity. The label n is an integer or a half integer. Fit using equation 5.1 gives $\lambda_F = 6.1 \pm 0.1\,\text{mm}$ and $\epsilon_0 = 0.18 \pm 0.02$. The first observed situation corresponds to $n = 1$ for which the bounces are synchronised, see Figure 5.6(a). Half integer values of n correspond to antisynchronised walkers, see Figure 5.6(b). The case $n = 1/2$ is particular since the droplets start to orbit around each other and they follow complex trajectories [111]. They finally coalesce or vanish in the vibrating bath. The absence of circular motions and promenade modes for other interdistances is assumed to be due to the constrain originated from the boundaries. Figure 5.7 shows the speed v_2 of the pair of bouncing droplets as a function of the distance s separating them. The group

speed is normalised by the speed v_1 of single droplets in the ring, where $v_1 \simeq 10$ mm/s. The single droplet case v_1 should represent the asymptotic case when the interdistance tends to infinity to neglect interactions. The speeds v_2 obtained for droplet pairs are larger than v_1 in both synchronous and antisynchronous cases. The speed ratio is also seen to decrease exponentially as a function of s. A model was developed, see the blue dashed line, and is in good agreement with our experiment. The latter is described in subsection 5.2.3. We will also develop there why the pair of walkers is moving faster than a single one. In the following, we discuss the evolution of a string with more than two droplets.

5.2.2 Interaction with N droplets

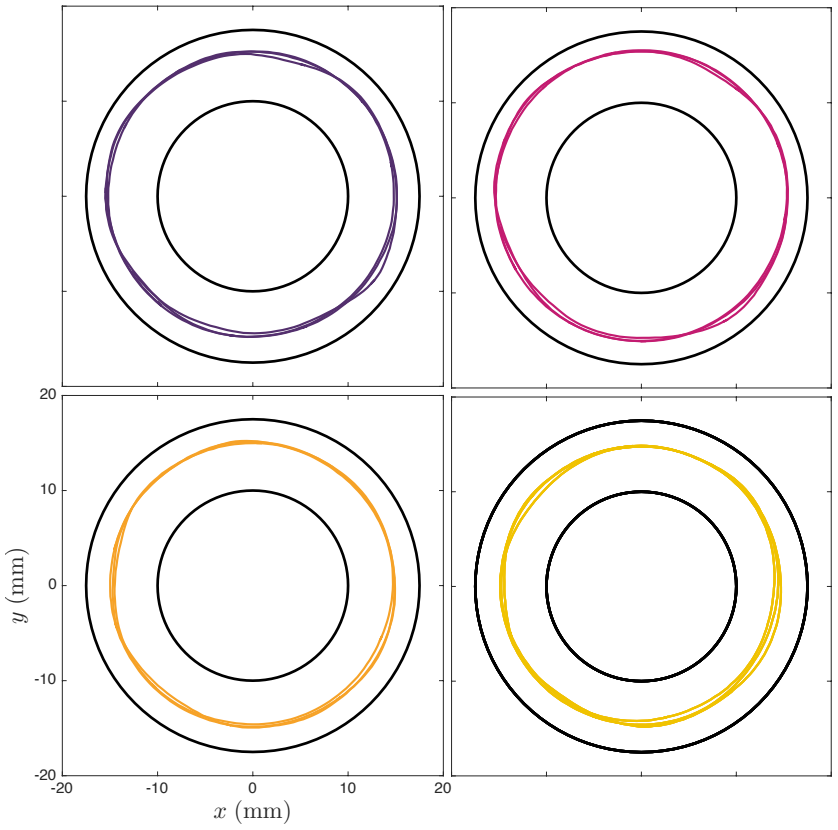

FIGURE 5.8: Trajectory of a string of 4 droplets, distant from $s \simeq 1.5\,\lambda_F$. Each walker still follows a circular 1d trajectory. Each colour corresponds to a walker.

In Figure 5.8, four trajectories of four droplets are presented. The distance between two consecutive walkers is about 1.5 λ_F. It is worth noting that all the walkers that constitute this string still follow regular circular trajectories. All the drops are moving at the same speed, consequently the distance between each drop remains the same, no matter how many droplets the string involves. Figure 5.9 presents a picture of a chain of four droplets. It also offers a visualisation of the wavefield emitted by the drops,

which adapts to the cavity symmetry. The coherence of the wave propelling the string of walkers has been tested [149]. When a string of a few droplets is formed, we used a needle to destroy one of the central droplets. The system appears to be unaffected by the disappearance of this droplet and behaves exactly as before. The distances remain unchanged and the synchronicity is kept. Movies of that experiments are given

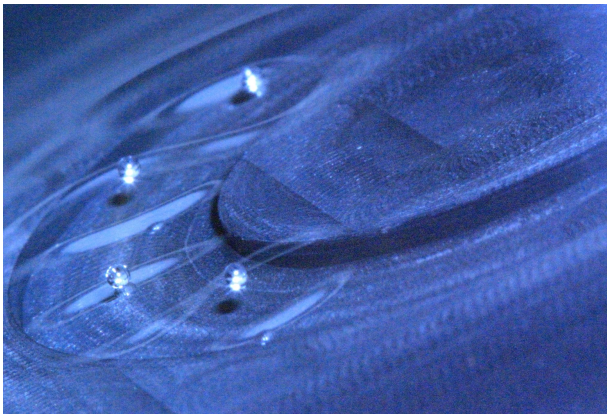

FIGURE 5.9: Four bouncing droplets walking in an annular cavity and creating a coherent wave propelling the group at a speed larger than individual droplets. The coherent wave is seen to follow the cavity symmetry. One can observe anti-synchronous bounces for the successive drops.

in the supplementary materials [149]. Such an experiment, to verify the coherence of the waves, was already presented in Figure 5.4. Indeed the spatio-temporal diagram revealed the vanishing of a droplet did not impact the speed of the remaining walkers. The only difference in Figure 5.4, is that the walker naturally vanished (probably because of some dust particles), without the disturbing action of the experimenter. It clearly confirms that the coherence is not an artefact. When the number N of droplets increases, the coherent wave extension increases accordingly. At some point, the wave starts to self-interfere such that the system destabilises, as it is depicted in Figure 5.10. We checked that it is nearly impossible to form a complete ring of droplets moving cooperatively due to this effect. The only stable groups of droplets are found up to 11 droplets in the smallest ring, each pair of droplets being distant from about one λ_F. In the same spirit, modifying the acceleration will inevitably change the stability of the system. Indeed, at higher memory, *e.g.* $\mathrm{Me} = 45$, only seven droplets can be placed. The space between each consecutive droplets was also varied. At a fixed memory of $\mathrm{Me} = 20$, one could only create a string of eight droplets, separated by $1.5\,\lambda_F$, which, in terms of distance between the head and the tail of the string, corresponds to a length of $d_{ht} \simeq 56$ mm. Note that it also equals the length of a string of 11 walkers, equally spaced by a single wavelength.

The collective motion of the string was unexpected because in 2d only a few cases lead to a rectilinear motion of the center of mass. Indeed, mainly two behaviours are found: promenade modes and orbiting motions. For both dynamics, the collective velocity is lower than the individual droplets freely moving along the surface [111, 129]. So far, with the pairs of walkers, we have demonstrated a clear violation of this conjecture and so, will the strings of N droplets (where $N > 2$). In order to emphasise the collective effects induced by wider coherent waves, we created groups of N droplets being separated by a single wavelength λ_F. All droplets are therefore bouncing in a synchronised way. The normalised speed v_N/v_1 of the string increases with N, as shown in Figure 5.11. The speed of the string seems to saturate for high N values, meaning that there is a limit for coherence. The origin of this limit is due to the damping of Faraday waves. Indeed, above a droplet number (around $N = 6$ in our experimental conditions) any additional droplet joining the string will not affect the global dynamics. We also created strings with a larger separation between successive walkers, like $3\lambda_F/2$. Similar results are obtained but the saturation speed is lower than the previous case.

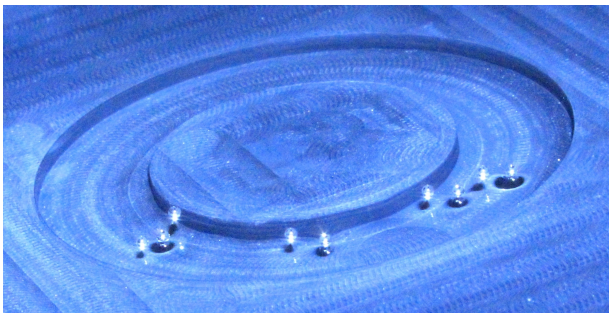

FIGURE 5.10: The collapse of what was a string of 11 walkers. Two of them merged before being vanished. The others form clusters of droplets that remain in a bouncing state, despite a forcing acceleration of $\Gamma \simeq 3.66$ which turns a single droplet into a walker, in a deep shallow region. The distance between two droplets is below a wavelength. We suspect the string of droplets collapsed because the wavefield self-interfered, which led to a destabilisation of the system.

5.2.3 Model

Actual models [35, 107] do not account for 1d geometries where emitted waves strongly depend on the presence of boundaries or on the viscous damping of emitted Faraday waves. As a consequence, we choose to adapt an existing model [107] to our experiments. We first assume that the standing waves associated with the successive droplet impacts are given by damped sine waves along the s-coordinate. We reduce the system to a 1d liquid profile $\zeta(s,t)$ along the ring. The driving horizontal force is supposed to be proportional to the slope of the liquid profile at each impact. Since the successive bounces are periodic events, separated by a time $\tau_F = 2/f$, a phenomenological strobed

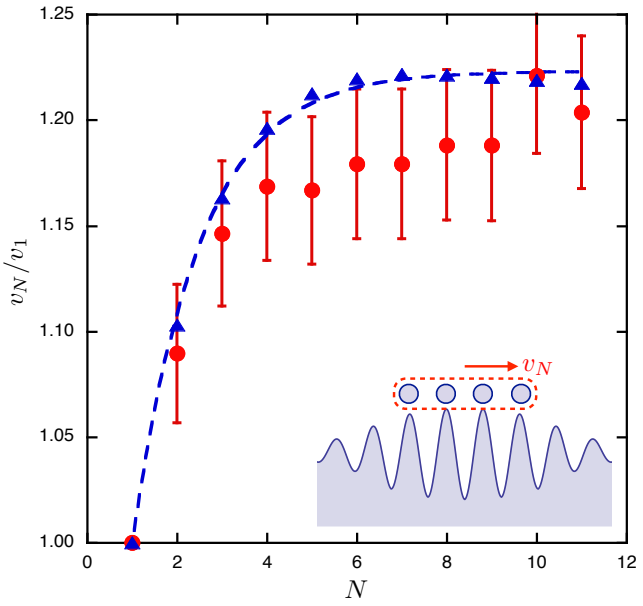

FIGURE 5.11: (Circles) Speed v_N of a droplet string as a function of its number N of components. The speed is normalised by the speed v_1 of single droplets. Error bars are indicated. The speed seems to saturate for large systems. (Triangles) The model described in the main text captures this effect for both synchronous (triangle up) and antisynchronous (triangle down) cases. A good agreement is found between the model and the experimental data. The dashed curve is a guide for the eye.

equation of motion is considered for each droplet i. The speed change $u^i_{n+1} - u^i_n$ of droplet i between the n^{th} and $(n+1)^{\text{th}}$ impacts is given by

$$u^i_{n+1} - u^i_n = -\gamma u^i_n - C_0 \left.\frac{\partial \zeta^{ii}}{\partial s}\right|_{n+1} - C_1 \sum_{j\neq i} \left.\frac{\partial \zeta^{ij}}{\partial s}\right|_{n+1}. \tag{5.2}$$

The first term represents some dissipation at bouncing, due to air drag and the shear of the air layer, with a parameter γ. The second term, with a coefficient C_0, represents the interaction of the droplet i at the $(n+1)^{\text{th}}$ impact with the waves produced by the same droplet at previous impacts. The last term, with a coefficient C_1, represents the interactions between the droplets in a string. We expect C_1 to be different from C_0 because the system is quasi 1d rather than purely 1d. As a consequence, waves emitted by neighbour droplets are also radiated outside the channel and this effect is taken into account thanks to C_1 (see Figures 5.9 and 4.1 for a general overview). Since we only focus on droplet motion in the tangential direction, the relevant information for the strobed equation (5.2) is given by

$$\zeta^{ij} = \zeta_0 \cos\left(\frac{2\pi(s^i_{n+1} - s^j_n)}{\lambda_F}\right) \exp\left(-\frac{s^i_{n+1} - s^j_n}{\delta}\right), \tag{5.3}$$

where ζ_0 is an arbitrary parameter containing the wave amplitude and thus the memory. Assuming $u_n^1 = u_n^2 = v_2$, only one solution is found with quantified distances, depending on whether successive walkers are in phase or out of phase. The model [44, 150] is calibrated as follows: the speed of a lonely droplet gives us the ratio C_0/γ, the value of δ is chosen as $2.1\,\lambda_F$ in order to fit the exponential decrease of v_2, this value is in the range of previous values of δ [107, 129]. Finally, C_1 is the only remaining fitting parameter with $C_0/\gamma \approx 0.03$ and $C_0 \approx 20\,C_1$. Quantification is shown in Figure 5.5. The agreement with the experimental data is excellent, except for ϵ_0 which remains close to zero in the model. Moreover, it can be shown that the speed of a group is larger than individual speeds. The group speed v_2 is seen to decay with the interdistance between two droplets. This is illustrated in Figure 5.7. Extra speed for a pair of droplets is due to the constructive interference of waves emitted from both droplets. Since the wave damping is already taken into account through δ, the fact that C_1 is much lower than C_0 has an origin related to the non-trivial dissipation of waves out of the cavity. Indeed, the self-interaction of a droplet with its wave is a local phenomenon, while cross interactions between droplets involve propagation and reflection of waves along the cavity. Although different interaction coefficients should be considered, the coherent wave dynamics is well captured by our model. By generalising the calculations to N droplets, it is possible to estimate numerically the speed increase of v_N reported in Figure 5.11. Numerical results are shown in this plot (see triangles). Qualitative agreement with the experimental data are obtained. Moreover, using different quantified distances for successive droplets, we are able to show that the asymptotic speed limit decreases with the distance between adjacent droplets. In fact, decoherence appears for distant droplets. A complete derivation of our model can be read in Appendix B.

5.2.4 Discussion

In summary, we have investigated bouncing droplets in a geometry confining them into a nearly 1d system. The wave emitted by a walker becomes a damped sine wave. We evidenced a remarkable feature for 1d walkers: they form a group bouncing collectively leading to a faster motion than independent elements. The fact that coherent waves can be created push the analogy between walking droplets and quantum system further by considering, for example, wave guide. Moreover, 1d systems as considered herein are promising since droplets can be conveyed to collisions and other phenomena which are reminiscent of quantum information or wavefields.

5.3 Conclusion

In this chapter, we focused on the interactions between droplets. First, we have seen that placing several droplets within a linear channel gives us a variety of droplets behaviours. Indeed, when interacting, they can simply repel in opposite directions, merge to form a larger droplet, or even orbit and follow a twin star motion. Interacting walkers can also follow each other at fixed distances. However, they are frequently disturbed by the edges of the cavity. Two walkers were sometimes stuck for a few seconds nearby the extremity of a channel. In addition, when several droplets were moving as a string, this string could be split in two parts when the « head » droplet was interacting with an edge. Combining these reasons with the non negligible probability for two droplets to merge makes it difficult and non convenient to study the interactions and the dynamics of a chain of droplets, since it can hardly last for more than a few minutes. Secondly, we decided to use an annular cavity to place several walkers and force them to orbit in the same direction. We showed that it was convenient and that one could easily add another droplet to grow the string of orbiting walkers. Besides, we demonstrated that within annular cavities, droplets share a common coherent wave that propels the group at a velocity faster than a single drop, which differs from the 2d case known in litterature [111, 129], thanks to the coherent wave that couples walkers together. It was shown that co-orbiting droplets move along circles of quantified radii [111]. In 2d, the rectilinear motion of two droplets, the so-called “promenade mode”, has been studied by Borghesi *et al.* [129]. It was demonstrated that walkers can move together at quantified average distances with a velocity proportional to their separation. In our case, when studying pairs of walkers, we demonstrated the quantisation of the interdistances s between walkers, but the opposite about the speed that grows when both walkers are getting closer. Finally, we studied a string of N droplets, and showed that the speed of the string increases with the number of droplets. In addition, we developed a model in good agreement with our observations. This model is entirely derived in Appendix B. We also demonstrated that the ring could not be filled entirely with walkers, since that, at a certain point, the wavefield self interacts when the string is getting longer.

Chapter 6

Conclusion and perspectives

Conclusion

In this thesis, we focused on a tiny but fascinating entity: a droplet. This object of everyday life is still full of mysteries and knows numerous promising development in various fields such as biochemical, medicine, industry and more.

In Chapter 1, we developed the importance of understanding the physics of droplets and how to manipulate them in order to perform various operations encountered in microfluidics. We have finally retained an original method to handle droplets without touching them: bouncing droplets. This method was popularised by the group of Couder in 2005.

In Chapter 2, we introduced the experiments of bouncing and walking droplets and the various works that have already been done. We showed that a walking droplet is definitely a surprising object, which exhibits remarkable features that may remind the world of quantum mechanics, even though it has more differences than similarities to this field. In any case, the physicist who wants to enter and discover the world of walkers should better see this entity has a striking curiosity than an entire analog of the quantum world. This said, the walker exhibits a duality with its own waves, created at each impact with the bath. When the droplet has vanished, no waves are created and conversely, if the waves can hardly propagate, for example because of a shallow water region, the walker ceases to exist. Numerous investigations were based on a walker evolving in a 2d geometry. The first question we answered was « is it possible to confine a walker and force it to move along a quasi 1d geometry? ». That was the aim of Chapter 3.

In our third chapter, after a short presentation of our experimental setup, we proposed a method to constraint a droplet along a 1d path. Our starting point was to vary the fluid depth, in order to prevent the waves from propagating and consequently, to prevent the droplet from walking. This starting point led us to build rectilinear cavities, of width proportional to the Faraday wavelength. We evidenced the existence of an optimal width that ensured the 1d motion of a walker, thanks to a kinetic energy study. In addition, with a model based on the analogy with waveguide systems and the observations of the Faraday instability in our channels, one modelled the evolution of the longitudinal speed of walkers.

In Chapter 4, we studied annular cavities. We demonstrated that fixing the width of an annulus to the optimal width to confine a walker in a linear channel provides regular circular path for the walkers. Secondly, we emphasised the effects of the memory parameter. In specific conditions, we evidenced that the expected behaviour of the droplet speed could be faulted, in particular for a 1d ring with tiny walkers. Despite a lack of model to explain this trend, we made some assumptions to characterise the decrease of a tiny walkers' speed with the memory, based on the bouncing mode which may differ between large and small walkers. Afterwards, we opened the door to a new kind of experiments, which is an extension to prior tunnelling effects works. We looked at the effect of periodic submarine obstacles on walkers. We demonstrated that such a lattice decreases the mean speed of a walker, but also that there are allowed and forbidden bands, similarly to the Kronig-Penney model.

Finally, in Chapter 5, we studied the interactions between walkers, within linear and circular cavities. After listing the different kinds of events that occur between two interacting walkers, we focused on the interactions between walkers within an annular cavity. We demonstrated that we can easily build a chain of walkers, that share a coherent wave propelling the group of droplets at a speed faster than a singe droplet. A model was developed in reasonable agreement with our observations. We also evidenced that, at a certain point, the string of droplet self-interferes and destabilises itself. It is thus impossible to complete our annular cavity with walkers. The longest chain we managed to create was made of 11 walkers, see Figure 6.1(a). However, we found an interesting case, similar to our experiment involving « levitating droplets », where a « cavity » was entirely completed. It deals with the experiment of the hydraulic jump, which was widely studied in the thesis of Alexis Duchesne [151]. In Figure 6.1(b) a hydraulic jump was completed with 18 droplets. Note that there are also some differences with our experiment. One of the main being that, in Figure 6.1(b),

the droplets are only animated by an internal motion, they do not orbit within the hydraulic jump.

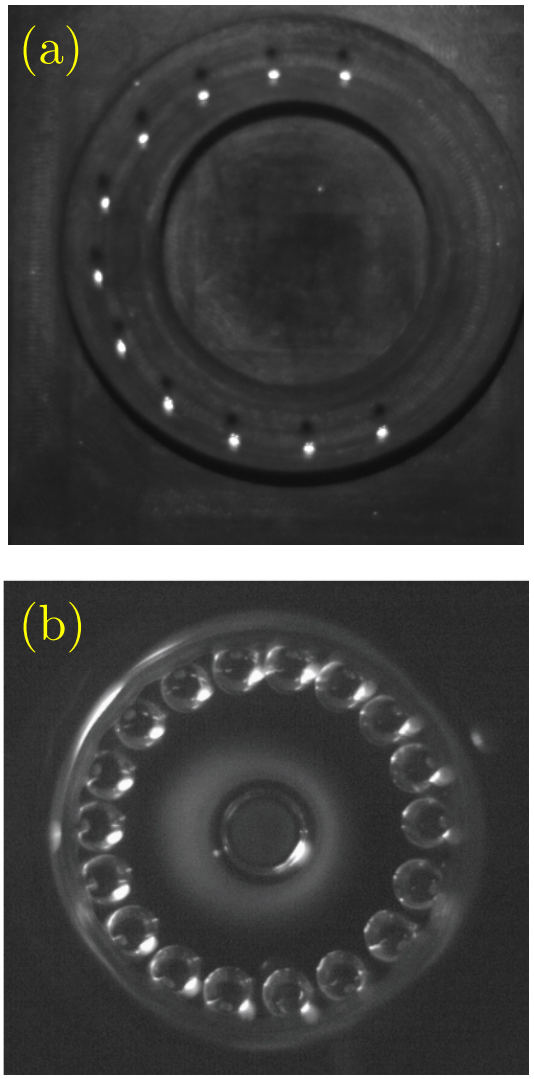

FIGURE 6.1: (a) Photograph of a chain of 11 walkers of diameter $2r_d = 0.8$ mm. We never succeed in adding more walkers into the ring, since the wavefield of the string self-interferes and leads to its own collapse. (b) Photograph of a hydraulic jump of radius $R_j \simeq 1$ cm, entirely completed with a chain of 18 droplets of diameter $2r_d \simeq 2$ mm (from [151]).

Perspectives

In the following, we list some perspectives and developments that may lead to a better understanding of the walkers and answer some of our questions which remained unsolved.

Annular cavities

In Chapter 4, we studied the influence of the memory parameter on the speed of walkers. We evidenced that the speed of tiny walkers surprisingly decreased with Me, but only in annular cavities. Nevertheless, this result is purely empirical. It would be an interesting start for a numerical and/or theoretical study for a better understanding of this phenomenon.

Secondly, we focused on submarine obstacles in a 1d annular cavity. The experimental setup used is reminiscent to the Kronig-Penney model for electrons, that yields to the electronic band structure. We revealed the existence of a band gap for walkers, similarly to Kronig-Penney model. This constitutes only a start for other investigations. In particular, can we find other bands, upon exploring the area where the adimensionalised pitch of the lattice p/λ_F is lower than $1/2$? It would be worth analysing how these bands are affected by the other parameters such as the memory parameter Me, the liquid height above the obstacles h_{obs} and the droplet size r_d.

The speed of a walking droplet depends on the forcing conditions. However, in the whole manuscript, we fixed the forcing frequency at $f = 70$ Hz. One wonders when modifying f could lead to a system analog to some whispering gallery mode, in a circular cavity. It would be worth measuring the speed of a walker as a function of f and to characterise whether we can obtain resonances. Thus, modifying f would not imply a monotonic variation of the speed v of a walker, which would evolve through different maxima at the different resonance frequencies.

Other geometries

Another path to explore was proposed by a collaborator, Ward Struyve. The idea is to study whether a walker follows a trajectory according to bohmian or quantum mechanics. It finds out that the Bohm approach gives results that disagree with those obtained from standard mechanics. In particular, in references [152, 153], experiments are depicted where quantum particles cross an incomplete Stern-Gerlach interferometer. In the latter, the particles are first split and therefore recombined by successive regions of reversed fields, as it is illustrated in Figure 6.2. Two cases occur depending on the nature of the trajectory. In the Bohm approach, the trajectories never cross: a particle that went through the upper (resp. lower) half plane will stay there, see Figure 6.2(a). On the contrary adopting a quantum mechanics point of vue yields crossed trajectories, as it is illustrated in Figure 6.2(b). We adapted this to build an interferometer for droplets, as one can observe in Figure 6.3. What is the probability to obtain such

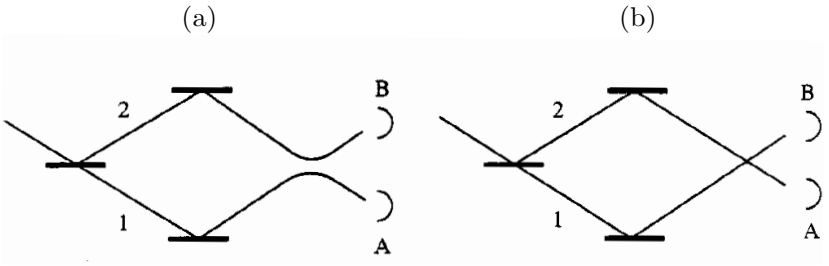

FIGURE 6.2: Schematic of an incomplete Stern Gerlach interferometer, where atoms are sent. One bit which way detectors are placed such that they enable us to distinguish whether the atoms borrowed the upper path 2, or the lower path 1. (a) In bohmian mechanics, one notes the non-crossing of trajectories. Thus, a particle that went through the upper (resp. lower) detector will hit the upper (resp. lower) part of the screen. (b) Path through an incomplete interferometer according to quantum mechanics (from [153]).

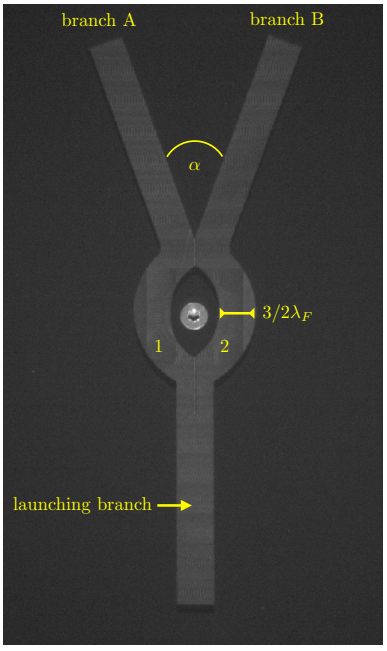

FIGURE 6.3: Photograph of our interferometer for walkers. The width of the branches are chosen so that the motion of the droplet is a 1d motion, accordingly to our results in Chapter 3. The interferometer is composed of a launching branch, at the end of it, there is a splitting between two paths: 1 and 2. These paths are crossed and two branches A and B can collect the walker. We note α the angle between both branches A and B.

trajectories for a walker ? Some preliminar and encouraging results were obtained, as shown in Figure 6.4. It is worth studying the influence of the parameters such as Me or the angle α and designing other interferometers, in order to determine whether a cavity is in favour of bohmian or quantum path. This is the beginning for a new kind of experiments on walkers.

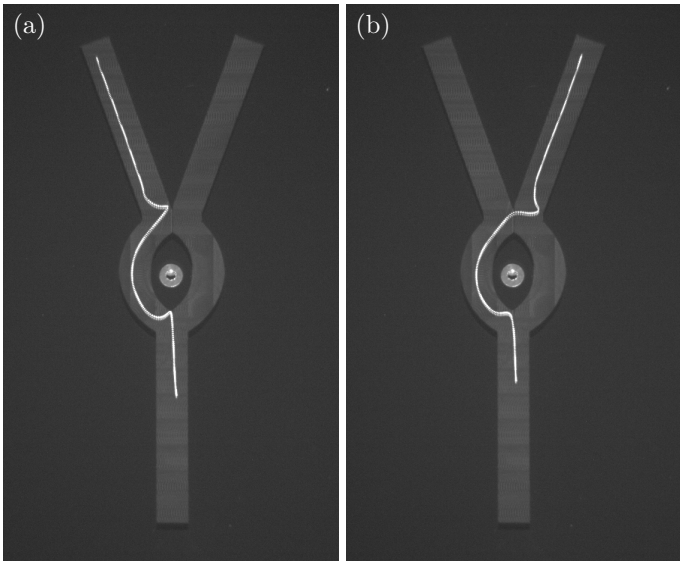

FIGURE 6.4: Chronophotography of experiments performed in a droplet interferometer. (a) A trajectory analog to bohmian mechanics, with a non-crossing of the trajectory. (b) Path followed by a walker, similarly to quantum mechanics.

Faraday instability in cavities

Finally, another field remains less explored. It is the occurence of the Faraday instability in our cavities, as it is illustrated in Figure 6.5. Figure 6.5(a) presents the Faraday patterns observed at different frequencies in a 1d annular cavity of radius R_{small}. Figure 6.5(b) shows the Faraday patterns for a larger annular cavity of width $4\lambda_F$. One observes the presence of the evanescent waves outside both cavities. In Figure 6.5(a), one notes that the number of wavelengths that appear in the cavity increases with the frequency, as expected when deriving the dispersion relation. However, in Figure 6.5(b), the patterns obtained are more complex, since the width of the cavity is larger than the wavelength when f is large enough. It results in patterns that are no longer stationary, and it becomes harder to determine precisely the number of wavelengths filling the cavity. In addition, in both cases, we observed that the number of wavelengths in the cavity can be degenerated. It would be interesting to study the influence of the forcing frequency on the number of wavelengths, and to characterise the degenerescence. Since the Faraday instability is behind the process of walking, gathering these information would maybe give us the solution to understand some problems in the community of walkers, that remain unsolved ? Maybe some new counter-intuitive events could be discovered as well. In addition, developments on Faraday instability on a patterned surface are of interest [154]. One could imagine that it would enable us to design cavities with new submarine obstacles and, without performing a single experiment, by

only knowing about the Faraday instability in this exotic case, one could foresee all the effects it could have on a walker.

The world of bouncing and walking droplets abounds with numerous curiosities, some of them are understood but many remains to be discovered. Finally, in this last decade, a simple droplet has revealed an unexpected treasure.

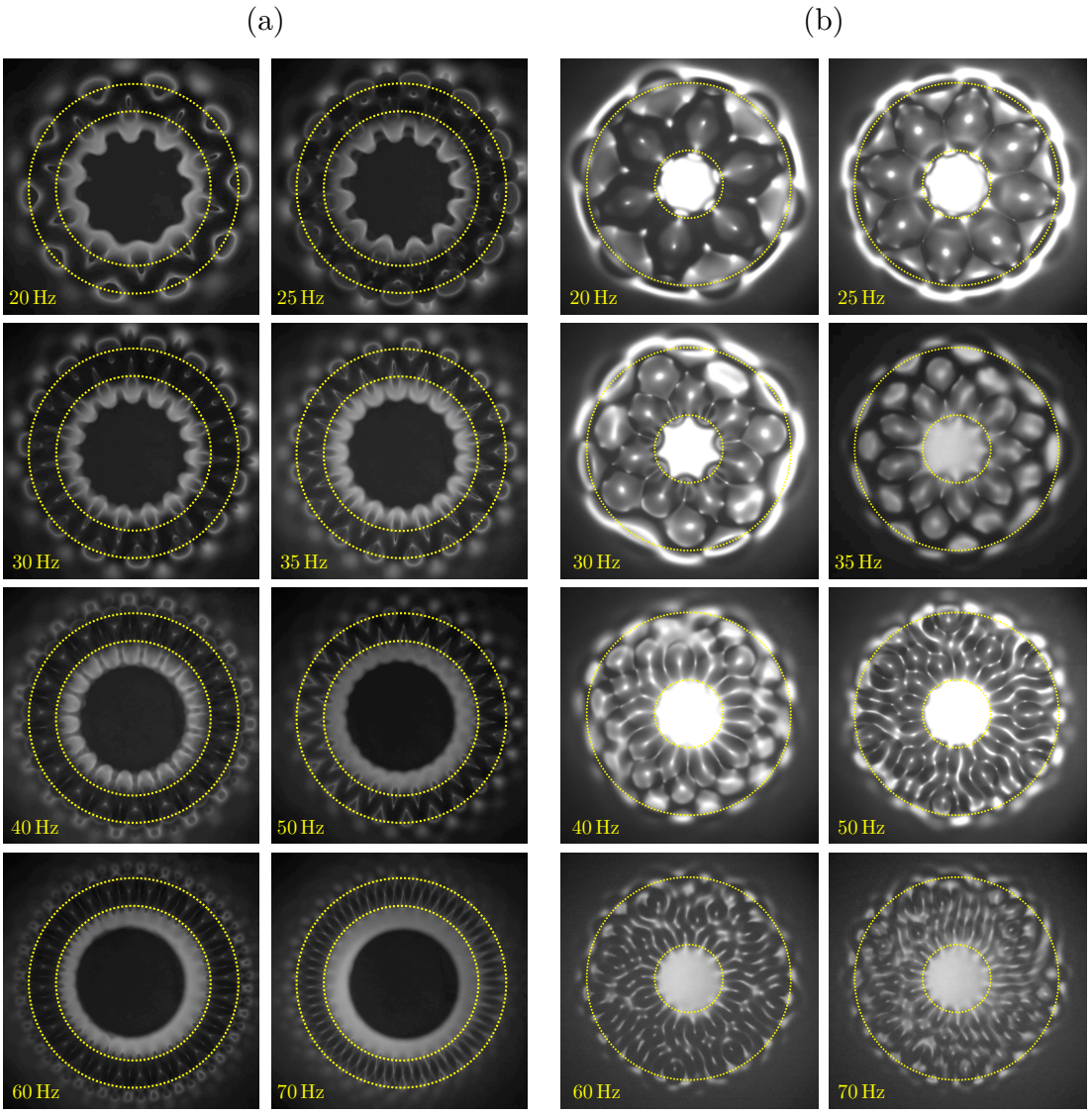

FIGURE 6.5: Faraday patterns in annular cavities, at different frequencies. The yellow dashed lines evidence the borders of the cavity. (a) Annular cavity of radius R_{small} and of width 1.5 λ_F. (b) Annular cavity of width $4\lambda_F$.

Appendix A

Droplets size measurement

The method we used to measure the size of a droplet created with the droplet dispenser is the following. The fall of hundreds of droplet, created in the same experimental conditions, have been recorded thanks to a high speed camera. A Matlab code has been implemented to track the position of the drop and to measure its size, as it is illustrated in Figure A.1. In addition, to drastically enhance the precision of our measurement, we have added a numerical and random gaussian noise on each image. Therefore, our code provides an averaged value of the size of our droplet with a precision of 1%.

Thus, we generated droplets of diameter $2r_d = 0.800$ mm, $2r_d = 0,713$ mm. The largest droplets used in this manuscript of diameter $2r_d \simeq 0.9$ mm, are resulting from the merging of two «tiny » droplets of $2r_d \simeq 0,7$ mm.

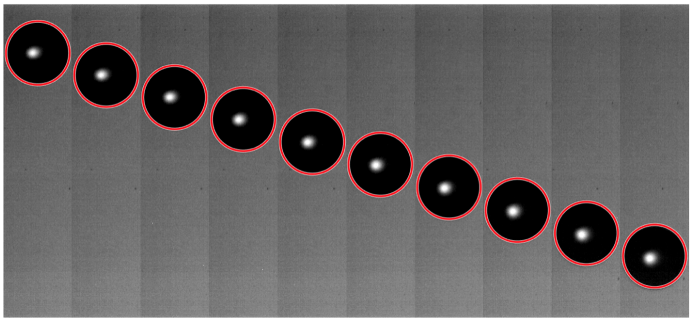

FIGURE A.1: Successive photographs of the fall of a single droplet, generated by our droplet dispenser. A Matlab code enables us to detect the position of the drop, as it is illustrated with the red circles, but also to determine the radius of the drop.

Appendix B

Modelling a string of walkers

The motion of a walker on the liquid surface originates from the coupling between the droplet and the waves emitted at each impact. An empirical model has been proposed by Fort and coworkers [44] to describe the walking behaviour taking advantage of the stroboscopic nature of the dynamics. One has

$$u_{n+1} - u_n = -\gamma u_n - C_0 \left.\frac{\partial \zeta}{\partial s}\right|_{n+1}. \tag{B.1}$$

In this expression, u is the walker speed along the s-direction, the subscript n refers to the n^{th} impact and the coefficient C_0 represents the coupling between the walker and its own wavefield $\zeta(s,t)$. Besides the wave-coupling term, a friction term has been added to take account of the dissipation of energy during impacts, with γ being the viscous-like coefficient. One can generalise this model to N droplets bouncing on the bath by considering the linear superposition of all produced wavefield.

$$u^i_{n+1} - u^i_n = -\gamma u^i_n - C_0 \left.\frac{\partial \zeta^{ii}}{\partial s}\right|_{n+1} - C_1 \sum_{j\neq i} \left.\frac{\partial \zeta^{ij}}{\partial s}\right|_{n+1}. \tag{B.2}$$

The superscript of the speed refers to the i^{th} walker on the surface and the superscripts of the wavefield denote the interaction of walker i with the wavefield arising from walker j. For this term, a coupling coefficient C_1 is considered and may be different from C_0. This difference comes from the dissipation of energy outside the channel. The waves emitted by a walker in the channel reads

$$\zeta^{ij}(s^i,t) = \zeta_0 \cos\left(k_F(s^i(t) - s^j_{imp})\right) \exp\left(-\frac{s^i(t) - s^j_{imp}}{\delta}\right) \exp\left(-\frac{t - t^j_{imp}}{\tau}\right), \tag{B.3}$$

where k_F is the Faraday wave number and s^j_{imp} and t^j_{imp} are the impact position and time respectively. The viscosity of the bath has been taken into account with the exponential factor $\exp(-(s^i(t)-s^j_{imp})/\delta)$ where δ is some viscous length. The memory of the walker has been considered with the factor $\exp(-(t-t^j_{imp})/\tau)$ where τ is the memory time. In the case of several impacts, the wavefields have to be summed up over the whole trajectory leading to

$$\zeta^{ij}(s^i,t) = \zeta_0 \sum_{p=-\infty}^{n} \cos\left(k_F(s^i(t)-s^j_p)\right) \exp\left(-\frac{s^i(t)-s^j_p}{\delta}\right) \exp\left(-\frac{t-t^j_p}{\tau}\right). \quad \text{(B.4)}$$

It was shown that, in the case of a 1d dynamics and in the low memory regime, the total wave field can be simplified by considering only the last impact with an equivalent amplitude ζ_{eq} [129, 150]. One has

$$\zeta^{ij}(s^i,t) = \zeta_{eq} \cos\left(k_F(s^i(t)-s^j_{last})\right) \exp\left(-\frac{s^i(t)-s^j_{last}}{\delta}\right) \quad \text{(B.5)}$$

where s^j_{last} and t^j_{last} are the last impact position and time respectively. Knowing the total wavefield and assuming a stationary regime where $s^i_{n+1}(t) - s^i_n = u^i_n \tau_F$, one gets, in the particular case of two walkers:

$$\begin{aligned} u^1_n = {} & \frac{C_0}{\gamma}\left(\sin\left(k_F\tau_F u^1_n\right) + \frac{1}{k_F\delta}\cos(k_F\tau_F u^1_n)\right)\exp\left(-\frac{\tau_F u^1_n}{\delta}\right) \\ & \pm \frac{C_1}{\gamma}\left(\sin\left(k_F(\tau_F u^2_n + d)\right) + \frac{1}{k_F\delta}\cos(k_F(\tau_F u^2_n + d))\right)\exp\left(-\frac{\tau_F u^2_n + d}{\delta}\right), \quad \text{(B.6)} \\ u^2_n = {} & \pm\frac{C_1}{\gamma}\left(\sin\left(k_F(\tau_F u^1_n - d)\right) - \frac{1}{k_F\delta}\cos(k_F(\tau_F u^1_n - d))\right)\exp\left(-\frac{d-\tau_F u^1_n}{\delta}\right) \\ & + \frac{C_0}{\gamma}\left(\sin\left(k_F\tau_F u^2_n\right) + \frac{1}{k_F\delta}\cos(k_F\tau_F u^2_n)\right)\exp\left(-\frac{\tau_F u^2_n}{\delta}\right), \quad \text{(B.7)} \end{aligned}$$

where $\pm$ accounts for synchronised or anti-synchronised droplets and $d = s^1 - s^2$ is the interdistance between the walkers. Assuming the same speed for both droplets ($u^1_n = u^2_n = v_2$) leads to the following conditions

$$\begin{aligned} & \sin\left(k_F(\tau_F v_2 + d)\right) + \frac{1}{k_F\delta}\cos(k_F(\tau_F v_2 + d)) = \\ & \left(\sin\left(k_F(\tau_F v_2 - d)\right) - \frac{1}{k_F\delta}\cos(k_F(d - \tau_F v_2))\right)\exp\left(\frac{2\tau_F v_2}{\delta}\right), \quad \text{(B.8)} \\ v_2 = {} & \frac{C_0}{\gamma}\left(\sin\left(k_F\tau_F v_2\right) + \frac{1}{k_F\delta}\cos(k_F\tau_F v_2)\right)\exp\left(-\frac{\tau_F v_2}{\delta}\right) \\ & \pm \frac{C_1}{\gamma}\left(\sin\left(k_F(\tau_F v_2 + d)\right) + \frac{1}{k_F\delta}\cos(k_F(\tau_F v_2 + d))\right)\exp\left(-\frac{\tau_F v_2 + d}{\delta}\right). \quad \text{(B.9)} \end{aligned}$$

The first equation gives the distance quantification and the second one gives the speed of a pair of drops v_2. Because of the non-linearity of both equations, one needs to solve then by iteration. Taking initially $v_2 = v_1$, the speed of a single walker and $d = n\lambda_F/2$, the multiples of the half Faraday wavelength, leads to the coefficient $C_0/\gamma = 0.0282$, $C_1 = 0.05C_0$ and $\delta = 2.1\lambda_F$. Eqs.(B.8) and (B.9) converge to a solution after a tenth of iterations. The value of δ is close to the one encountered in models of walkers. The value of C_1 compared to C_0 shows that only 5% of the wave emitted by walker j acts on walker i. One can understand the decrease of v_2 as a function of δ because of the factor $\exp(-(\tau_F v_2 + d)/\delta)$ in equation(B.9). This behaviour is due to the viscous properties of the bath that leads to an exponential damping of the waves. One can also rationalise a value of v_2 higher than v_1 by checking the values of d and the synchronicity of the bounce. Those values are the ones that lead to constructive interference of the surface waves. Because the speed of a walker is directly proportional to the slope of the waves, a higher amplitude leads to a faster motion.

In the case of N droplets, one assumes that the quantified interdistances between the droplets are unchanged. Doing so, the speed v_N of a chain of droplets is

$$v_N = \frac{C_0}{\gamma}\left(\sin\left(k_F\tau_F v_N\right) + \frac{1}{k_F\delta}\cos(k_F\tau_F v_N)\right)\exp\left(-\frac{\tau_F v_N}{\delta}\right)$$
$$\pm\frac{C_1}{\gamma}\sum_{i=1}^{n}\left(\sin\left(k_F(\tau_F v_N + id)\right) + \frac{1}{k_F\delta}\cos(k_F(\tau_F v_N + id))\right)\exp\left(-\frac{\tau_F v_N + id}{\delta}\right). \tag{B.10}$$

The results of this equation reproduce the increase of the speed thanks to constructive interference.

We show that a model based on the superposition of all waves reproduces the observed experimental behaviour. Thanks to constructive interferences, the coherent wave propels the string of droplets faster than single ones. Furthermore, as the distance between the walkers increases, the speed is reduced because of the viscous damping.

Bibliography

[1] C. Longquan, E. Bonaccurso, P. Deng, and H. Zhang. Droplet impact on soft viscoelastic surfaces. *Physical Review E*, 94:063117, 2016.

[2] D. Khojasteh, M. Kazerooni, S. Salarian, and R. Kamali. Droplet impact on superhydrophobic surfaces: a review of recent developments. *Journal of Industrial and Engineering Chemistry*, 42:1, 2016.

[3] C. Josserand and S. T. Thoroddsen. Drop impact on a solid surface. *Annual Review of Fluid Mechanics*, 48:365, 2016.

[4] A. van der Bos, M.-J. van der Meulen, T. Driessen, M. van den Berg, H. Reinten, H. Wijshoff, M. Versluis, and D. Lohse. Velocity profile inside piezoacoustic inkjet droplets in flight: comparison between experiment and numerical simulation. *Physical Review Applied*, 1:014004, 2014.

[5] Z. Xingye, Y. Shouqi, L. Junping, and L. Xingfa. Comparison of droplet distributions from fluidic and impact sprinklers. *Frontiers of Agricultural Science and Engineering*, 2:53, 2015.

[6] W. Jia and H. H. Qiu. Experimental investigation of droplet dynamics and heat transfer in spray cooling. *Experimental Thermal and Fluid Science*, 27:829, 2003.

[7] A. L. N. Moreira, A. S. Moita, and M. R. Panao. Advances and challenges in explaining fuel spray impingement: how much of single droplet impact research is useful? *Progress in Energy and Combustion Science*, 36:554, 2010.

[8] H. K. Webb, J. Hasan, V. K. Truong, R. K. Crawford, and E. P. Ivanova. Nature inspired structured surfaces for biomedical applications. *Current Medicinal Chemistry*, 18:3367, 2011.

[9] H. Zhu, Z. Guo, and W. Liu. Biomimetic water-collecting materials inspired by nature. *Chemical Communications*, 52:3863, 2016.

[10] P. Aussillous and D. Quéré. Properties of liquid marbles. *Proceedings of the Royal Society of London A: Mathematical, Physical and Engineering Sciences*, 462:973, 2006.

[11] M. Lee, Y. S. Chang, and H.-Y. Kim. Drop impact on microwetting patterned surfaces. *Physics of Fluids*, 22:072101, 2010.

[12] Y. Lu, S. Sathasivam, J. Song, C. R. Crick, C. J. Carmalt, and I. P. Parkin. Robust self-cleaning surfaces that function when exposed to either air or oil. *Science*, 347:1132, 2015.

[13] F. Mugele and J.-C. Baret. Electrowetting: from basics to applications. *Journal of Physics: Condensed Matter*, 17:R705, 2005.

[14] R. De Ruiter, J. de Ruiter, H. B. Eral, C. Semprebon, M. Brinkmann, and F. Mugele. Buoyant droplets on functional fibers. *Langmuir*, 28:13300, 2012.

[15] H. B. Eral, J. de Ruiter, R. de Ruiter, J. M. Oh, C. Semprebon, M. Brinkmann, and F. Mugele. Drops on functional fibers: from barrels to clamshells and back. *Soft Matter*, 7:5138, 2011.

[16] M. J. Jebrail and A. R. Wheeler. Let's get digital: digitizing chemical biology with microfluidics. *Current Opinion in Chemical Biology*, 14:574, 2010.

[17] M. Abdelgawad and A. R. Wheeler. The digital revolution: a new paradigm for microfluidics. *Advanced Materials*, 21:920, 2009.

[18] B. Berge and J. Peseux. Variable focal lens controlled by an external voltage: an application of electrowetting. *The European Physical Journal E*, 3:159, 2000.

[19] C.-X. Liu, J. Park, and J.-W. Choi. A planar lens based on the electrowetting of two immiscible liquids. *Journal of Micromechanics and Microengineering*, 18: 035023, 2008.

[20] K. Mishra, C. Murade, B. Carreel, I. Roghair, J. M. Oh, G. Manukyan, D. van den Ende, and F. Mugele. Optofluidic lens with tunable focal length and asphericity. *Scientific Reports*, 4:6378, 2014.

[21] P. Mary, V. Studer, and P. Tabeling. Microfluidic droplet-based liquid-liquid extraction. *Analytical Chemistry*, 80:2680, 2008.

[22] D. L. Huber, R. P. Manginell, M. A. Samara, B.-I. Kim, and B. C. Bunker. Programmed adsorption and release of proteins in a microfluidic device. *Science*, 301:352, 2003.

[23] H. A. Stone, A. D. Stroock, and A. Ajdari. Engineering flows in small devices: microfluidics toward a lab-on-a-chip. *Annual Review of Fluid Mechanics*, 36:381, 2004.

[24] D. S. Millington, R. Sista, A. Eckhardt, J. Rouse, D. Bali, R. Goldberg, M. Cotten, R. Buckley, and V. Pamula. Digital microfluidics: a future technology in the newborn screening laboratory? *Seminars in Perinatology*, 34: 163, 2010.

[25] A. R. Wheeler. Putting electrowetting to work. *Science*, 322:539, 2008.

[26] H. Yang, V. N. Luk, M. Abelgawad, I. Barbulovic-Nad, and A. R. Wheeler. A world-to-chip interface for digital microfluidics. *Analytical Chemistry*, 81:1061, 2008.

[27] A. B. Theberge, E. Mayot, A. El Harrak, F. Kleinschmidt, W. T. S. Huck, and A. D. Griffiths. Microfluidic platform for combinatorial synthesis in picolitre droplets. *Lab on a Chip*, 12:1320, 2012.

[28] J. G. Leidenfrost. *De aquae communis nonnullis qualitatibus tractatus*. Ovenius, 1756.

[29] J. Leiterer, M. Grabolle, K. Rurack, U. Resch-Genger, J. Ziegler, T. Nann, and U. Panne. Acoustically levitated droplets. *Annals of the New York Academy of Sciences*, 1130:78, 2008.

[30] A. L. Yarin, M. Pfaffenlehner, and C. Tropea. On the acoustic levitation of droplets. *Journal of Fluid Mechanics*, 356:65, 1998.

[31] E. Welter and B. Neidhart. Acoustically levitated droplets—a new tool for micro and trace analysis. *Fresenius' Journal of Analytical Chemistry*, 357:345, 1997.

[32] A. A. Fedorets, M. Frenkel, E. Shulzinger, L. A. Dombrovsky, E. Bormashenko, and M. Nosonovsky. Self-assembled levitating clusters of water droplets: pattern-formation and stability. *Scientific Reports*, 7:1888, 2017.

[33] J. Walker. Drops of liquid can be made to float on liquid-what enables them to do so. *Scientific American*, 238:151, 1978.

[34] Y. Couder, E. Fort, C.-H. Gautier, and A. Boudaoud. From bouncing to floating: noncoalescence of drops on a fluid bath. *Physical Review Letters*, 94: 177801, 2005.

[35] J. W. M. Bush. Pilot-wave hydrodynamics. *Annual Review of Fluid Mechanics*, 47:269, 2015.

[36] S. Perrard, M. Labousse, E. Fort, and Y. Couder. Chaos driven by interfering memory. *Physical Review Letters*, 113:104101, 2014.

[37] D. M. Harris and J. W. M. Bush. Droplets walking in a rotating frame: from quantized orbits to multimodal statistics. *Journal of Fluid Mechanics*, 739:444, 2014.

[38] M. Labousse, S. Perrard, Y. Couder, and E. Fort. Build-up of macroscopic eigenstates in a memory-based constrained system. *New Journal of Physics*, 16: 113027, 2014.

[39] A. U. Oza, E. Siéfert, D. M. Harris, J. Moláček, and J. W. M. Bush. Orbiting pairs of walking droplets: dynamics and stability. *Physical Review Fluids*, 2: 053601, 2017.

[40] A. U. Oza, D. M. Harris, R. R. Rosales, and J. W. M. Bush. Pilot-wave dynamics in a rotating frame: on the emergence of orbital quantization. *Journal of Fluid Mechanics*, 744:404, 2014.

[41] M. Labousse, A. U. Oza, S. Perrard, and J. W. M. Bush. Pilot-wave dynamics in a harmonic potential: quantization and stability of circular orbits. *Physical Review E*, 93:033122, 2016.

[42] S. Perrard, M. Labousse, M. Miskin, E. Fort, and Y. Couder. Self-organization into quantized eigenstates of a classical wave-driven particle. *Nature Communications*, 5, 2014.

[43] A. Eddi, J. Moukhtar, S. Perrard, E. Fort, and Y. Couder. Level splitting at macroscopic scale. *Physical Review Letters*, 108:264503, 2012.

[44] E. Fort, A. Eddi, A. Boudaoud, J. Moukhtar, and Y. Couder. Path-memory induced quantization of classical orbits. *Proceedings of the National Academy of Sciences*, 107:17515, 2010.

[45] H.-Y. Chu, H.-T. Fei, and C.-R. Ko. One-dimensional wave-propelled bouncing drop on an oscillating liquid bath. *Physics of Fluids*, 25:042101, 2013.

[46] P.-G. de Gennes, F. Brochard-Wyart, and D. Quéré. *Gouttes, bulles, perles et ondes*. Belin Paris, 2002.

[47] L. Petit, J.-P. Hulin, and E. Guyon. *Hydrodynamique physique 3e édition*. EDP sciences, 2012.

[48] S. Yun and G. Lim. Ellipsoidal drop impact on a solid surface for rebound suppression. *Journal of Fluid Mechanics*, 752:266, 2014.

[49] J. Eggers and E. Villermaux. Physics of liquid jets. *Reports on Progress in Physics*, 71:036601, 2008.

[50] H. M. Gonnermann. Magma fragmentation. *Annual Review of Earth and Planetary Sciences*, 43:431, 2015.

[51] L. Rayleigh. On the capillary phenomena of jets. *Proceedings of the Royal Society of London*, 29(196):71–97, 1879.

[52] L. Rayleigh. Xxxvi. investigations in capillarity:—the size of drops.—the liberation of gas from supersaturated solutions.—colliding jets.—the tension of contaminated water-surfaces. *The London, Edinburgh, and Dublin Philosophical Magazine and Journal of Science*, 48:321, 1899.

[53] L. Rayleigh. On the instability of jets. *Proceedings of the London Mathematical Society*, 1:4, 1878.

[54] E. Villermaux. The formation of filamentary structures from molten silicates: Pelés hair, angel hair, and blown clinker. *Comptes Rendus Mécanique*, 340:555, 2012.

[55] F. B. Wadsworth, J. Vasseur, E. W. Llewellin, and D. B. Dingwell. Sintering of polydisperse viscous droplets. *Physical Review E*, 95:033114, 2017.

[56] D. Terwagne, N. Mack, S. Dorbolo, T. Gilet, J.-Y. Raty, and N. Vandewalle. The mayonnaise droplet. *Chaos: An Interdisciplinary Journal of Nonlinear Science*, 19:041105, 2009.

[57] N. Kapur and P. H. Gaskell. Morphology and dynamics of droplet coalescence on a surface. *Physical Review E*, 75:056315, 2007.

[58] P. J. Graham, M. M. Farhangi, and A. Dolatabadi. Dynamics of droplet coalescence in response to increasing hydrophobicity. *Physics of Fluids*, 24: 112105, 2012.

[59] Y. Amarouchene, G. Cristobal, and H. Kellay. Noncoalescing drops. *Physical Review Letters*, 87:206104, 2001.

[60] P. Dell'Aversana, J. R. Banavar, and J. Koplik. Suppression of coalescence by shear and temperature gradients. *Physics of Fluids*, 8:15, 1996.

[61] P. Dell'Aversana, V. Tontodonato, and L. Carotenuto. Suppression of coalescence and of wetting: the shape of the interstitial film. *Physics of Fluids*, 9:2475, 1997.

[62] K. R. Sreenivas, P. K. De, and J. H. Arakeri. Levitation of a drop over a film flow. *Journal of Fluid Mechanics*, 380:297, 1999.

[63] A. Duchesne, C. Savaro, L. Lebon, C. Pirat, and L. Limat. Multiple rotations of a drop rolling inside a horizontal circular hydraulic jump. *EPL (Europhysics Letters)*, 102:64001, 2013.

[64] A.-L. Biance, C. Clanet, and D. Quéré. Leidenfrost drops. *Physics of Fluids*, 15: 1632, 2003.

[65] H. Linke, B. J. Alemán, L. D. Melling, M. J. Taormina, M. J. Francis, C. C. Dow-Hygelund, V. Narayanan, R. P. Taylor, and A. Stout. Self-propelled leidenfrost droplets. *Physical Review Letters*, 96:154502, 2006.

[66] G. Lagubeau, M. Le Merrer, C. Clanet, and D. Quéré. Leidenfrost on a ratchet. *Nature Physics*, 7:395, 2011.

[67] L. Maquet, M. Brandenbourger, B. Sobac, A.-L. Biance, P. Colinet, and S. Dorbolo. Leidenfrost drops: effect of gravity. *EPL (Europhysics Letters)*, 110: 24001, 2015.

[68] P. Pierański. Jumping particle model. period doubling cascade in an experimental system. *Journal de Physique*, 44:573, 1983.

[69] N. B. Tufillaro and A. M. Albano. Chaotic dynamics of a bouncing ball. *American Journal of Physics*, 54:939, 1986.

[70] N. B. Tufillaro, T. M. Mello, Y. M. Choi, and A. M. Albano. Period doubling boundaries of a bouncing ball. *Journal de Physique*, 47:1477, 1986.

[71] S. T. Thoroddsen and K. Takehara. The coalescence cascade of a drop. *Physics of Fluids*, 12:1265, 2000.

[72] T. Gilet, N. Vandewalle, and S. Dorbolo. Controlling the partial coalescence of a droplet on a vertically vibrated bath. *Physical Review E*, 76:035302, 2007.

[73] S. Protière, Y. Couder, E. Fort, and A. Boudaoud. The self-organization of capillary wave sources. *Journal of Physics: Condensed Matter*, 17:S3529, 2005.

[74] N. Vandewalle, D. Terwagne, K. Mulleners, T. Gilet, and S. Dorbolo. Dancing droplets onto liquid surfaces. *Physics of Fluids*, 18:091106, 2006.

[75] T. Gilet, D. Terwagne, N. Vandewalle, and S. Dorbolo. Dynamics of a bouncing droplet onto a vertically vibrated interface. *Physical Review Letters*, 100:167802, 2008.

[76] S. Dorbolo, D. Terwagne, N. Vandewalle, and T. Gilet. Resonant and rolling droplet. *New Journal of Physics*, 10:113021, 2008.

[77] D. Terwagne, F. Ludewig, N. Vandewalle, and S. Dorbolo. The role of the droplet deformations in the bouncing droplet dynamics. *Physics of Fluids*, 25: 122101, 2013.

[78] T. Gilet, N. Vandewalle, and S. Dorbolo. Completely inelastic ball. *Physical Review E*, 79:055201, 2009.

[79] M. Hubert, F. Ludewig, S. Dorbolo, and N. Vandewalle. Bouncing dynamics of a spring. *Physica D: Nonlinear Phenomena*, 272:1, 2014.

[80] M. Hubert, D. Robert, H. Caps, S. Dorbolo, and N. Vandewalle. Resonant and antiresonant bouncing droplets. *Physical Review E*, 91:023017, 2015.

[81] J. Moláček and J. W. M. Bush. Drops bouncing on a vibrating bath. *Journal of Fluid Mechanics*, 727:582, 2013.

[82] F. Blanchette. Modeling the vertical motion of drops bouncing on a bounded fluid reservoir. *Physics of Fluids*, 28:032104, 2016.

[83] A. Eddi, A. Decelle, E. Fort, and Y. Couder. Archimedean lattices in the bound states of wave interacting particles. *EPL (Europhysics Letters)*, 87:56002, 2009.

[84] A. Eddi, A. Boudaoud, and Y. Couder. Oscillating instability in bouncing droplet crystals. *EPL (Europhysics Letters)*, 94:20004, 2011.

[85] A. Eddi, D. Terwagne, E. Fort, and Y. Couder. Wave propelled ratchets and drifting rafts. *EPL (Europhysics Letters)*, 82:44001, 2008.

[86] S. I. Lieber, M. C. Hendershott, A. Pattanaporkratana, and J. E. Maclennan. Self-organization of bouncing oil drops: two-dimensional lattices and spinning clusters. *Physical Review E*, 75:056308, 2007.

[87] Y. Couder and E. Fort. Single-particle diffraction and interference at a macroscopic scale. *Physical Review Letters*, 97:154101, 2006.

[88] Y. Couder, A. Boudaoud, S. Protière, and E. Fort. Walking droplets, a form of wave-particle duality at macroscopic scale? *Europhysics News*, 41:14, 2010.

[89] S. Protière, A. Boudaoud, and Y. Couder. Particle–wave association on a fluid interface. *Journal of Fluid Mechanics*, 554:85, 2006.

[90] M. Faraday. On a peculiar class of acoustical figures; and on certain forms assumed by groups of particles upon vibrating elastic surfaces. *Philosophical transactions of the Royal Society of London*, 121:299, 1831.

[91] S. Douady. Experimental study of the faraday instability. *Journal of Fluid Mechanics*, 221:383, 1990.

[92] W. S. Edwards and S. Fauve. Parametrically excited quasicrystalline surface waves. *Physical Review E*, 47:R788, 1993.

[93] W. S. Edwards and S. Fauve. Patterns and quasi-patterns in the faraday experiment. *Journal of Fluid Mechanics*, 278:123, 1994.

[94] O. Lioubashevski, J. Fineberg, and L. S. Tuckerman. Scaling of the transition to parametrically driven surface waves in highly dissipative systems. *Physical Review E*, 55:R3832, 1997.

[95] C. Wagner, H. W. Müller, and K. Knorr. Faraday waves on a viscoelastic liquid. *Physical Review Letters*, 83:308, 1999.

[96] A. Wernet, C. Wagner, D. Papathanassiou, H. W. Müller, and K. Knorr. Amplitude measurements of faraday waves. *Physical Review E*, 63:036305, 2001.

[97] W. Zhang and J. Vinals. Pattern formation in weakly damped parametric surface waves. *Journal of Fluid Mechanics*, 336:301, 1997.

[98] J. Miles and D. Henderson. Parametrically forced surface waves. *Annual Review of Fluid Mechanics*, 22:143, 1990.

[99] T. B. Benjamin and F. Ursell. The stability of the plane free surface of a liquid in vertical periodic motion. *Proceedings of the Royal Society of London. Series A, Mathematical and Physical Sciences*, 225:505, 1954.

[100] K. Kumar and L. S. Tuckerman. Parametric instability of the interface between two fluids. *Journal of Fluid Mechanics*, 279:49, 1994.

[101] K. Kumar. Linear theory of faraday instability in viscous liquids. *Proceedings of the Royal Society of London. Series A: Mathematical, Physical and Engineering Sciences*, 452:1113, 1996.

[102] B. A. Puthenveettil and E. J. Hopfinger. Evolution and breaking of parametrically forced capillary waves in a circular cylinder. *Journal of Fluid Mechanics*, 633:355, 2009.

[103] P. Chen and J. Viñals. Pattern selection in faraday waves. *Physical Review Letters*, 79:2670, 1997.

[104] D. Terwagne. *Bouncing droplets, the role of deformations*. PhD thesis, Université de Liège, 2011.

[105] S. Protiere. *Gouttes rebondissantes: une association onde-particule à échelle macroscopique*. PhD thesis, Université Paris-Diderot-Paris VII, 2007.

[106] A. U. Oza, R. R. Rosales, and J. W. M. Bush. A trajectory equation for walking droplets: hydrodynamic pilot-wave theory. *Journal of Fluid Mechanics*, 737:552, 2013.

[107] A. Eddi, E. Sultan, J. Moukhtar, E. Fort, M. Rossi, and Y. Couder. Information stored in faraday waves: the origin of a path memory. *Journal of Fluid Mechanics*, 674:433, 2011.

[108] J. Moláček and J. W. M. Bush. Drops walking on a vibrating bath: towards a hydrodynamic pilot-wave theory. *Journal of Fluid Mechanics*, 727:612, 2013.

[109] Y. Couder, S. Protière, E. Fort, and A. Boudaoud. Dynamical phenomena: walking and orbiting droplets. *Nature*, 437:208, 2005.

[110] S. Protière and Y. Couder. Orbital motion of bouncing drops. *Physics of Fluids*, 18:91114, 2006.

[111] S. Protiere, S. Bohn, and Y. Couder. Exotic orbits of two interacting wave sources. *Physical Review E*, 78:036204, 2008.

[112] G. I. Stegeman and M. Segev. Optical spatial solitons and their interactions: universality and diversity. *Science*, 286:1518, 1999.

[113] A. W. Liehr, A. S. Moskalenko, Y. A. Astrov, M. Bode, and H.-G. Purwins. Rotating bound states of dissipative solitons in systems of reaction-diffusion type. *The European Physical Journal B-Condensed Matter and Complex Systems*, 37:199, 2003.

[114] D. Shirokoff. Bouncing droplets on a billiard table. *Chaos: An Interdisciplinary Journal of Nonlinear Science*, 23:013115, 2013.

[115] R. P. Feynman, R. B. Leighton, M. Sands, and R. B. Lindsay. The feynman lectures on physics, vol. 3: quantum mechanics, 1966.

[116] D. Bohm. A suggested interpretation of the quantum theory in terms of « hidden" variables. i. *Physical Review*, 85:166, 1952.

[117] A. Andersen, J. Madsen, C. Reichelt, S. Rosenlund Ahl, B. Lautrup, C. Ellegaard, M. T. Levinsen, and T. Bohr. Double-slit experiment with single wave-driven particles and its relation to quantum mechanics. *Physical Review E*, 92:013006, 2015.

[118] A. Eddi, E. Fort, F. Moisy, and Y. Couder. Unpredictable tunneling of a classical wave-particle association. *Physical Review Letters*, 102:240401, 2009.

[119] G. Pucci, P. J. Sáenz, L. M. Faria, and J. W. M. Bush. Non-specular reflection of walking droplets. *Journal of Fluid Mechanics*, 804:R3, 2016.

[120] R. Dubertrand, M. Hubert, P. Schlagheck, N. Vandewalle, T. Bastin, and J. Martin. Scattering theory of walking droplets in the presence of obstacles. *New Journal of Physics*, 18:113037, 2016.

[121] T. Gilet. Dynamics and statistics of wave-particle interactions in a confined geometry. *Physical Review E*, 90:052917, 2014.

[122] D. M. Harris, J. Moukhtar, E. Fort, Y. Couder, and J. W. M. Bush. Wavelike statistics from pilot-wave dynamics in a circular corral. *Physical Review E*, 88: 011001, 2013.

[123] T. Gilet. Quantumlike statistics of deterministic wave-particle interactions in a circular cavity. *Physical Review E*, 93:042202, 2016.

[124] E. Fort and Y. Couder. Trajectory eigenmodes of an orbiting wave source. *EPL (Europhysics Letters)*, 102:16005, 2013.

[125] L. de Broglie. Une interprétation nouvelle de la mécanique ondulatoire est-elle possible? *Il Nuovo Cimento*, 1:37, 1955.

[126] L. de Broglie. *Ondes et mouvements*, volume 1. Gauthier-Villars et cie., 1926.

[127] L. M. Faria. A model for faraday pilot waves over variable topography. *Journal of Fluid Mechanics*, 811:51, 2017.

[128] P. A. Milewski, C. A. Galeano-Rios, A. Nachbin, and J. W. M. Bush. Faraday pilot-wave dynamics: modelling and computation. *Journal of Fluid Mechanics*, 778:361, 2015.

[129] C. Borghesi, J. Moukhtar, M. Labousse, A. Eddi, E. Fort, and Y. Couder. Interaction of two walkers: wave-mediated energy and force. *Physical Review E*, 90:063017, 2014.

[130] Y. Couder and E. Fort. Probabilities and trajectories in a classical wave-particle duality. *Journal of Physics: Conference Series*, 361:012001, 2012.

[131] J. W. M. Bush. Quantum mechanics writ large. *Proceedings of the National Academy of Sciences*, 107:17455, 2010.

[132] L. D. Tambasco, D. M. Harris, A. U. Oza, R. R. Rosales, and J. W. M. Bush. The onset of chaos in orbital pilot-wave dynamics. *Chaos: an Interdisciplinary Journal of Nonlinear Science*, 26:103107, 2016.

[133] A. Nachbin and V. S. Simões. Solitary waves in forked channel regions. *Journal of Fluid Mechanics*, 777:544, 2015.

[134] D. M. Harris and J. W. M. Bush. Generating uniaxial vibration with an electrodynamic shaker and external air bearing. *Journal of Sound and Vibration*, 334:255, 2015.

[135] D. M. Harris, T. Liu, and J. W. M. Bush. A low-cost, precise piezoelectric droplet-on-demand generator. *Experiments in Fluids*, 56:83, 2015.

[136] S. Perrard. *Une mémoire ondulatoire: états propres, chaos et probabilités.* PhD thesis, Université Paris Diderot, 2014.

[137] R. Carmigniani, S. Lapointe, S. Symon, and B. J. McKeon. Influence of a local change of depth on the behavior of walking oil drops. *Experimental Thermal and Fluid Science*, 54:237, 2014.

[138] G. Pucci, E. Fort, M. Ben Amar, and Y. Couder. Mutual adaptation of a faraday instability pattern with its flexible boundaries in floating fluid drops. *Physical Review Letters*, 106:024503, 2011.

[139] G. Pucci. Faraday instability in floating drops out of equilibrium: motion and self-propulsion from wave radiation stress. *International Journal of Non-Linear Mechanics*, 75:107, 2015.

[140] C. Dekker. Carbon nanotubes as molecular quantum wires. *Physics Today*, 52: 22, 1999.

[141] D. Ferry and S. M. Goodnick. *Transport in nanostructures.* Cambridge university press, 1997.

[142] W. Guerin, J.-F. Riou, J. P. Gaebler, V. Josse, P. Bouyer, and A. Aspect. Guided quasicontinuous atom laser. *Physical Review Letters*, 97:200402, 2006.

[143] A. Couvert, M. Jeppesen, T. Kawalec, G. Reinaudi, R. Mathevet, and D. Guéry-Odelin. A quasi-monomode guided atom laser from an all-optical bose-einstein condensate. *EPL (Europhysics Letters)*, 83:50001, 2008.

[144] V. Bacot, M. Labousse, A. Eddi, M. Fink, and E. Fort. Time reversal and holography with spacetime transformations. *Nature Physics*, 12:972, 2016.

[145] C. Kittel. *Introduction to solid state physics*. Wiley, 2005.

[146] A. Sánchez, E. Maciá, and F. Domínguez-Adame. Suppression of localization in kronig-penney models with correlated disorder. *Physical Review B*, 49:147, 1994.

[147] H.-S. Cho and P. R. Prucnal. New formalism of the kronig-penney model with application to superlattices. *Physical Review B*, 36:3237, 1987.

[148] D. A. McQuarrie. The kronig-penney model: A single lecture illustrating the band structure of solids. *The Chemical Educator*, 1:1, 1996.

[149] B. Filoux, M. Hubert, and N. Vandewalle. Strings of droplets propelled by coherent waves. *Physical Review E*, 92:041004, 2015.

[150] M. Labousse and S. Perrard. Non-hamiltonian features of a classical pilot-wave dynamics. *Physical Review E*, 90:022913, 2014.

[151] A. Duchesne. *Trois problèmes autour du ressaut hydraulique circulaire*. PhD thesis, Université Paris-Diderot-Paris VII, 2014.

[152] B.-G. Englert, M. O. Scully, G. Süssmann, and H. Walther. Surrealistic bohm trajectories. *Zeitschrift für Naturforschung A*, 47:1175, 1992.

[153] M. O. Scully. Do bohm trajectories always provide a trustworthy physical picture of particle motion? *Physica Scripta*, 76:41, 1998.

[154] J. Feng, I. Jacobi, and H. A. Stone. Experimental investigation of the faraday instability on a patterned surface. *Experiments in Fluids*, 57:86, 2016.